# 3D Laser Nanoprinted Metasurface for Light Manipulation

**Chenhao Li**


München 2024

# 3D Laser Nanoprinted Metasurface for Light Manipulation

**Chenhao Li**

Dissertation

an der Fakultät für Physik

der Ludwig-Maximilians-Universität

München

vorgelegt von

Chenhao Li

aus HEILONGJIANG. CHINA

München, den 12/06/2024

Erstgutacher/in: Prof. Dr. Leonardo de S. Menezes.

Zweitgutachter/in: Prof. Dr. Ralf Jungmann.

Tag der mündlichen Prüfung: 25/07/2024

# Contents

# List of Figures

# Zusammenfassung

In den letzten Jahren haben Fortschritte in der Lichtforschung unser Verständnis seiner Eigenschaften und Anwendungen erheblich vertieft. Licht, als der allgegenwärtigste Informationsträger, spielt eine entscheidende Rolle in Bereichen wie Bildgebung, Display, Kommunikation und Detektion. Die historische Entwicklung der traditionellen Optik hat zu erheblichen Errungenschaften und Innovationen geführt. Doch die zunehmende Komplexität und Raffinesse moderner optischer Systeme hat die Grenzen traditioneller optischer Komponenten aufgezeigt, was die Suche nach neuen Materialien und Strukturen angestoßen hat, die den steigenden Anforderungen an Leistung und Funktionalität gerecht werden können.

Metamaterialien, die künstliche Nanomaterialien sind, die so entwickelt wurden, dass sie Eigenschaften besitzen, die in natürlich vorkommenden Substanzen nicht zu finden sind, haben sich als vielversprechende Lösung für diese Herausforderungen herausgestellt. Im Gegensatz zu herkömmlichen Materialien können Metamaterialien elektromagnetische Wellen auf eine Weise manipulieren, die die Fähigkeiten der traditionellen Optik übertrifft. Diese einzigartige Fähigkeit rührt von ihren spezialisierten Strukturen her, die so gestaltet werden können, dass sie gewünschte Interaktionen mit Licht erzeugen. Unter diesen Metamaterialien haben Metaoberflächen aufgrund ihrer vielseitigen Funktionalität und relativen Einfachheit der Herstellung besondere Aufmerksamkeit erlangt

Metaoberflächen sind im Wesentlichen zweidimensionale periodische Nanoarrays, die eine beispiellose Kontrolle über Licht bieten. Durch die präzise Abstimmung der Größe, Form und Anordnung der Nanostrukturen können Metaoberflächen verschiedene Eigenschaften des Lichts modulieren, wie Polarisation, Phase und Intensität. Aktuelle Forschungs- und Entwicklungsarbeiten haben das Potenzial von auf Metaoberflächen basierenden Geräten in einer Vielzahl von Anwendungen gezeigt. Beispielsweise können Metaflächenlinsen (auch Metalinsen genannt) Licht mit hoher Effizienz und minimalen Aberrationen fokussieren und dabei oft traditionelle Linsen übertreffen. Ebenso ermöglichen Metaoberflächenpolarisatoren eine präzise Kontrolle des Polarisationszustands des Lichts, was für Bildgebungs- und Telekommunikationsanwendungen entscheidend ist. Die Einfachheit der Herstellung von Metaoberflächen in Kombination mit ihrer leistungsstarken Funktionalität macht sie zu einer attraktiven Option für die Entwicklung fortschrittlicher optischer Geräte. Allerdings schränken die komplexen Prozesse und teuren Geräte, die für die Herstellung von Metaflächen erforderlich sind, oft deren breitere Anwendung ein, und die inhärenten Beschränkungen zweidimensionaler Nanostrukturen begrenzen ihre Funktionalität.

In dieser Arbeit schlagen wir eine nanogedruckte 3D-Metaoberfläche basierend auf der Laser-Direktschreibtechnologie vor. Diese neue Art von Metaoberfläche bietet eine verbesserte Substratkompatibilität und ermöglicht das direkte Drucken auf verschiedenen Oberflächen, wie z. B. dem Endgesicht einer optischen Faser. Darüber hinaus verbessert der zusätzliche Freiheitsgrad, der durch die dreidimensionale Struktur bereitgestellt wird, die optische Leistung der Metafläche. Wir glauben, dass nanogedruckte 3D-Metaoptiken signifikante Anwendungen

in der Faseroptik und anderen fortschrittlichen optischen Systemen haben werden.

Diese Arbeit ist in sechs Kapitel gegliedert. Kapitel 1 bietet einen Überblick über die Geschichte und Anwendungen von Metaoberflächen und hebt drei repräsentative Forschungsfelder hervor, die mit dieser Studie in Zusammenhang stehen. Kapitel 2 behandelt die theoretischen Grundlagen, einschließlich der Prinzipien des 3D-Meta-Atoms und der verwendeten Simulationsmethoden. Kapitel 3 beschreibt die experimentellen und Verarbeitungsmethoden, wobei der Schwerpunkt auf dem Laser-Direktschreibsystem liegt, das zur Herstellung der 3D-Meta-Atome verwendet wird. Kapitel 4 diskutiert, wie nanogedruckte Metaflächen die Dispersion von Licht regulieren können und stellt eine achromatische Metafaser vor, die mit einer optischen Faser kombiniert ist. Kapitel 5 untersucht die Kontrolle von Phase und Polarisation des Lichts durch nanogedruckte Metaoberflächen und präsentiert eine Metafaser-Plattform, die in der Lage ist, beliebige strukturierte Lichtmuster zu erzeugen. Schließlich führt Kapitel 6 eine Polarisationsdetektionsmethode basierend auf nanogedruckten Metaflächen ein. Diese umfassende Studie zielt darauf ab, das Gebiet der optischen Materialien und Geräte durch die Nutzung der innovativen Eigenschaften nanogedruckter 3D-Metaflächen voranzubringen und neue Wege für ihre Anwendung in Spitzentechnologien zu eröffnen.

# Summary

In recent years, advancements in the study of light have significantly deepened our understanding of its properties and applications. Light, as the most ubiquitous information carrier, plays a crucial role in fields such as imaging, display, communications, and detection. The historical development of traditional optics has led to substantial achievements and innovations. However, the increasing complexity and sophistication of modern optical systems have highlighted the limitations of traditional optical components, prompting the search for novel materials and structures that can meet the growing demands for enhanced performance and functionality.

Metamaterials, which are artificial nanomaterials engineered to possess properties not found in naturally occurring substances, have emerged as a promising solution to these challenges. Unlike conventional materials, metamaterials can manipulate electromagnetic waves in ways that transcend the capabilities of traditional optics. This unique ability stems from their specialized structures, which can be designed to produce desired interactions with light. Among these metamaterials, metasurfaces have gained particular attention due to their versatile functionality and relative ease of fabrication.

Metasurfaces are essentially two-dimensional periodic nanoarrays that offer unprecedented control of light. By precisely tuning the size, shape, and arrangement of nanostructures, metasurfaces can modulate various properties of light, such as polarization, phase, and intensity. Current research and development have demonstrated the potential of metasurface-based devices in a variety of applications. For example, metasurface lenses (also known as metalenses) can focus light with high efficiency and minimal aberrations, often surpassing traditional lenses. Similarly, metasurface polarizing devices enable precise control of the polarization state of light, which is critical for imaging and telecommunications applications. The simplicity of metasurface fabrication combined with its powerful functionality makes it an attractive option for developing advanced optical devices. However, the complex processes and expensive equipment required for metasurface fabrication often limit their broader application, and the inherent limitations of two-dimensional nanostructures restrict their functionality.

In this dissertation, we propose a nanoprinted 3D metasurface based on laser direct writing technology. This new type of metasurface offers improved substrate compatibility, allowing for direct printing on various surfaces, such as the end face of an optical fiber. Moreover, the added degree of freedom provided by the three-dimensional structure enhances the optical performance of the metasurface. We believe that nanoprinted 3D meta-optics will have significant applications in fiber optics and other advanced optical systems.

This dissertation is organized into six chapters. Chapter 1 provides an overview of the history and applications of metasurfaces, highlighting three representative research fields related to this study. Chapter 2 covers the theoretical background, including the principles of the 3D meta-atom and the simulation methods used. Chapter 3 details the experimental and processing methods, focusing on the laser direct writing system employed to produce the 3D meta-atoms.

Chapter 4 discusses how nanoprinted metasurfaces can regulate the dispersion of light and introduces an achromatic metafiber combined with optical fiber. Chapter 5 explores the control of phase and polarization of light by nanoprinted metasurfaces and presents a metafiber platform capable of generating arbitrary structured light. Finally, Chapter 6 introduces a polarization detection method based on nanoprinted metasurfaces. This comprehensive study aims to advance the field of optical materials and devices by leveraging the innovative properties of nanoprinted 3D metasurfaces, opening new avenues for their application in cutting-edge technologies.

# 1. Introduction

Light, serving as one of most pervasive carriers of information in nature, has fundamentally reshaped human lifestyles and communication paradigms. The historical evolution of this transformation traces back to the 13th century when the polishing of transparent glass into lenses marked a pivotal advancement in the correction of human vision. Subsequent breakthroughs, exemplified by the invention of the telescope and microscope, granted humanity unprecedented opportunities to explore the cosmos and unravel the complexities of cellular structures.

In contemporary times, optical technology permeates every facet of daily life. The advent of advanced optical diagnostic equipment enables non-invasive diagnostic capabilities, while optical communication enhances data transmission rates over extended distances. Despite these advancements, conventional optical components face limitations, relying on thickness adjustments to control light properties, resulting in unwieldy dimensions unsuitable for modern integrated photonics.

This predicament raises a crucial question in modern optics: how can one comprehensively control all properties of light on a nanoscale and in an integrated manner? The field of nanophotonics, which has recently emerged at the intersection of nanotechnology and photonics, holds promise in solving this issue. Notably, metamaterials, playing a significant role in nanophotonics, offer an unparalleled platform for manipulating light through nanostructured materials and devices.

## 1.1 Metamaterial

When an electromagnetic wave propagates through a medium, its electric field vector, magnetic field vector, and wave vector obey the right-hand rule, which is a principle rooted in Ampere's law and forms a cornerstone of electromagnetism. In 1968, Veselago proposed that if a material exhibits negative values for both the dielectric constant and magnetic permeability, the electromagnetic wave will follow a left-handed relationship during its propagation through the material [1]. This theoretical proposition predicts a series of optical phenomena contrary to common sense, including negative refraction of light, the anomalous Doppler effect, evanescent wave amplification, the perfect lens effect, and anomalous Cherenkov radiation [2-6].

Despite the intriguing nature of these predictions, the absence of naturally occurring negative refractive index materials at that time diverted attention from this inference. In the 1990s, Pendry et al. first demonstrated that arrays composed of metal wires could produce macroscopic anomalous dielectric constants near resonant frequencies [7]. They subsequently confirmed theoretically the achievement of anomalous effective magnetic permeability by designing an artificial metal split-ring resonator (SRR) array [8]. Building on these theoretical foundations, in 2000, Smith et al. experimentally confirmed for the first time the negativity of both the permittivity and the permeability of a material. They utilized circuit board processing methods

to fabricate periodic composite structures of metal lines and SRR structures, directly observing the left-handed electromagnetic wave transmission passband and negative refraction behavior in the microwave frequency band [3]. These macroscopic composites having a man-made, three-dimensional, periodic cellular architecture designed to produce an optimized combination, not available in nature, of two or more responses to a specific excitation material with unusual properties are also defined as metamaterials [9].

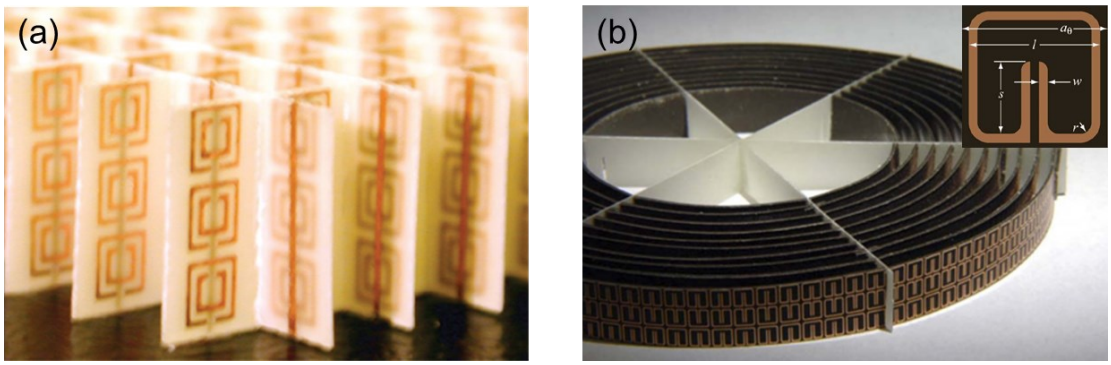


**Figure 1.1.: Photos of some metamaterial samples.** (a) Photograph of the left-handed metamaterial sample. (b) Photograph of 2D microwave cloaking structure. (insert panel: the SRR design in the cell of metamaterial) Adapted from [3] and [10].

The advent of negative refractive index metamaterials has sparked profound advancements in metamaterial research, leading to a cascade of remarkable applications based on these materials. Among these applications, one that garners the most research interest is undoubtedly cloaking. In 2006, Pendry et al. introduced a design strategy based on metamaterials for manipulating electromagnetic fields to fulfill specific requirements, which provided a theoretical framework for the implementation of optical cloaking [11]. On this basis, Schurig et al. designed a copper metamaterial array, as shown in Figure 1.1 (b), and successfully demonstrated optical cloaking experimentally [10]. Furthermore, metamaterials have found applications in creating superlens imaging beyond the diffraction limit [6, 12], as well as achieving perfect electromagnetic absorbers with ultra-high efficiency [13, 14].

While metamaterials offer access to distinctive physical phenomena and applications due to their unique optical properties, they are facing several challenges. Most of metamaterials are made of metal, leading to substantial electromagnetic losses and rendering them hard to apply in visible range. On the other hand, metamaterials, as complex three-dimensional micro-nano structures, encounter issues related to complex technological processes and difficulties in large-scale processing during the manufacturing phase. In response to these challenges, a kind of two-dimensional nanostructures, referred to as metasurfaces, were designed.

## 1.2 Planar metasurface

Similar to metamaterials, metasurfaces are also artificial periodic nanostructures with unique physical properties. However, in contrast to metamaterials, metasurfaces are two-dimensional structures, making them easier to process and integrate, thereby providing broader development prospects. Consequently, metasurfaces are also called planar metasurfaces. Based on the

different materials and principles that constitute them, metasurfaces can be divided into metallic metasurfaces and dielectric metasurfaces.

## Metallic metasurfaces

Early research on metasurfaces mainly focused on metallic materials. A seminal contribution to the field of metasurfaces was made by Capasso et al., who introduced a metasurface featuring a gold V shape structure capable of controlling wavefronts and elucidated the underlying principles of wavefront manipulation [15]. (Figure 1.2) Incident light on the metasurface induces various resonance modes in the V-shaped structure, leading to a phase shift upon their coupling. Leveraging this phase shift, they designed nanostructures of diverse shapes and sizes to achieve phase control capabilities spanning from 0 to 2π.

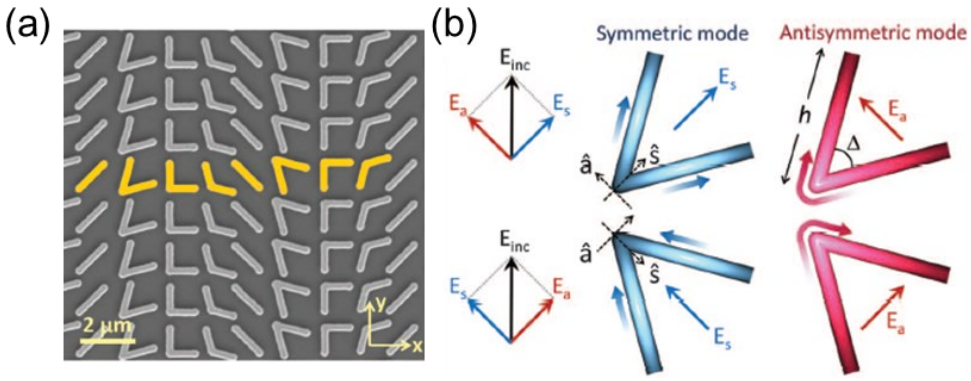


**Figure 1.2.: A V-shape surface plasmonic metasurface.** (a) The SEM image of V-shape metasurface (b) Symmetric and antisymmetric modes supported by metasurface. Adapted from [15].

Babinet's principle reveals that two complementary patterns produce the same diffraction pattern, so replacing nanoantennas with nanovoids in a metal film of the same structure can also control light. Building upon this concept, Ni et al. introduced a metalens in 2013 with an ability to focus visible light [16]. (Figure 1.3a) These metasurfaces composed of metal oscillators are based on surface plasmon resonance, so they are also referred to as a Surface Plasmonic Metasurface (SPM).

Another category of metallic metasurfaces is known as Gap-Surface Plasmon Metasurfaces (GSPM), featuring a Metal-Insulator-Metal (MIM) sandwich structure. As shown in Figure 1.3b, GSPM consists of two infinitely long gold strips separated by a layer of silicon dioxide with a thickness $d$. Due to the terminations of the MIM structure, multiple reflections of GSP modes can be realized, leading to the formation of lateral standing-wave modes. Therefore, these modes can be described succinctly with a simple Fabry-Perot resonator formula [17]:

$$w\frac{2\pi}{\lambda_0}n_{GSP} = m\pi - \varphi, \qquad (1-1)$$

where $\lambda_0$is the wavelength of incident light, $w$ is the strip width, $n_{GSP}$ is the effective index for GSP modes, $m$ is an integer order of the GSP mode, and $\varphi$ is an additional phase shift caused

by GSPM. By properly tuning the dimensions according to equation (1-1), GSP resonance at ~800 nm can be achieved with a gap size of $d = 50$ nm, which shows a dominant scattering process, making this structure a good candidate for reflective metasurfaces (Figure 1.3c). Additionally, the GSP mode shows magnetic dipole (MD) resonance properties due to the presence of out-of-phase currents in the two metal strips. Compared with SPM, GSPM is favored because it supports MD mode and can achieve 0-2π phase control, leading to wider applications. However, given the high reflectivity of the metal at the bottom of the MIM, these metasurfaces predominantly serve as reflective devices.

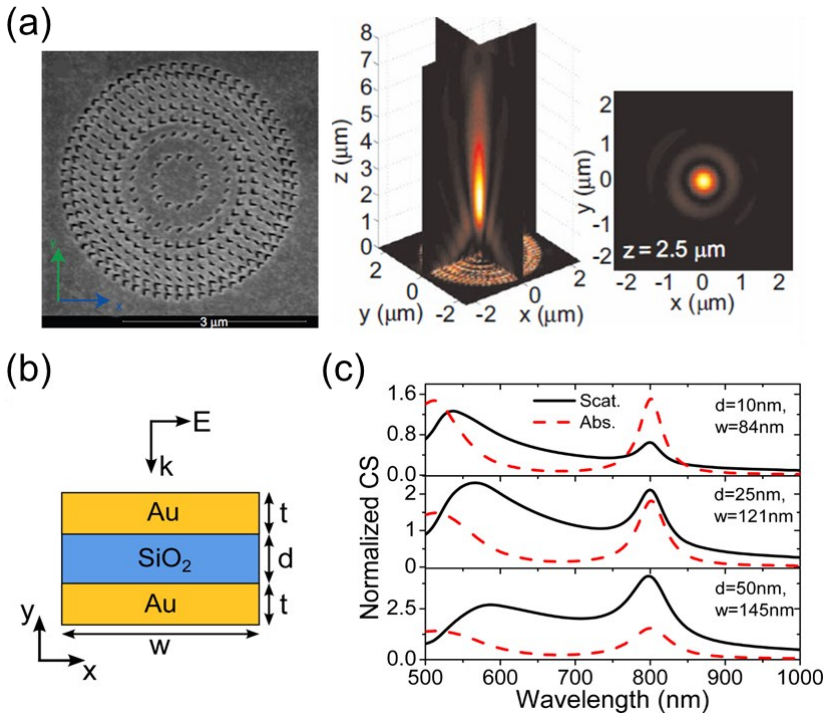


**Figure 1.3.: Different types of metallic metasurface devices.** (a) A metallic metalens based on Babinet's principle. (b) Schematic of a gap-surface plasmon metasurfaces with a typical gold-silica-gold layers. (c) normalized scattering and absorption cross sections with different $w$ and $d$. Adapted from [16] and [17].

It is important to note that metallic metasurfaces do not possess the capability to direct manipulate the light field. Instead, when light illuminates the nanoantenna, the electromagnetic field resonates with the free electrons on the metal surface, exciting surface plasmons. Subsequently, these surface plasmons are scattered by the structure and become into photons again. The process of converting photons to plasma and back to photons is accompanied by the modulation of phase and amplitude induced by resonant mode coupling. This is also the reason for the high loss of metallic metasurface devices.

## Dielectric metasurfaces

While metallic metasurfaces have achieved notable successes in manipulating wavefronts, they encounter several challenges in practical applications. Foremost among these challenges is the efficiency issue. The interaction of light with metal often results in thermal effects and energy

loss, leading to low efficiency of metallic metasurface devices. On the other hand, the requirement for resonance with the eigenfrequency of the metal limits the ability of metallic metasurfaces to operate across a broad range of wavelengths. Therefore, high refractive index dielectric materials have attracted the attention of metasurface research due to their advantages in low loss and wide spectrum coverage.

A dielectric is an electrical insulator susceptible to polarization under an applied electric field. When light illuminates on dielectric materials, the photons don't excite plasma because dielectric materials don't have free electrons like metals. Instead, due to polarization effects, electric dipoles (magnetic dipoles) and higher-order modes are generated inside the structure, which can be described by Mie scattering theory. Therefore, dielectric metasurfaces could achieve a high efficiency (>80%) compared to metallic metasurface. As dielectric materials can support both electric and magnetic dipoles, they can be regarded as a Huygens source and called as Huygens metasurface. In addition, people have also used dielectric materials with different band gaps to realize metasurfaces that operate from ultraviolet to mid-infrared, which greatly expands the potential applications of metasurfaces [18-21]. (Figure 1.4) Due to their excellent optical control capabilities and good compatibility with silicon, dielectric materials are called the preferred materials for metasurfaces and are widely used in modern optical systems.

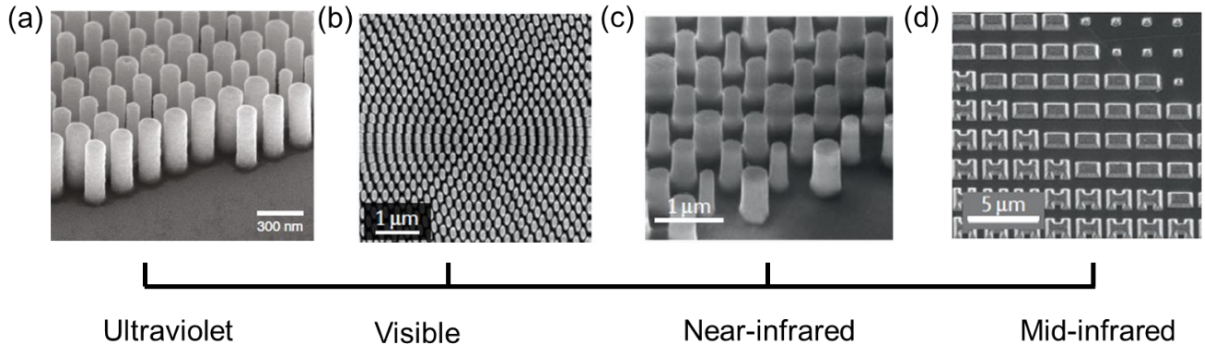


**Figure 1.4.: All-dielectric metasurfaces operating in the ultraviolet to infrared band.** (a) A $HfO_2$ metasurface operating in the ultraviolet range. (b) A GaN metasurface operating in the visible range. (c) A α-Silicon metasurface operating in the near-infrared range. (d) A PbTe metasurface operating in the mid-infrared range. Adapted from [18-21].

## 1.3 Hight aspect ratio metasurface

For Huygens metasurfaces, their ability to control light fields comes from the changes in the shape and size of the nanostructure. As the demand for advanced optics grows, the complexity of metasurface structures continues to increase, posing significant challenges to fabrication accuracy. On the other hand, the fabrication of Huygens metasurfaces involves multiple material depositions and etchings, leading to a highly intricate processing procedure. To address these challenges, the concept of high aspect ratio dielectric metasurfaces has been proposed.

High aspect ratio metasurfaces (HARM) consist of nanostructures with heights exceeding the wavelength of light, allowing light to complete a full propagation cycle within the metasurface.

Consequently, this metasurface can be regarded as a waveguide structure. In this approach, the focus is not on delving into the complex electromagnetic field distribution within meta-atoms, but rather on the phase changes induced by the metasurface. The phase transition caused by meta-atoms satisfies the following relationship:

$$\varphi = \frac{2\pi n_{eff}}{\lambda} H, \qquad (1-2)$$

where $\lambda$ is the wavelength of light, $n_{eff}$ is the effective refractive index at the wavelength of $\lambda$ and $H$ is the height of meta-atom. I It's noteworthy that the phase change no longer necessitates considering complex mode coupling; rather, it relies on the effective refractive index and the height of the nanostructure. This significantly simplifies the design of metasurfaces especially in wavefront control.

Robert C. Devlin and colleagues were the first to utilize atomic layer deposition technology to fabricate a metasurface comprised of high aspect ratio $TiO_2$ nanofins [22]. (Figure 1.5a) As depicted in Figure 1.5b, the designed nanofin exhibits anisotropy, resulting in a phase difference of π between the x and z components of the electric field at the wavelength of 480nm. (Here the propagation direction of the electric field is along the y-axis.) And the metasurface functions as a half-wave plate. By introducing geometric phases, they achieved high-efficiency holographic imaging in the visible light spectrum. Furthermore, they demonstrated that by varying the size of the nanofin, HARM can achieve phase coverage ranging from 0 to 2π.

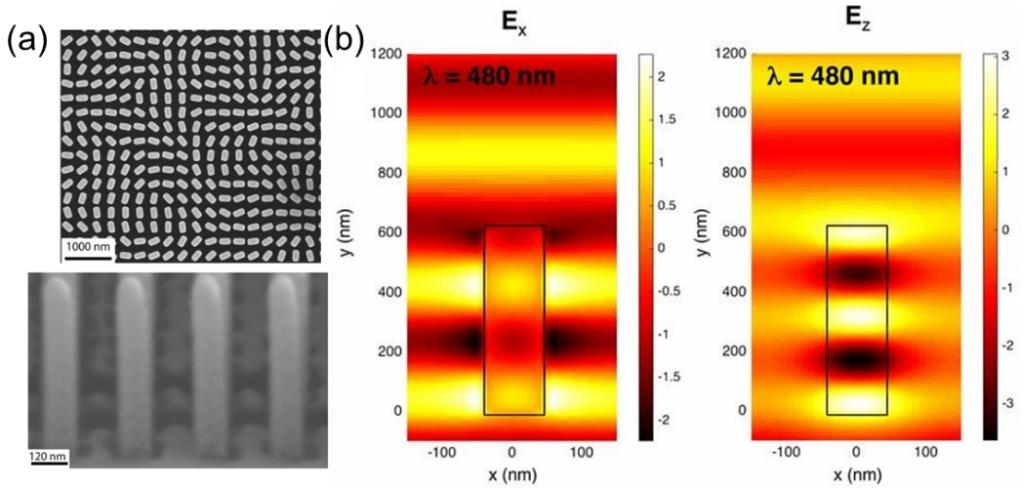


**Figure 1.5.: A TiO2 high aspect ratio metasurface.** (a) SEM image of the $TiO_2$ nanofin. (b) The components of the electric field in the x and z directions of a nanofin with incident light of 480 nm. Adapted from [22].

## 1.4 Geometric phase metasurface

Light manipulation in metasurfaces, whether utilizing metallic metasurfaces based on surface plasmon resonance or dielectric metasurfaces relying on Mie resonance, hinges on the mutual coupling of internal eigenmodes. This control primarily involves manipulating the shape and size of each meta-atom. Another pivotal method to induce phase control in metasurfaces involves introducing geometric phase by rotating a single meta-atom. This kind of metasurface

that uses geometric phase to regulate light is called geometric phase metasurface.

The concept of geometric phase originated from quantum mechanics. In 1984, Berry proposed a general description of geometric phase: when a quantum system in an eigenstate is slowly transported around a circuit $C$ by varying parameters $R$ in its Hamiltonian $H(R)$, it will acquire a geometrical phase factor [23]. In 1956, while studying the interference between different polarized light waves, Pancharatnam observed a phase shift occurring when the polarization of the photon beam cyclically changes [24]. Subsequently, Berry proved that this phase change stems from adiabatic evolution in the quantum system, thus naming it the Pancharatnam-Berry (PB) phase.

Geometric phase in optics is attributed to the spin-orbit interaction of photons. It can be described by the cyclic evolution process of the polarization state on the Poincaré sphere. Consider an anisotropic meta-atom, depicted in Figure 1.6a, capable of converting left-handed polarized light (LCP) into right-handed polarized light (RCP). An angle $\alpha$ exists between the meta-atom and the optical axis. As shown in Figure 1.6b, during the cross-polarization change from RCP to LCP, the evolution can follow either path C1 or C2. Between these two distinct evolutionary paths, a geometric phase arises, with a magnitude equal to half the solid angle $\Omega = 2\alpha$ it encompasses.

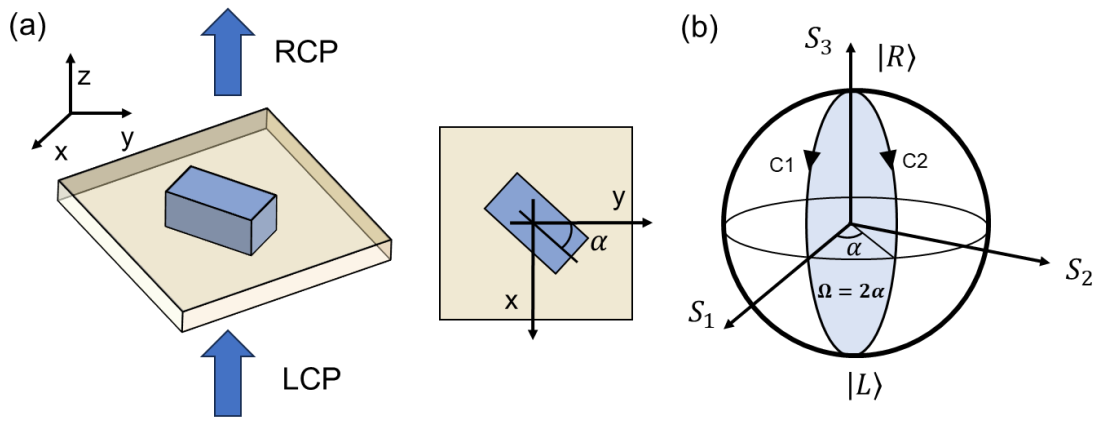


**Figure 1.6.: Schematic diagram of geometric phase principle.** (a) Anisotropic meta-atom producing geometric phase. (b) PB phase on Poincaré sphere, which equals half the solid angle (Ω) subtended at the origin by the area enclosed by the closed curves (C1 and C2) on the Poincaré sphere.

Obviously, the geometric phase is related to the polarization evolution of light, offering metasurfaces a novel degree of freedom in manipulating electromagnetic waves and significantly augmenting their capabilities. Furthermore, as the geometric phase is independent of the material and structure of the scatterer, achieving ultra-high-efficiency metasurface devices becomes possible by introducing the geometric phase into high-efficiency dielectrics. Currently, hybrid metasurfaces, which incorporate geometric phases, are considered the preferred choice for metasurface devices owing to their exceptional optical properties.

## 1.5 Metasurface-based optical device.

Metasurfaces have indeed emerged as versatile tools in contemporary optical systems, offering powerful light manipulation capabilities, superior optical properties, and integration. Their widespread application spans fields including imaging [25-27], holography [28-30], optical cloaking [31-33], optical communications [34-37], polarization conversion [38, 39], and quantum computing [40-42]. In the subsequent section, based on the research relevance of the paper, we will review the research development status and related applications of metasurfaces in metalenses, vortex beam generators, and polarization devices.

**Metalenses**

Among traditional optical devices, lenses with the function of focusing light play a pivotal role in optical systems. With a history spanning hundreds of years, these lenses have found applications in various aspects of our daily lives. However, these conventional optical devices are usually bulky, heavy, and costly due to the diffraction limit requirement and long optical path for phase manipulation, which has made them unsuitable in modern electronic and photonic systems with demands for miniaturization and integration. Furthermore, the fabrication of these lenses, whether refractive or reflective, relies on traditional technologies and molding methods, further constraining their development. Metasurfaces have become ideal candidates to replace traditional optical devices due to their excellent ability to manipulate light and the great advantages in miniaturization and integration.

In earlier metalens studies, the achievement of light focusing through plasmonic metasurfaces was demonstrated via amplitude modulation and strategic spatial design of plasmonic apertures [43, 44]. However, these plasmonic metasurfaces faced efficiency challenges attributed to metal losses. A significant milestone emerged when Mark Brongersma et al. introduced an all-dielectric planar device with phase manipulation capabilities in 2013 [45]. They designed and fabricated a silicon planar metasurface structure functioning as a half-wave plate. (Figure 1.7a) Through rotating metasurfaces, geometric phases were introduced, and devices with grating and focusing capabilities were successfully realized. Subsequently, Capasso et al. demonstrated a high numerical aperture metasurface lens operating in the visible light band [46]. As shown in Figure 1.7b, the metalens, composed of $TiO_2$ nanofins, utilizes geometric phase for phase control. The metalens reaches diffraction limited focal spots with an 86% efficiency, demonstrating the potential in areas such as optical lithography, laser microscopy and spectroscopy.

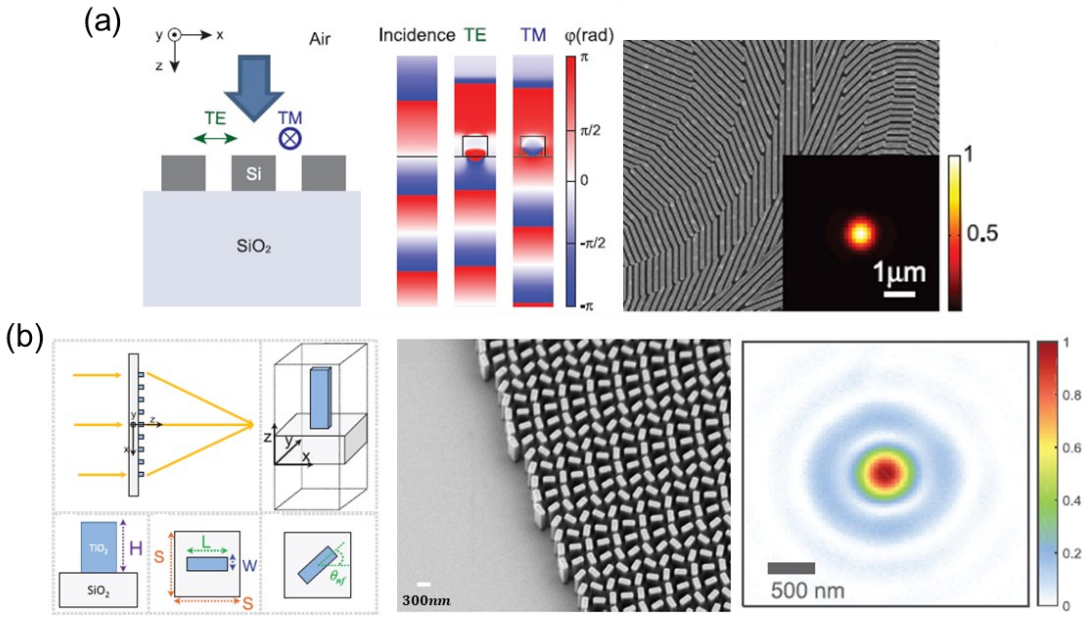


**Figure 1.7.: Dielectric metalenses.** (a) An all-dielectric metalens made of silicon. (b) A high efficiency diffraction-limited metalens operating in the visible light band. Adapted from [45] and [46].

Dispersion is an inevitable challenge in optical imaging systems, primarily stemming from the variation in refractive index within optical materials across different wavelengths. This characteristic prevents light of diverse wavelengths from converging to a single point, thereby diminishing imaging quality. In conventional imaging systems, the approach to mitigating chromatic aberration involves employing a lens group consisting of multiple lenses, which hinders the miniaturization of optical systems. Achromatic metalenses provide a strategy to replace complex multiple lenses with single planar optical devices, offering robust support for on-chip optical systems, quantum communications, and various other fields. As depicted in Figure 1.8a, a metallic metalens based on the MIM structure was introduced in 2015, highlighting the significant potential of metalenses in dispersion engineering [47]. As dispersion is the first derivative of refractive index with respect to wavelength, which can be described by Group Delay (GD), achromatic metalenses must possess the capability to independently control both phase and group delay. Therefore, this achromatic metalens employs two nanostructures within a single periodic unit, allowing for simultaneous and independent control of both phase and dispersion and successful enabling achromatic focusing in the near-infrared range. Subsequently, akin principles were applied to propose an all-dielectric achromatic metalens, as shown in Figure 1.8b. Another complementary nanopillar made of GaN also achieves achromatic imaging in the visible range [48]. Independent control of phase and GD was attained by adding an auxiliary nanopillar [49]. These all-dielectric achromatic metalenses prove efficient in focusing and imaging in the visible range.

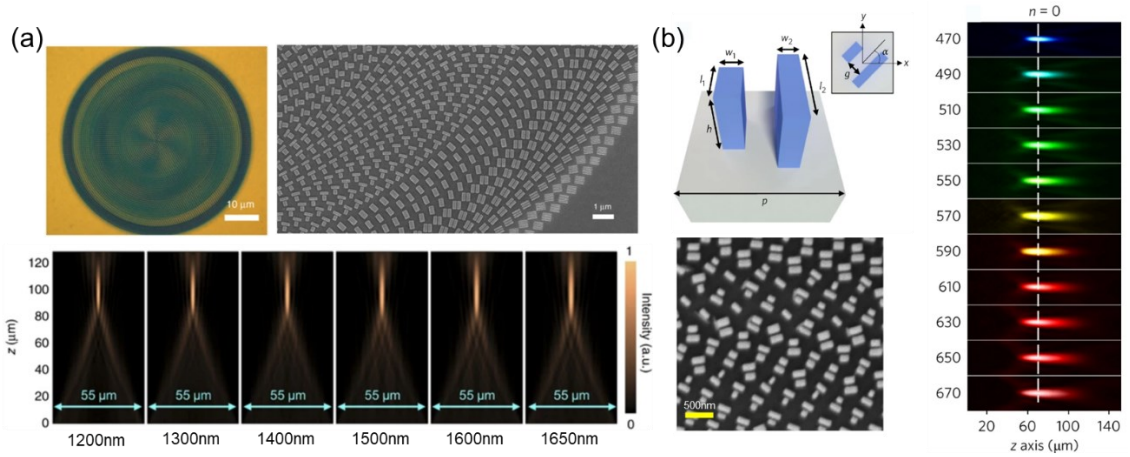


**Figure 1.8.: Achromatic metalenses.** (a) A MIM structure achromatic metalens working in the infrared band. (b) A dielectric achromatic metalens works in the visible light band. Adapted from [47] and [49].

As research on the design and production processes of metalenses becomes increasingly mature, metalenses have demonstrated the potential to replace commercial lenses in various applications. For instance, Li Tao et al. demonstrated a wide-angle imaging lens using a metalens array [50]. By carefully designing the wavefront, the metalens array efficiently gathers light from various incident angles and seamlessly stitches them into a comprehensive image, achieving lossless wide-angle imaging with a viewing angle of 60°. Moreover, the compact size and lightweight nature of metasurfaces make them advantageous in aerospace applications, where reducing the weight of optical equipment is crucial. To address this, Joon-Suh Park et al. utilized deep ultraviolet (DUV) technology to manufacture a 100mm diameter metalens, enabling high-quality imaging in the visible light band [51].

Another promising commercial application of metasurfaces is in emerging optical devices such as augmented reality (AR) and virtual reality (VR). Zhaoyi Li et al. demonstrated advancements in both AR and VR systems using an RGB-achromatic transmissive metalens [52]. In VR systems, the metalens was designed to magnify the displayed image in front of a human's eyeball, while in AR systems, it facilitated the seamless integration of virtual objects into the real scene using an optical combiner like a beam splitter. The achromatic metalenses enabled the display of three-primary-color images for both VR and AR applications, showcasing their potential in enhancing AR/VR experiences with improved image quality and color fidelity.

### Vortex beam generators

In the field of communications, various properties of light (such as intensity, polarization, etc.) are used to carry information. However, these characteristics limit the development of optical communications due to problems such as information transmission accuracy and communication capacity. In 1992, Allen et al. made a groundbreaking discovery—photons with a spiral phase $\exp(il\zeta)$ can carry orbital angular momentum of order $l$, where $\zeta$ represents the azimuthal angle of an Orbital Angular Momentum (OAM) beam [53]. Unlike other light properties, the orbital angular momentum of light theoretically possesses an infinite order, allowing for the encoding of unlimited information into the OAM. More strikingly, all OAM

eigen-states are mutually orthogonal, opening the possibility of using OAM modes as independent information channels to carry optical information with negligible crosstalk. Therefore, in the last decade, OAM multiplexing has attracted a great deal of attention for high-capacity optical and quantum communications [54, 55], and the OAM of light holds great promise to significantly improve the capacity of optical devices and systems.

In traditional optical systems, the generation of an OAM-carrying optical vortex beam often rely on free-space optics utilizing refractive or diffractive optical elements like cylindrical lenses [53], computer-generated holograms [56, 57], and spiral phase plates [58]. However, the considerable footprint of these optical devices poses challenges for achieving photonic integration. Planar metasurfaces, with their robust optical manipulation capabilities, have emerged as an ideal solution for generating vortex light, owing to their compact size and weight. Capasso et al., in their demonstration of metallic plasmonic metasurfaces for wavefront manipulation, also pioneered a vortex beam emitter. They achieved this by utilizing a V-shaped metasurface to generate a vortex beam m with the order of +1 [15].

In addition, metallic metasurfaces can also generate vortex light by introducing geometric phases. The geometric phase offers an accurate phase manipulation approach through the spin-to-orbit conversion that couples an incident circularly polarized beam into an opposite helicity. Due to total angular momentum conservation, the incident spin angular momentum of a circularly polarized light changes its helicity after passing through the geometric metasurface, giving rise to an OAM state with $l = \pm 2$ in the cross-polarization state. As such, a plasmonic geometric metasurface made of L-shaped plasmonic nanostructures was used to create an optical vortex beam with $l = \pm 2$, as illustrated in Figure 1.9 [59]. Here the geometric metasurface with strong circular birefringence acts as a spin-to-orbit angular momentum conversion plate. In general, one metasurface imprinted with a single spiral phase pattern can only create a given OAM state, limiting its application prospects.

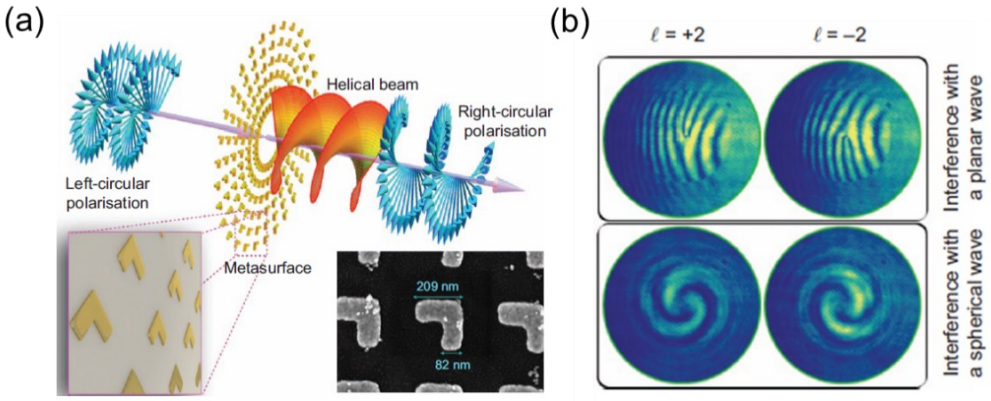


**Figure 1.9.: A spin-to-orbital conversion L-shape metasurface.** (a) Schematic diagram of OAM generation through geometric phase. Insert panel: SEM image of metasurface. (b) Interference pattern of the generated OAM mode ($l = \pm 2$). Adapted from [59].

Since plasmonic metasurfaces based on noble metals are limited by substantial material losses in the UV and visible spectral ranges due to interband transitions, all-dielectric metasurfaces based on Mie resonance and geometric phase principles have recently attracted considerable attention in optical vortex generation. A notable milestone in this realm is the recent

development of J-plates (J representing total angular momentum), showcasing dielectric metasurfaces' potential for optical vortex generation. Unlike q-plate metasurfaces generating an optical vortex beam with only two possible OAM states of $l = \pm 2$, J-plate metasurfaces can imprint an arbitrary vortex phase to the coupled circular polarization states. The basic principle of a J-plate is based on the simultaneous modulation of both propagation phase and geometric phase responses of a meta-atom. This allows the geometric phase principle to be extended from circular polarization states to any orthogonal polarization states, and each state can carry an arbitrary OAM state. As an example, Figure 1.10 shows that two orthogonal elliptical polarization states of an incident optical beam can carry different OAM states with $l = +2$ and $+3$ after passing through a J-plate metasurface [60].

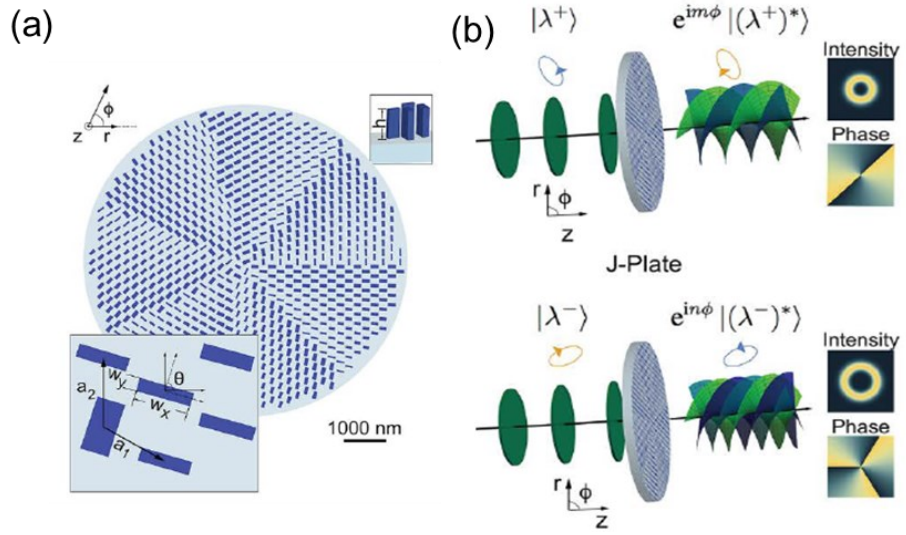


**Figure 1.10.: A J-plate metasurface based on a new concept of arbitrary spin-orbit conversion.** (a) Schematic image of J-plate (b) Schematic diagram of J-plate that generates different angular momentum for different incident lights**.** Adapted from [60].

**Polarization devices**

In classical electromagnetism, light is considered as a wave, with the vibration direction of the light field vector being perpendicular to the propagation direction of the light wave. This fundamental property is termed the polarization property of light. Similar to other light properties such as intensity and phase, polarization can function as a carrier and encoder of information. Currently, a diverse array of polarization-related applications based on metasurfaces, focused on achieving miniaturization and enhancing the functionality of various optical system components, have emerged. Particularly noteworthy is the fact that the polarization characteristics of light scattered by an object can provide insights into details about the object's contour, roughness, material type, and other pertinent information. As a result, imaging technology founded on polarization detection exhibits considerable potential across various domains including target detection, environmental monitoring, underwater imaging, biological imaging, and more. Metasurfaces have emerged as an ideal option for modern polarizing optical devices, owing to their exceptional optical properties, compact size, and ease of integration.

One notable application is polarization detection. In conventional optical polarization detection

methods, the measurement system typically comprises discrete optical components, leading to a complex setup that necessitates multiple measurements (usually 4 or 6 measurements). Utilizing unique polarization control capabilities and multifunctional integration, metasurfaces can obtain polarization information in just one measurement, that strongly simplifying the process and making it an attractive polarization detection platform.

Ming Zhao et al. introduced a theoretical method for measuring polarization using metasurfaces [61]. In Figure 1.11a, a metasurface pixel is partitioned into four regions, enabling the separation of four distinct polarizations in space: horizontal (H), vertical (V), +45-degree, and left circularly polarized (LCP) components. The strengths of these polarizations can be detected individually. By measuring and analyzing the intensities of these four polarization states, the Stokes parameters of the metasurface can be derived, which facilitates the determination of the polarization state of the incident light. Moreover, the metasurface also integrates a focusing function to improve detection accuracy.

Compared with measuring 4 polarization states, metasurfaces that can measure 6 polarization states have higher measurement accuracy and more powerful measurement capabilities. In Figure 1.11b, Yang et al. illustrate a generalized Hartmann–Shack array based on 2 × 3 sub-arrays of all-dielectric transmission-mode metalenses [62]. Each of the six distinct metalenses in every sub-array is capable of detecting specific polarizations, including horizontal linear polarization ("x"), vertical linear polarization ("y"), diagonal linear polarization ("a"), 90 degrees rotated diagonal polarization ("b"), as well as left-handed circular polarization ("l") and right-handed circular polarization ("r"). This arrangement enables comprehensive determination of the Stokes parameters in each pixel of the array. In addition, the metasurface links the phase to the spatial displacement of the focus. By measuring the focal intensity and spatial information in six sub-arrays, the polarization and wavefront of the incident light can be inversely calculated simultaneously.

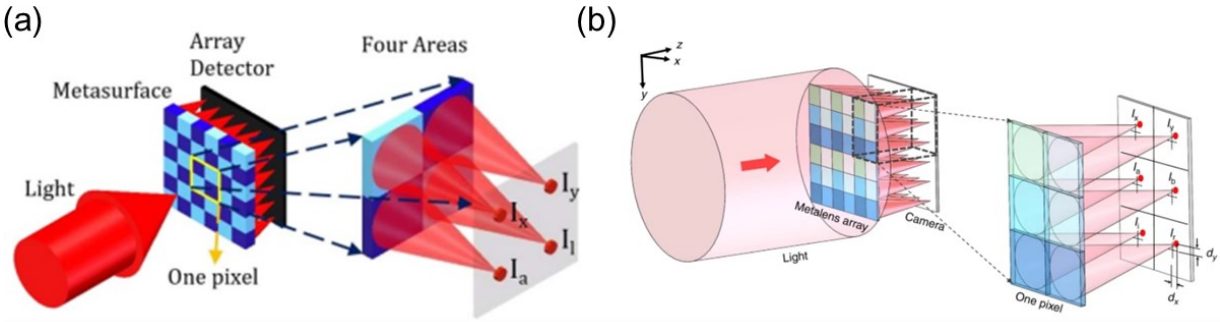


**Figure 1.11.: Polarization detection metasurface.** (a) A four-channel polarization measurement metasurface strategy (b) A Hartmann–Shack metasurface with simultaneous measurement of phase and polarization information. Adapted from [61] and [62].

After the successful application of metasurfaces in detecting polarization, the next natural progression was to design and develop metasurface-based polarization cameras. As depicted in Figure 1.12, Capasso et al. devised a metasurface grating-based full-Stokes polarization camera [63]. They employed matrix Fourier optical processing to fabricate metasurface gratings, seamlessly integrating them into the camera. This polarization camera, devoid of moving parts, is capable of capturing the complete polarization information of light and facilitating imaging.

The camera employs an array of subwavelength-spaced titanium dioxide nanopillars to form a metasurface diffraction grating. Each grating's design, based on matrix Fourier optics, is anisotropic. As polarized light traverses through various gratings, images corresponding to the Stokes vector parameter directions manifest on the imaging sensor. Polarization imaging is achieved by amalgamating images containing information in four polarization directions.

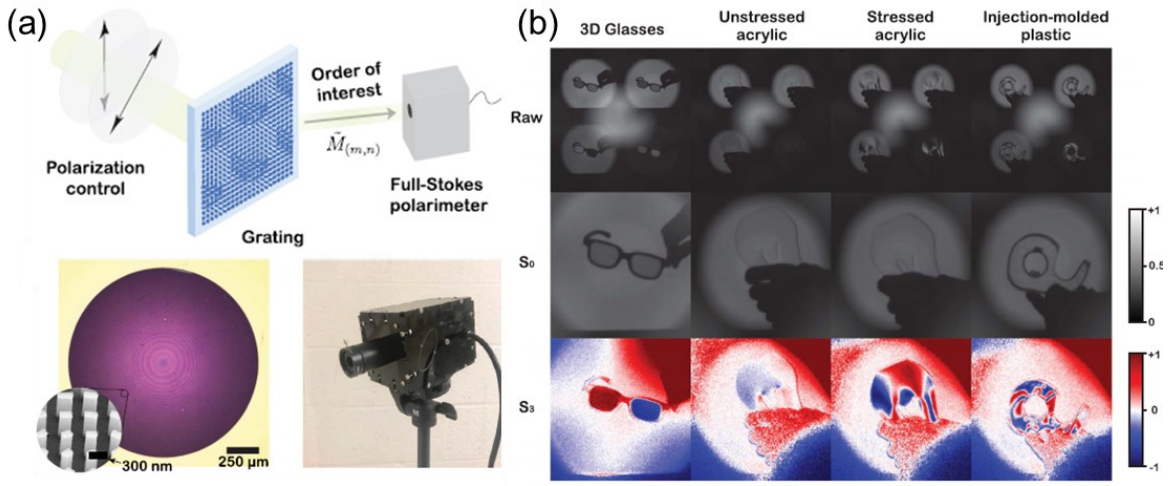


**Figure 1.12.: A metasurface-based polarization camera.** (a) Schematic diagram of polarization camera. Bottom panel: pictures of the metasurface and the camera (b) Imaging based on different polarizations. Adapted from [63].

## 1.6 Direct laser writing based on two photon polymerizations.

In the fabrication processes, a high precision metasurface device needs to be fabricated under a complex process with multiple steps such as material deposition, electron beam lithography, hard mask deposition, etching, and lift-off. This complexity requires expensive equipment and time-consuming processes. Furthermore, the intricate process flow prevents the direct production of nanostructures on optical devices such as optical fiber and vertical cavity surface emitting laser, which hinders further miniaturization of devices. On the other hand, the material of metasurface is deposited by thermal evaporation or sputtering that only allow for the creation of 2D devices (the height cannot be freely adjusted) with limited structural complexity, which strongly limits metasurface performance. A technology called direct laser writing (DLW) offers a solution by enabling the direct processing of 3D nanostructures on the device surface, effectively overcoming these shortcomings.

The principle of DLW is very similar to that of photolithography, where exposure and development are utilized to fabricate geometric structures on photosensitive materials. However, DLW primarily utilizes a negative photoresist, which retains only the illuminated area—a process known as photon polymerization. During printing, the photosensitive material absorbs incident photon energy in the exposed areas, triggering polymerization and forming structures on the substrate, while the unexposed areas dissolve in the developer and are subsequently washed away during the development process. The construction of the three-

dimensional structure involves dividing it into multiple layers and superimposing the scanned two-dimensional layers. Therefore, an independent 3D structure is formed on the substrate after the exposure and development steps. However, the diffraction limit of the lens and the typical focal spot size, often a few microns, pose constraints on conventional single-photon polymerization, rendering it unsuitable for processing nanoscale structures.

In a groundbreaking development in 1997, Maruo et al. introduced the concept of two-photon polymerization (TPP), revolutionizing the precision and control achievable in creating nanoscale features [64]. During the TPP process, nonlinear effects occur, and only a minute polymer at the focus undergoes a polymerization reaction. This unique characteristic empowers DLW based on TPP to surpass the diffraction limit, enabling the generation of structures at the 200nm scale. However, the processing accuracy of DLW faces challenges due to the diffraction effect of the optical system and the internal proximity effect within the photoresist material. Figure 1.13 shows the principle of single-photon absorption and two-photon absorption, as well as the three-dimensional structure printed by two-photon absorption [65, 66].

To overcome these limitations and further enhance writing resolution, researchers drew inspiration from Stimulated Emission Depletion (STED) microscopy technology and introduced a direct writing method called Photoinhibition Lithography, a super-resolution based on the edge light inhibition effect. This innovative approach aims to surmount the diffraction effect and alleviate the proximity effect. The incorporation of super-resolution direct writing technology has significantly improved the processing accuracy of two-photon direct writing, achieving resolutions as fine as 10nm [67-69].

On the other hand, the manufacture of three-dimensional structures through DLW faces challenges in terms of scalability due to the necessity of layer-by-layer scanning with a single focus, making it less suitable for large-area production when compared to conventional lithography. Nonetheless, DLW has seen advancements with the introduction of various techniques such as multi-focus printing [70], surface projection printing [71], and volume projection printing [72], which can significantly enhance the speed of manufacturing processing. As a result, DLW technology has achieved success in diverse applications such as photonic metamaterials [73, 74], optical data storage [75], biomedicine [76] and in vivo imaging [77-79] due to its distinctive features, including sub-micron resolution and the ability to create three-dimensional structures.

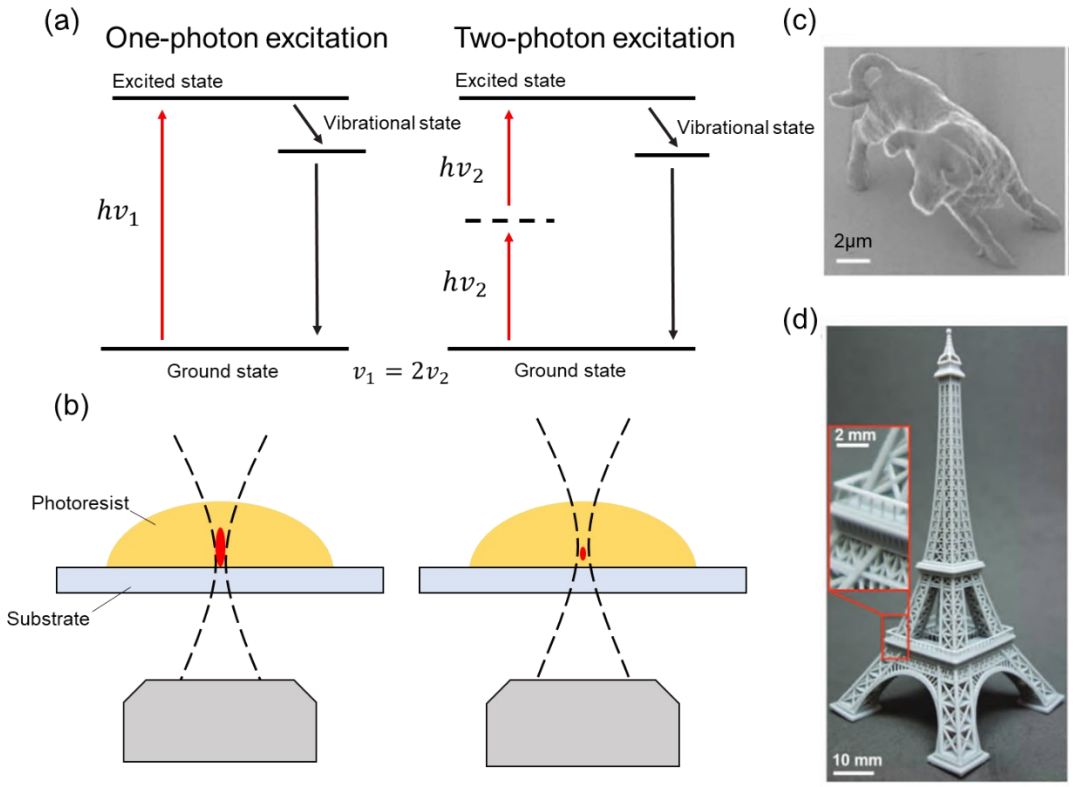


**Figure 1.13.: The principle of DLW based on single and two-photon absorption polymerization and printed 3D structures.** (a) Schematic diagram of single and two-photon absorption energy level transitions and photopolymerization reaction process. (b) Schematic diagram of DLW for single and two-photon absorption polymerization. (The red spot is the area where polymerization occurs). (c) and (d) 3D Bull and Eiffel Tower printed by DLW. Adapted from [65] and [66].

## 1.7 Direct laser writing nanophotonic devices.

The principal advantage of DLW technology lies in its capability to generate intricate 3D structures that are unattainable through alternative processing methods. For example, M. Wegener et al. utilized DLW to print a three-dimensional mold and integrated it with electrochemical deposition technology to fabricate the chiral structure illustrated in Figure 1.14a [80]. This achievement marked a significant milestone in the fabrication of devices through DLW in the field of nanophotonics.

The incorporation of a 3D structure also enhances the optical manipulation capabilities of the nanoprinted metasurface. Haoran Ren et al. demonstrated a metasurface utilizing DLW technology for orbital angular momentum holography, exhibiting the capacity to multiplex up to 200 independent orbital angular momentum channels [81]. This achievement involves designing a complex amplitude metasurface in momentum space, enabling complete and independent manipulation of amplitude and phase. The diverse orbital angular momentum patterns of light are then leveraged to extract information through Fourier transform, allowing for lensless reconstruction and display of holographic video.

Additionally, DLW technology contributes to the realization of nanoscale devices consisting of multi-layer structures, enabling the creation of multifunctional optical devices. Illustrated in Figure 1.14.b is a demonstration of a high numerical aperture (NA), broadband, and polarization-insensitive achromatic metalens with a three-layer structure [82]. The multi-layer achromatic lens, developed through inverse engineering, boast a diameter of 20 µm and operate within the visible range of 400 to 800 nm, featuring a NA of 0.5 and 0.7 to ensure high efficiency, reaching up to 42%.

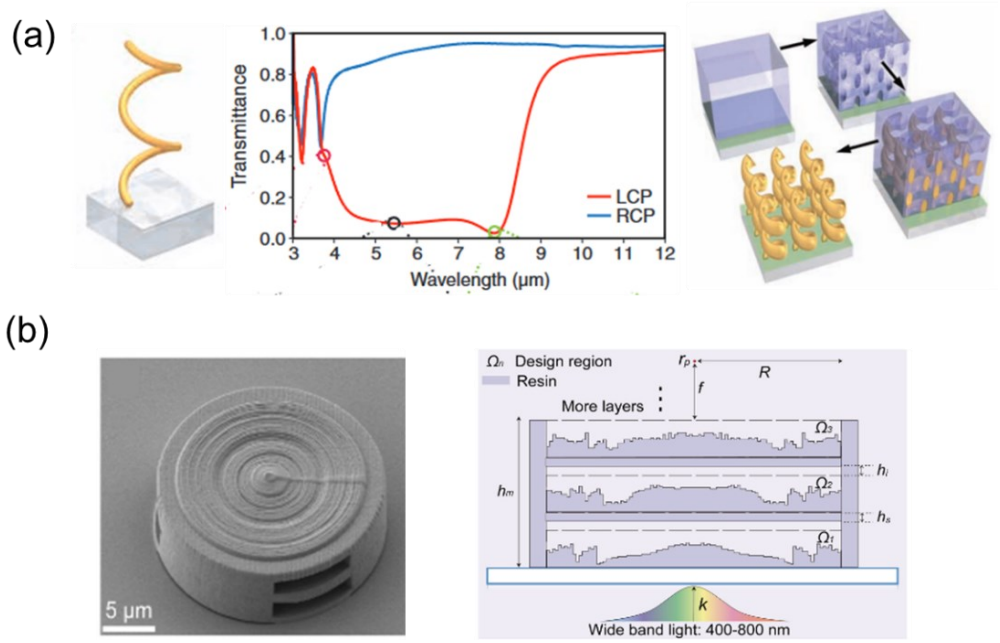


**Figure 1.14.: Nanophotonic devices fabricated from DLW.** (a) A chiral nanostructure fabricated by DLW. (b) A multi-layer lens made using DLW. Adapted from [80] and [82].

Indeed, DLW technology offers the advantage of printing nanostructures directly onto various optical devices, such as optical fibers or chips. This capability significantly enhances the integration potential of metasurfaces. In particular, the direct printing of metasurfaces on the end face of optical fibers enables direct control of light output from the fiber, paving the way for highly integrated optical systems.

Harald Giessen et al. demonstrated ultracompact multi-lens with excellent imaging effects and successfully used DLW to print directly on the fiber end face as depicted in Figure 1.15a [83]. In 2021, Malte and collaborators designed metalenses with a high Numerical Aperture (NA) of 0.88, achieving performance close to the diffraction limit [84]. (Figure 1.15b) This highlights the unique capabilities of these flexible, cost-effective, and bio- and fiber-optic circuit-compatible metafiber devices. By combining a single-mode optical fiber with diffractive optics, they effectively captured microbeads and bacteria, showcasing the diverse applications of such technology.

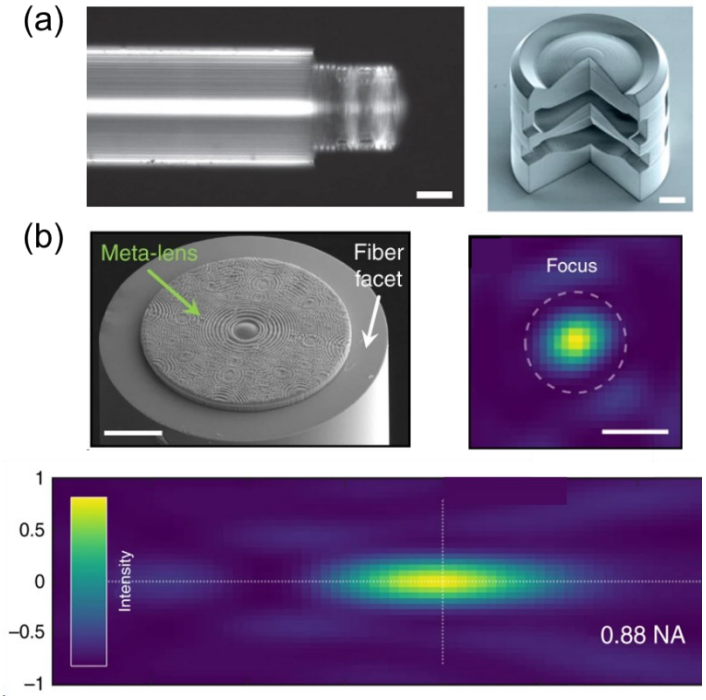


**Figure 1.15.: Nanophotonic devices fabricated on the end face of optical fiber using DLW technology.** (a) A Triplet lens printed on the end of fiber end. (b) A high NA lens printed on the laser end face that can be used for optical tweezers. Adapted from [83] and [84].

# 2. Theory

*The upcoming chapter introduces the theoretical foundation of dielectric metasurfaces and outlines the principles of numerical simulation methods. The derivations and explanations in this chapter are directly sourced from relevant textbooks [85, 86] and papers [87, 88].*

Chapter 1 offers a comprehensive examination of the historical evolution of metasurfaces and their contemporary applications in optics. The central objective of this chapter is to delve into the intricate physics underpinning metasurfaces. Firstly, we introduce the phase discontinuity phenomenon induced by metasurfaces, expounding upon the principles governing phase discontinuities arising from various metasurface typologies. After that, an in-depth exploration of the physical principles governing phase discontinuity engendered by 3D dielectric metasurfaces, substantiated by numerical simulation methodologies. Finally, the chapter elucidates the foundational principles underpinning the two numerical simulation methods employed throughout this thesis.

## 2.1 Generalized Snell's law of refraction.

When light is incident obliquely from one medium to another, its direction of propagation changes, a phenomenon commonly referred to as the refraction of light. Snell first summarized this rule to describe this phenomenon with the following relationship:

$$n_1 \sin(\theta_1) = n_2 \sin(\theta_2), \qquad (2-1)$$

where $n_1$ and $n_2$ represent the refractive index of the respective medium, and $\theta_1$ and $\theta_2$ are the angles of incidence and refraction, respectively. The elucidation of the law of refraction can be derived from Fermat's principle. As illustrated in Figure 2.1, light propagates from point A of medium 1 to point B of medium 2 with an incident angle $\theta_1$. Assuming that the two paths are infinitesimally close to the actual light path, and $dx$ is the distance between them. According to Fermat's principle that can be stated as the principle of stationary phase, the law of refraction can be written as:

$$k_0 n_1 \sin(\theta_1) dx - k_0 n_2 \sin(\theta_2) dx = 0, \qquad (2-2)$$

where $k_0 = \frac{2\pi}{\lambda_0}$ is the wave vector of the propagating light in vacuum. As indicated by Equation (2-2), the direction of light refraction is intricately linked to the refractive index of the medium, a fundamental property of the material. This implies that once the medium is determined, the corresponding direction of refraction becomes unequivocally defined. However, in 2011, Capasso et al. highlighted a noteworthy exception [15]. They pointed out that V-shaped metallic nanoantennas possess the capability to induce phase discontinuity, consequently altering the refraction direction of light. These nanostructures, referred to as metasurfaces, usher in a new era in the manipulation of light.

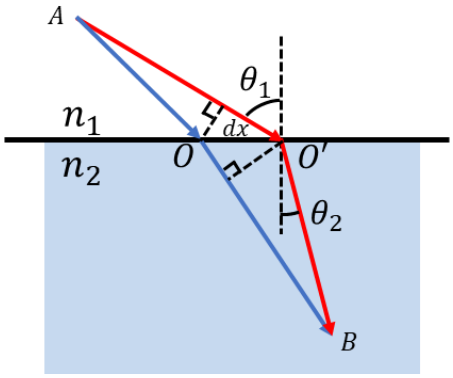


**Figure 2.1.: Schematics of the Snell's law.**

Figure 2.2 illustrates a distinctive phenomenon known as negative refraction induced by metasurfaces. Imagine a scenario where a metasurface is situated at the boundary of two media, and metasurfaces of varying shapes and dimensions yield different phase discontinuity. Let $\varphi$ and $\varphi + d\varphi$ represent the phase changes introduced by the metasurface at points $O$ and $O'$, respectively. At this juncture, in compliance with Fermat's principle, the light should adhere to:

$$[[k_0 n_1 \sin(\theta_1)dx + \varphi] - [k_0 n_2 \sin(\theta_2)dx + \varphi + d\varphi] = 0, \qquad (2-3)$$

Here, it should be noted that when negative refraction occurs, as shown in the figure, the refraction angle $\theta_2$ in Equation should be considered negative.

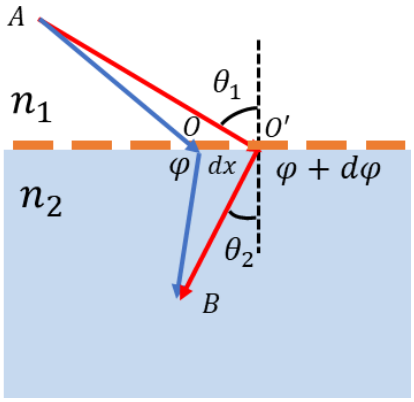


**Figure 2.2.: Schematic used to derive the generalized Snell's law.**

If the phase gradient along the interface is constant, Eq (2-3) leads to the generalized Snell's law of refraction.

$$n_2 \sin(\theta_2) - n_1 \sin(\theta_1) = \frac{\lambda_0}{2\pi}\frac{d\varphi}{dx}. \qquad (2-4)$$

## 2.2 Phase discontinuity in metasurface

According to the generalized Snell's law, the manipulation of wavefronts using metasurfaces hinges on phase alterations. Hence, a thorough examination of the physical mechanisms governing light field manipulation by nanoparticles becomes imperative. Notably, the principles underlying phase alterations vary across metasurfaces crafted from diverse materials.

For metallic metasurfaces, the underlying principle predominantly revolves around surface plasmon resonance. Within metal surfaces, a layer of free electrons exists. When incident light frequency coincides with the intrinsic frequency of these electrons, surface plasmons become activated on the metal surface. Conceptually akin to an electric dipole, this activation allows for modulation of both amplitude and phase of light. Nonetheless, metallic metasurfaces encounter efficiency challenges stemming from photoelectric conversion within surface plasmon resonance phenomena.

For dielectric metasurfaces, the principle is Mie resonance. When light irradiates dielectric materials, it will cause polarization phenomena, and the electromagnetic field distribution inside the nanostructure can be described by dipole coupling of different orders. Because both electric and magnetic fields are supported in the dielectric metasurface, it is also more efficient.

In the realm of high aspect ratio metasurfaces, while internal modes can be analyzed through Mie resonance, the elongated cross-sectional geometry engenders intricacies that render internal modes exceedingly complex. Consequently, such metasurfaces can be conceptualized as waveguides (refer to Figure 2.3). Upon incidence of light onto the metasurface, owing to the higher refractive index of the medium relative to air, total internal reflection occurs at the waveguide interface, facilitating light propagation within the waveguide. The phase of the outgoing light is contingent upon its distance traversed within the waveguide. Thus, manipulation of the height of the high aspect ratio metasurface directly governs the phase of the emitted light.

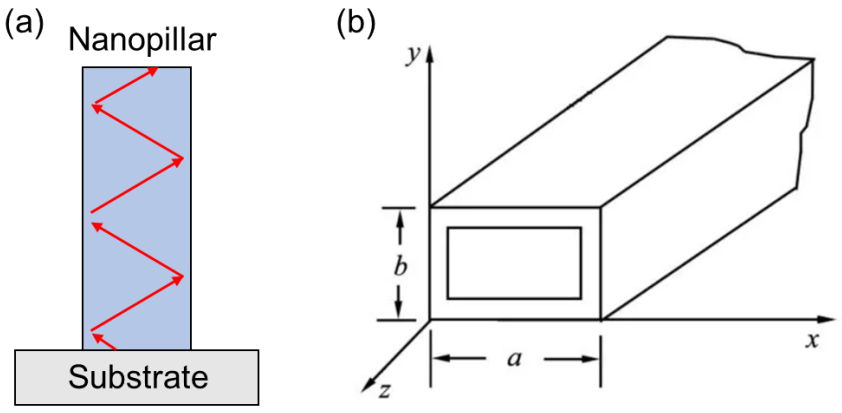


**Figure 2.3.: Schematic of the principle of high aspect ratio metasurface.** (a) Total reflection of light in high aspect ratio metasurfaces (b) Rectangular waveguide mode that can be used to simulate high aspect ratio metasurfaces

## 2.3 Waveguide theory.

A waveguide is a structure comprised of layers of materials with varying refractive indexes, facilitating the transmission of optical signals. Waveguide theory elucidates the principles governing the propagation of light within such structures. Despite the focus on a 3D meta-atom in this study, an understanding of 2D waveguide theory proves immensely beneficial. In this section, we start from the theory of light propagation, delving into the propagation modes of light waves within both 2-D and 3-D rectangular waveguides. We will theoretically explain the phase discontinuity generated by the 3-D meta-atom. Furthermore, we will conduct a comparative analysis between theoretical calculations and numerical simulation results to validate the accuracy and reliability of the theoretical framework.

### 2.3.1 Total refraction of light

When light transitions from one medium another, it undergoes reflection and refraction. Depending on the polarization direction of the light, it can be classified as TE-polarized or TM-polarized. Considering the scenario where TE-polarized and TM-polarized light are incident from a medium with a refractive index $n_1$ to a medium with a refractive index $n_2$ ($n_1 > n_2$), Fresnel's law provides the reflection coefficients for TE-polarized and TM-polarized light:

$$r_{\mathrm{TE}} = \frac{n_1 \cos(\theta_1) - n_2 \cos(\theta_2)}{n_1 \cos(\theta_1) + n_2 \cos(\theta_2)}, \tag{2-5}$$

$$r_{\mathrm{TM}} = \frac{n_2 \cos(\theta_1) - n_1 \cos(\theta_2)}{n_2 \cos(\theta_1) + n_2 \cos(\theta_2)}, \tag{2-6}$$

as per Equations (2-5) and (2-6), it becomes evident that when $\theta_2 = \frac{\pi}{2}$, the reflection coefficients $r_{\mathrm{TE}}$ and $r_{\mathrm{TM}}$ both equal 1. This implies that in this critical situation, all incident light will be reflected, and the incident angle $\theta_1$ corresponds to the critical angle $\theta_c$. And when total reflection occurs ($n_1 \sin(\theta_1) > n_2$), the reflection coefficient is no longer real, which means there is a jump in the phase of the reflected light:

$$\Phi_{\mathrm{TE}} = \arctan\left(\sqrt{\frac{n_1^2 \sin^2\theta_1 - n_2^2}{n_1^2 - n_1^2 \sin^2\theta_1}}\right) \tag{2-7}$$

$$\Phi_{\mathrm{TM}} = \arctan\left[\left(\frac{n_1}{n_2}\right)^2 \sqrt{\frac{n_1^2 \sin^2\theta_1 - n_2^2}{n_1^2 - n_1^2 \sin^2\theta_1}}\right] \tag{2-8}$$

$\Phi_{\mathrm{TE}}$ and $\Phi_{\mathrm{TM}}$ represent the phase jump of TE-polarized and TM-polarized light, respectively.

### 2.3.2 2-D waveguide theory

Figure 2.4 illustrates a typical two-dimensional planar waveguide consisting of three layers of media with $n_1 > n_3 > n_2$. It is evident that when the refractive index of the core layer is the largest and the incident angle $\theta$ meets the critical condition, light will be confined within the core layer due to total reflection and propagate forward along the z-axis. The wave-vector $\boldsymbol{k}$ follows the following relationships:

$$|\boldsymbol{k}| = k_0 n_1 \tag{2-9}$$

$$\kappa = k_0 n_1 \cos\theta \tag{2-10}$$

$$\beta = k_0 n_1 \sin\theta \tag{2-11}$$

where $k_0$ represents the wave number in a vacuum, $\kappa$ and $\beta$ are the x component and z component of $\boldsymbol{k}$ respectively. Notably, since the direction of $\beta$ is the same as the direction of light propagation, it is also defined as a propagation constant.

In addition, if we consider a cross section with a constant Z, the light should satisfy the standing wave condition:

$$2\kappa h - 2\phi_{12} - 2\phi_{13} = 2m\pi, \tag{2-12}$$

where $m$ is a positive integer starting from 0, representing the order of the mode. $\phi_{12}$ and $\phi_{13}$ are the phase mutation caused by total reflection. Obviously, when $h$ is close to the wavelength, only light that satisfies a specific incident angle exists, that means the propagation of light becomes discretized and limited modes can propagate in the waveguide. For a given mode $m$, there are fixed $\beta_m$ and $\theta_m$ corresponding to it.

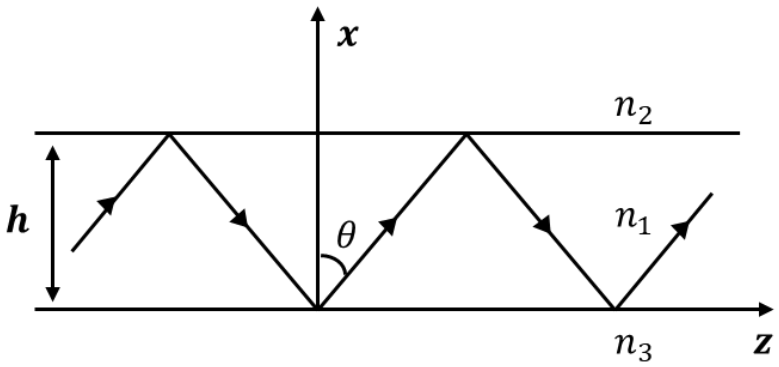


**Figure 2.4.: Schematic diagram of 2D planar waveguide**

According to equation (2-12), the characteristic equation of TE polarized light propagation in the waveguide can be obtained:

$$\kappa h = m\pi + arctan\left(\frac{p_2}{\kappa}\right) + arctan\left(\frac{p_3}{\kappa}\right) \tag{2-13}$$

For TM mode:

$$\kappa h = m\pi + arctan\left(\frac{n_1^2}{n_2^2}\frac{p_2}{\kappa}\right) + arctan\left(\frac{n_1^2}{n_3^2}\frac{p_3}{\kappa}\right) \tag{2-14}$$

Here, $p_2 = (\beta^2 - k_0^2 n_2^2)^{1/2}$, $p_3 = (\beta^2 - k_0^2 n_3^2)^{1/2}$. Obviously, there are $k_0 n_3 < \beta < k_0 n_1$. Therefore, the refractive index of the waveguide at this time can be replaced by the concept of effective refractive index $n_{eff}$, and the relationship is:

$$n_3 < n_{eff} < n_1 \tag{2-15}$$

It's worth noting that the concept of effective refractive index is widely used in waveguide theory. In particular, the phase discontinuity phenomenon produced by our 3-D meta-atom in this dissertation will also be explained by the effective refractive index.

While traditional optical theory provides an intuitive explanation of how light propagates in 2D planar waveguides, accurately determining the internal mode distribution of the waveguide and the energy carried by the mode remains a challenge. Therefore, it is imperative to reassess this paradigm from an electromagnetic perspective.

Here we consider the model in Figure 2.5. The refractive index distribution $n(x)$ in space is:

$$n(x) = \begin{cases} n_2, & h < x < +\infty \\ n_1, & 0 < x < h \\ n_3, & -\infty < x < 0 \end{cases} \tag{2-16}$$

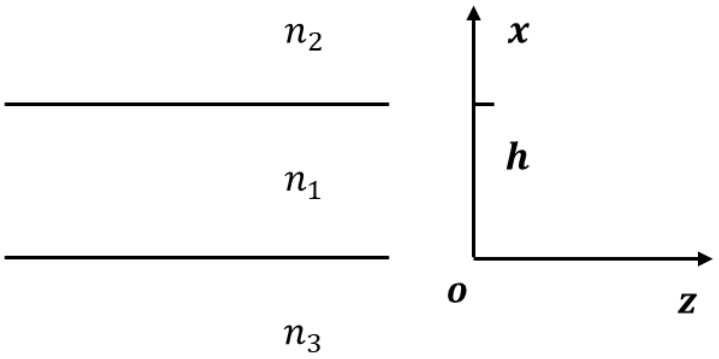


**Figure 2.5.: Schematic diagram of 2D planar waveguide**

At this time, the electromagnetic wave transmission in the planar waveguide has nothing to do with y, and the electric field $\boldsymbol{E}$ and magnetic field $\boldsymbol{H}$ distribution can be written as:

$$E(x,z,t) = E(x)\exp[i(\beta z - \omega t)] \tag{2-17}$$

$$H(x,z,t) = H(x)\exp[i(\beta z - \omega t)] \tag{2-18}$$

From Equations (2-17) and (2-18), we can write the Helmholtz equation of the electromagnetic field:

$$\frac{\partial^2 E_y}{\partial x^2} + \left(k_0^2 n_j^2 - \beta^2\right) E_y = 0 \tag{2-19}$$

$$\frac{\partial^2 H_y}{\partial x^2} + \left(k_0^2 n_j^2 - \beta^2\right) H_y = 0 \tag{2-20}$$

Mathematically, solutions to Helmholtz equation have two forms: exponential decay and oscillation. Obviously, the propagation of light in the waveguide relies on total reflection, thus

within medium 2 and medium 3, the electromagnetic field experiences exponential attenuation. Conversely, within the medium 1, the electromagnetic field can be seen as the superposition of two waves propagating in opposite directions. From this, the distribution of the electric field can be written as:

$$E_y = \begin{cases} Aexp(p_3 x), & -\infty < x < 0 \\ Bexp(i\kappa_1 x) + Cexp(-i\kappa_1 x), & 0 < x < h \\ Dexp[-p_2(x-h)], & h < x < +\infty \end{cases} \quad (2-21)$$

Using the undetermined coefficient method to solve equation 2-22, we can write the characteristic equation of equation 2-14 and 2-15. This also proves the consistency of the two methods.

## 2.3.3 3D rectangular waveguide theory

In the preceding analysis, we have illustrated that a 2D rectangular waveguide can support pure TE and TM modes. However, in the context of 3D rectangular optical waveguides, pure TE and TM modes do not exist, giving way to hybrid TEM modes polarized along the x and y directions. Therefore, the guided modes supported by 3D waveguides are classified according to whether the main electric field component lies in the x or the y direction. The mode having the main electric field Ex resembles the TM mode and is termed the TM-like mode, represented by $E_{mn}^{x}$. The subscripts $m$ and $n$ denote represent the number of maximum values of the electric field $E_x$ in the x and y direction, respectively. Similarly, the $E_{mn}^{y}$ mode (TE-like mode) has the main electric field $E_y$.( For convenience of expression, the subsequent quasi-TM and TM modes will be directly called TE and TM modes.)

In general, the hybrid TEM modes in waveguides are intricate and frequently necessitate the application of numerical simulation methods for precise solutions. However, such methods demand substantial computing power and often hinder a comprehensive understanding of the physical nature of these modes. On the contrary, approximate analysis methods provide a way to find closed-form analytical solutions. In this context, we employ the Marcatili approximation method to derive an approximate solution for the electromagnetic field distribution within a rectangular waveguide [89].

**Marcatili's method**

As shown in Figure 2.6, in the Marcatili's method, the rectangular waveguide with side lengths $a$ and $b$ is divided into 9 regions, and the mode propagating in the waveguide is assumed far from the cut-off frequency. Under this approximation, most of the energy in the guided mode is confined within the core region (region I), while outside the fiber core, the electromagnetic field experiences exponential decay in both horizontal and vertical directions. Therefore, the fields in the outer quadrants of rectangular waveguide can be ignored. Without loss of generality, we consider the refractive index in the vertical and horizontal directions are $n_2$, $n_3$, $n_4$, $n_5$ that smaller than $n_1$, respectively.

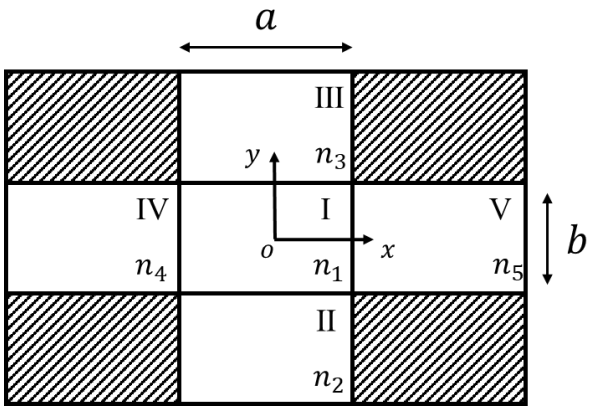


**Figure 2.6.: Schematic diagram of Marcatili approximation method**

For any wave vector, it satisfies:

$$k_x^2 + k_y^2 + k_z^2 = k^2 \qquad (2-22)$$

Obviously, the electromagnetic fields along the x and y directions should be continuous under approximate conditions, so we can obtain the following relationship:

$$k_{1x} = k_{2x} = k_{3x} = k_x \qquad (2-23)$$

$$k_{1y} = k_{4y} = k_{5y} = k_y \qquad (2-24)$$

We begin with the TM mode. According to Maxwell's curl equation in dielectrics:

$$\nabla \times \boldsymbol{E} = -i\omega\mu\boldsymbol{H} \qquad (2-25)$$

$$\nabla \times \boldsymbol{H} = i\omega\varepsilon\boldsymbol{E} \qquad (2-26)$$

Given that the principal electromagnetic field components of $E_{mn}^x$ are $E_x$ and $H_y$, we assume $H_x = 0$, component in equations (2-25) and (2-26) in Cartesian coordinates can be written:

$$\begin{cases} \dfrac{\partial E_x}{\partial y} + i\beta E_y = 0 \\ i\beta E_x + \dfrac{\partial E_z}{\partial x} = i\omega\mu H_y \\ \dfrac{\partial E_y}{\partial x} - \dfrac{\partial E_x}{\partial y} = -i\omega\mu H_z \end{cases} \qquad \begin{cases} \dfrac{\partial H_x}{\partial y} + i\beta H_y = i\omega\varepsilon E_x \\ \dfrac{\partial H_z}{\partial x} = -i\omega\varepsilon E_y \\ \dfrac{\partial H_y}{\partial x} = i\omega\varepsilon E_z \end{cases} \qquad (2-27)$$

and the wave equation of the TM mode with respect to the main magnetic field component $H_y$ is:

$$\frac{\partial^2 H_y}{\partial x^2} + \frac{\partial^2 H_y}{\partial y^2} + (k_0^2 n^2 - \beta^2) H_y = 0 \qquad (2-28)$$

Since the electromagnetic field distribution should satisfy the wave equation, and based on the above analysis, we get the magnetic field distribution in the five areas as:

$$H_y = \begin{cases} H_1 cos(k_x x + \varphi_1)\, cos\left(k_y y + \varphi_2\right) \\ H_2 cos(k_x x + \varphi_1)\, exp\left[\gamma_2\left(y + \frac{b}{2}\right)\right] \\ H_3 cos(k_x x + \varphi_1)\, exp\left[\gamma_3\left(y - \frac{b}{2}\right)\right] \\ H_4\, cos\left(k_y y + \varphi_2\right) exp\left[\gamma_4\left(x + \frac{a}{2}\right)\right] \\ H_5\, cos\left(k_y y + \varphi_2\right) exp\left[\gamma_5\left(x - \frac{a}{2}\right)\right] \end{cases} \quad (2-29)$$

Where $H_1$, $H_2$, $H_3$, $H_4$ and $H_5$ are amplitude coefficient in each region, $\varphi_1$ and $\varphi_2$ are phase factors. $\gamma$ is the attenuation coefficient and satisfy the following relations:

$$\gamma_{2,3}^2 = \left(n_1^2 - n_{2,3}^2\right)k_0^2 - k_y^2 \quad (2-30)$$

$$\gamma_{4,5}^2 = \left(n_1^2 - n_{4,5}^2\right)k_0^2 - k_x^2 \quad (2-31)$$

At the boundary $x = \pm\frac{a}{2}$, $H_y$ and $E_z$are tangentially continuous. When $x = \frac{a}{2}$, satisfy:

$$H_1 cos\left(k_x \frac{a}{2} + \varphi_1\right) = H_5 \quad (2-32)$$

$$\frac{k_x}{n_1^2} H_1 sin\left(k_x \frac{a}{2} + \varphi_1\right) = \frac{\gamma_5}{n_5^2} H_5 \quad (2-33)$$

After mathematical calculation, the characteristic equation can be written as:

$$k_x a = m\pi - arctan\left(\frac{n_5^2}{n_1^2}\frac{k_x}{\gamma_5}\right) - arctan\left(\frac{n_4^2}{n_1^2}\frac{k_x}{\gamma_4}\right) \quad (2-34)$$

Similarly, at $x = -\frac{a}{2}$, we can get characteristic equation in the y direction:

$$k_y b = n\pi - arctan\left(\frac{k_y}{\gamma_2}\right) - arctan\left(\frac{k_y}{\gamma_3}\right) \quad (2-35)$$

Here, m and n are positive integers, representing the number when the field is maximum.

We use the same method to write the characteristic equation of TE mode:

$$k_y a = m\pi - arctan\left(\frac{k_y}{\gamma_2}\right) - arctan\left(\frac{k_y}{\gamma_3}\right) \quad (2-36)$$

$$k_x b = n\pi - arctan\left(\frac{n_2^2}{n_1^2}\frac{k_x}{\gamma_4}\right) - arctan\left(\frac{n_3^2}{n_1^2}\frac{k_x}{\gamma_5}\right) \quad (2-37)$$

**Numerical simulation**

In the above, we have used the Marcatili's method to approximate the analytical solution of light propagation in a 3D rectangular waveguide. Below we take the 3D meta-atom used in this dissertation as an example to verify the correctness of the theory through numerical simulation.

We assume that the length and width of our rectangular nanopillar are 600nm, 1500nm, respectively. The refractive index of the material is $n_p = 1.5$ and the environment is air $n_a = 1$. And the attenuation coefficient $\gamma$ can be written as $\gamma_x$ and $\gamma_y$ according to the x and y directions. In this case, the characteristic equations (2-34) and (2-35) of the TM mode are:

$$k_x a = m\pi - 2arctan\left(\frac{1}{n_p^2}\frac{k_x}{\gamma_x}\right) \qquad (2-38)$$

$$k_y b = n\pi - 2arctan\left(\frac{k_y}{\gamma_y}\right) \qquad (2-39)$$

We draw equations (2-39) and (2-40) in MATLAB. The intersection in the figure is the mode in which $E_{mn}^x$ can propagate in the waveguide.

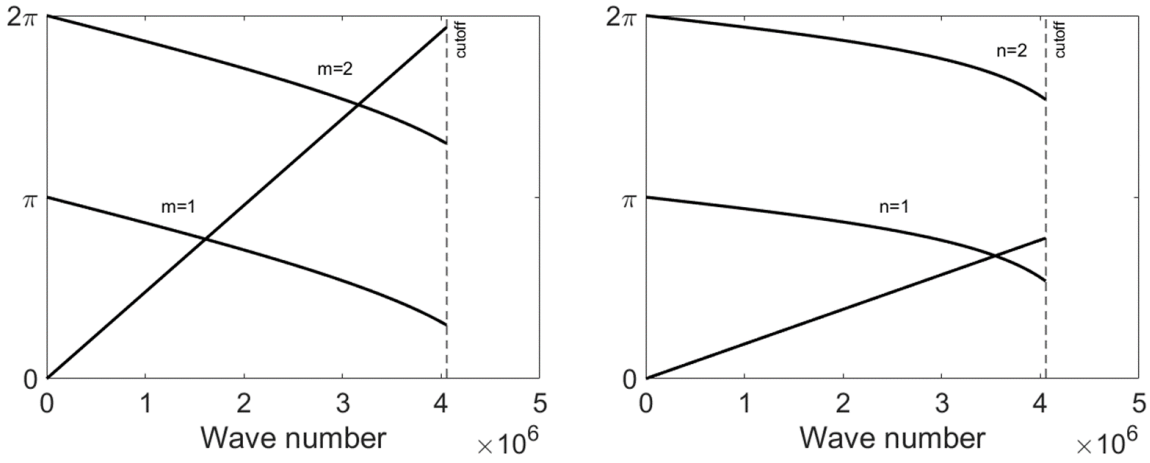


**Figure 2.7.: Solution of characteristic equation of TM mode**

From Figure 2.7, we can see that for the TM mode, there are two modes, $E_{11}^x 1$ and $E_{21}^x$, inside the waveguide. Considering that the main mode of propagation is the fundamental mode $E_{11}^x$ we can get the corresponding $k_x = 1.835e6\, m^{-1}$ and $k_y = 2.911e6\, m^{-1}$. According to Equation (2-22) and the relationship $\beta = n_{eff}k_0$we can calculate the effective refractive index of the rectangular nanopillar in the TM mode is $n_{eff} = 1.23$.

Similarly, we can use MATLAB to draw figures for TE mode. (Figure 2.8) Similar to the TM mode, its main mode of propagation is $E_{11}^y$ and the effective refractive index for TE mode is $n_{eff} = 1.15$

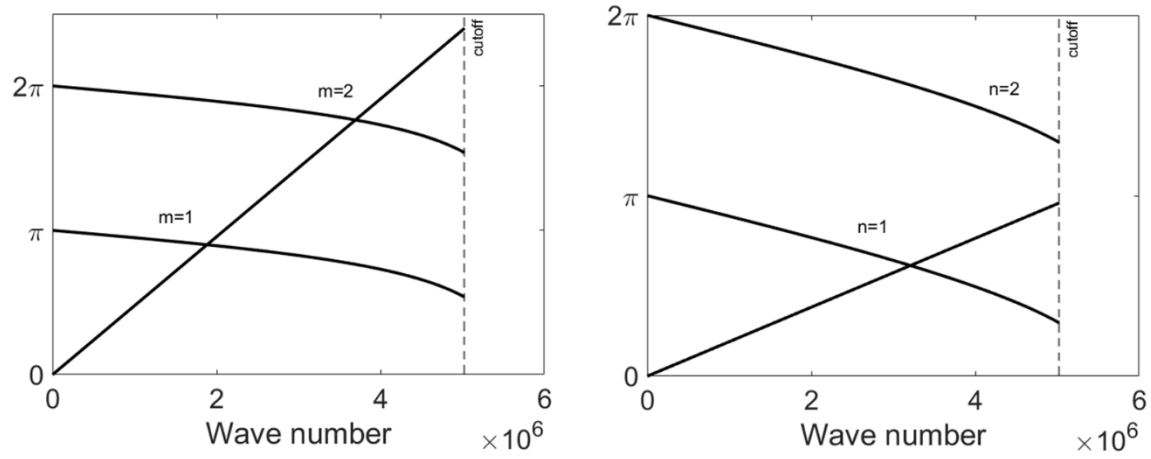


**Figure 2.8.: Solution of characteristic equation of TE mode**

Next, we use FDTD software to simulate the propagation of electromagnetic waves in the rectangular waveguide. In order to be close to the situation used in this dissertation, the rectangular waveguide was chosen to be a nanopillar with a length of 1500nm, a width of 600nm and a height of 10μm, and the boundaries were set to perfectly matched layers to simulate the situation of individual nanopillars. The simulation results of TM mode are shown in Figure 2.9. Nanopillars are highlighted with white boxes in the figure.

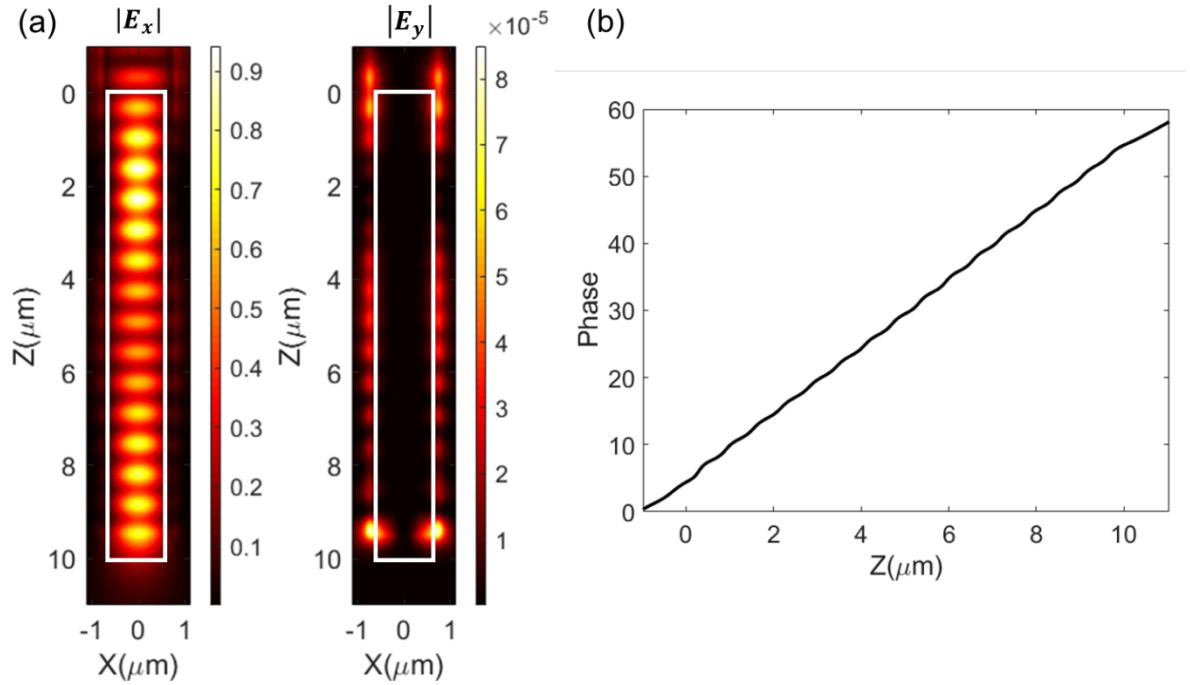


**Figure 2.9.: FDTD simulation electric field intensity distribution diagram (a) and relationship between phase change and nanopillar height (b) for TM mode.**

Figure 2.9a shows the distribution of the electric field on the XZ plane. It can be noted that in TM mode, the main component of the electric field is $E_x$, which is consistent with the theory. In Figure 2.9b, the phase of $E_x$ is illustrated, with the slope of the line segment representing the effective refractive index. Through calculation, an effective refractive index $n_{eff} = 1.24$ can

be determined.

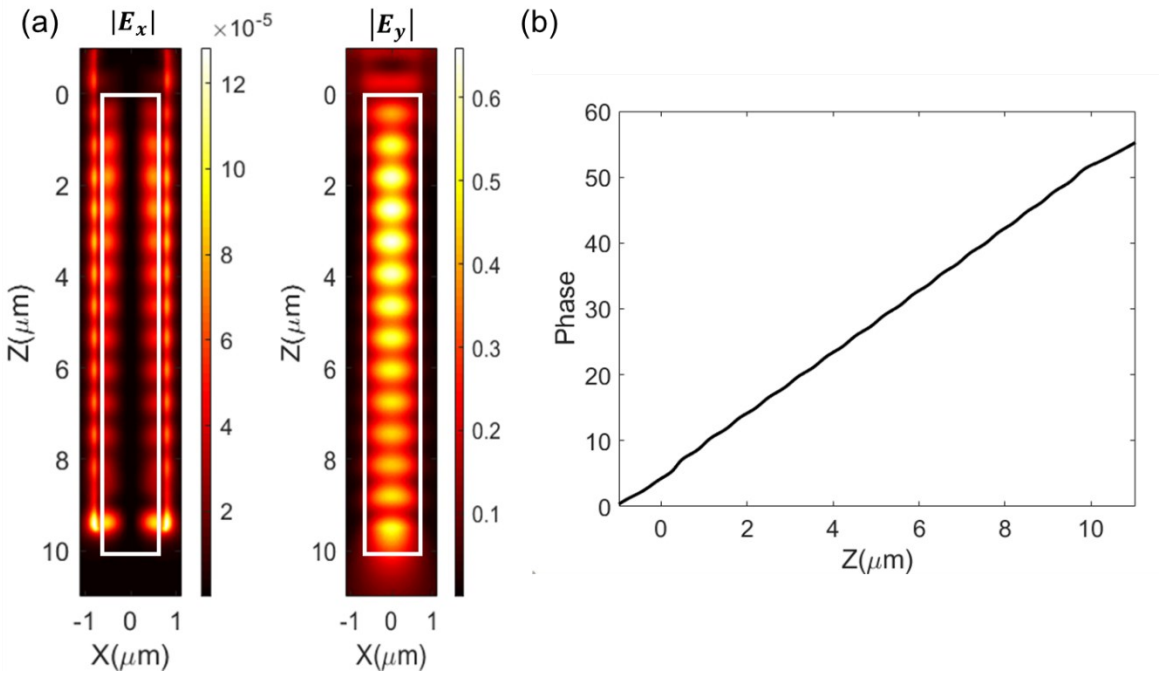


**Figure 2.10.: FDTD simulation electric field intensity distribution diagram (a) and relationship between phase change and nanopillar height (b) for TE mode.**

Similar simulation was conducted to analyze the TE mode. In this mode, the primary component of the electric field is $E_y$, and the effective refractive index is $n_{eff} = 1.16$. (Figure 2.10) These simulation results exhibit a high level of consistency with theoretical expectations.

Therefore, for our 3D rectangular meta-atom, the propagation phases of TM and TE modes can be described by:

$$\varphi_{\mathrm{TE,TM}}(\lambda, H) = \frac{2\pi}{\lambda} n_{\mathrm{TE,TM}}(\lambda) H \qquad (2-40)$$

where $\lambda$ is the wavelength of incident light and $n(\lambda)$ is the effective refractive index corresponding to the wavelength $\lambda$, and $H$ stands for the height of the 3D meta-atom. Clearly, when the lateral size of the 3D meta-atom remains constant, the effective refractive index becomes a fixed value. In this scenario, the phase is directly proportional to the height of the nanopillar.

It should be noted that waveguide theory only considers the case of a single nanopillar. The actual metasurface is a periodic structure in which electromagnetic fields between adjacent nanopillars interact, changing the effective refractive index. However, it can be seen from the simulation results that the electromagnetic field mainly propagates inside the waveguide, and the crosstalk between nanopillars can be ignored.

## 2.4 Jones matrix description of geometric phase

When the meta-atom is rotated, a phase mutation will also occur. This phase change is called

geometric phase. Its origin can be traced back to spin–orbit interaction and can be described by the Jones matrix.

We know that light of arbitrary polarization can be described by a pair of orthogonal complex vectors:

$$\boldsymbol{E} = \begin{bmatrix} \boldsymbol{E_x} \\ \boldsymbol{E_y} \end{bmatrix} \tag{2-41}$$

When light passes through a polarization-related device, the polarization state of the emitted light is:

$$\boldsymbol{E_{out}} = \boldsymbol{M}\boldsymbol{E_{inc}} \tag{2-42}$$

where $\boldsymbol{M}$ is the Jones matrix of the device. Consider the situation in Figure 2.11. The coordinates XY are the observation coordinate system, and xy is the device coordinate system where the fast axis and slow axis of the device are located. There is a rotation angle a between the two, then the transformation relationship between the two coordinate systems is as follows:

$$\begin{bmatrix} \boldsymbol{E_X} \\ \boldsymbol{E_Y} \end{bmatrix} = \boldsymbol{R}\begin{bmatrix} \boldsymbol{E_x} \\ \boldsymbol{E_y} \end{bmatrix} \tag{2-43}$$

Where $\boldsymbol{R} = \begin{bmatrix} \cos\alpha & -\sin\alpha \\ \sin\alpha & \cos\alpha \end{bmatrix}$ is the rotation matrix. So, we can get the Jones matrix of the device in the observation coordinate system:

$$\begin{bmatrix} \boldsymbol{E_X} \\ \boldsymbol{E_Y} \end{bmatrix}_{\boldsymbol{out}} = \boldsymbol{R}\boldsymbol{M}\boldsymbol{R^{-1}}\begin{bmatrix} \boldsymbol{E_X} \\ \boldsymbol{E_Y} \end{bmatrix}_{\boldsymbol{inc}} \tag{2-44}$$

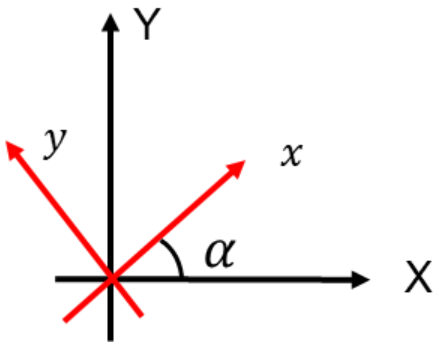


**Figure 2.11.: Coordinate rotation changes in geometric phase.**

Considering that the incident light is left-handed polarized light $\boldsymbol{E_{inc}} = \begin{bmatrix} 1 \\ i \end{bmatrix}$ and the optical device passing through is a half-wave plate, its Jones matrix $\boldsymbol{M} = \begin{bmatrix} 1 & 0 \\ 0 & -1 \end{bmatrix}$. The Jones vector of the output light is:

$$\boldsymbol{E_{out}} = e^{i2\alpha}\begin{bmatrix} 1 \\ -i \end{bmatrix} \tag{2-45}$$

It can be seen from Equation (2-45) that for left-handed polarized light, after passing through a

half-wave plate with a rotation angle of $\alpha$, it will become right-handedly polarized light and carry a phase change of $2\alpha$.

## 2.5 Numerical simulation methods

As previously mentioned, while light still adheres to macroscopic optical laws when traversing metasurfaces, it introduces a phase mutation that cannot be calculated in traditional optics. Furthermore, when facing complex nanostructures, Maxwell's equations cannot be analytically solved. Hence, the use of numerical simulation methods becomes inevitable when designing metasurfaces.

Presently, advancements in computer performance and the introduction of novel calculation methods have given rise to a diverse array of numerical simulation techniques, including Finite Difference Time Domain, Finite Element Method, Multiple-Multipole Method, and Rigorous Coupled Wave Analysis. Here, our primary focus is on introducing two specific numerical simulation methods used in this thesis: FDTD and RCWA.

### 2.5.1 Finite Difference Time Domain

Light, as an electromagnetic wave, can be accurately understood and described by Maxwell's equations. In essence, the calculation of the time-domain response of electric fields and magnetic fields at discrete points in space via Maxwell's equations facilitates an understanding of the response of arbitrary nanostructures. In 1965, Yee introduced a method known as finite difference to provide an approximate solution to Maxwell's equations, subsequently serving as the foundation for Finite Difference Time Domain (FDTD) simulations [90].

Finite-difference methods (FDM) represent a numerical technique employed for solving differential equations by approximating derivatives with finite differences. To illustrate the fundamental principle of FDM, we employ a one-dimensional function, denoted as $f(x,t)$. The Taylor's series expansion of $f(x,t)$ about the space point $x_0$ to space point $x_0+\frac{\Delta x}{2}$, and keep time fixed at $t_n$ [86]:

$$f\left(x_0+\frac{\Delta x}{2}\right)\Big|_{t_n} = f|_{x_0,t_n} + \frac{\Delta x}{2}\cdot\frac{1}{1!}\cdot\frac{\partial f}{\partial x}\Big|_{x_0,t_n} + (\frac{\Delta x}{2})^2\cdot\frac{1}{2!}\cdot\frac{\partial^2 f}{\partial x^2}\Big|_{x_0,t_n} + \cdots \qquad (2-46)$$

where $\Delta x$ is an infinitesimal quantity. The same is carried out for $x_0-\frac{\Delta x}{2}$ and let $f(x_0+\Delta x)|_{t_n}$ and $f(x_0-\Delta x)|_{t_n}$ be subtracted:

$$\frac{\partial f}{\partial x}\Big|_{x_0,t_n} = \frac{f\left(x_0+\frac{\Delta x}{2}\right)\Big|_{t_n} - f\left(x_0-\frac{\Delta x}{2}\right)\Big|_{t_n}}{\Delta x} + O(\Delta x^2) \qquad (2-47)$$

Equation 2-47 is the second-order central difference, and its accuracy is and is third-order $\Delta x$.

Therefore, in order to ensure the accuracy of calculation, x should be made as small as possible.

Now we come back to the propagation of electromagnetic fields in an isotropic material. According to Maxwell's curl equation:

$$\nabla \times \boldsymbol{H} = \varepsilon \frac{\partial \boldsymbol{E}}{\partial t} + \sigma_e \boldsymbol{E} \tag{2-48}$$

$$\nabla \times \boldsymbol{E} = -\mu \frac{\partial \boldsymbol{H}}{\partial t} - \sigma_m \boldsymbol{H} \tag{2-49}$$

Here, $\sigma_e$ and $\sigma_m$ correspond to electrical conductivity and magnetic conductivity that related to the loss of material, respectively.

Then the equations are written in the Cartesian coordinate system:

$$\begin{cases} \mu \dfrac{\partial H_x}{\partial t} = \dfrac{\partial E_y}{\partial z} - \dfrac{\partial E_z}{\partial y} - \sigma_m H_x \\ \mu \dfrac{\partial H_y}{\partial t} = \dfrac{\partial E_z}{\partial x} - \dfrac{\partial E_x}{\partial z} - \sigma_m H_y \\ \mu \dfrac{\partial H_z}{\partial t} = \dfrac{\partial E_x}{\partial y} - \dfrac{\partial E_y}{\partial x} - \sigma_m H_z \end{cases} \tag{2-50}$$

$$\begin{cases} \varepsilon \dfrac{\partial E_x}{\partial t} = \dfrac{\partial H_z}{\partial y} - \dfrac{\partial H_y}{\partial z} - \sigma_e E_x \\ \varepsilon \dfrac{\partial E_y}{\partial t} = \dfrac{\partial H_x}{\partial z} - \dfrac{\partial H_z}{\partial x} - \sigma_e E_y \\ \varepsilon \dfrac{\partial E_z}{\partial t} = \dfrac{\partial H_y}{\partial x} - \dfrac{\partial H_x}{\partial y} - \sigma_e E_y \end{cases} \tag{2-51}$$

The spatial domain is discretized into uniform rectangular cells with dimensions $\Delta x$, $\Delta y$, and $\Delta z$, as illustrated in Figure 2.12. The electric field is positioned at the midpoint of the edge, while the magnetic field is situated on the middle surface, aligning its distribution with Maxwell's equations. Simultaneously, to capture the temporal evolution of the electromagnetic field, time is discretized by $\Delta t$. The state of the electric and magnetic fields at any given point in time and space can be denoted by $(i\Delta x, j\Delta y, k\Delta z, n\Delta t)$, where $i, j, k,$ and $n$ are integers. Importantly, the electric field components are computed at times $n + \frac{1}{2}$, enabling the subsequent evaluation of the magnetic field at time $n + 1$.

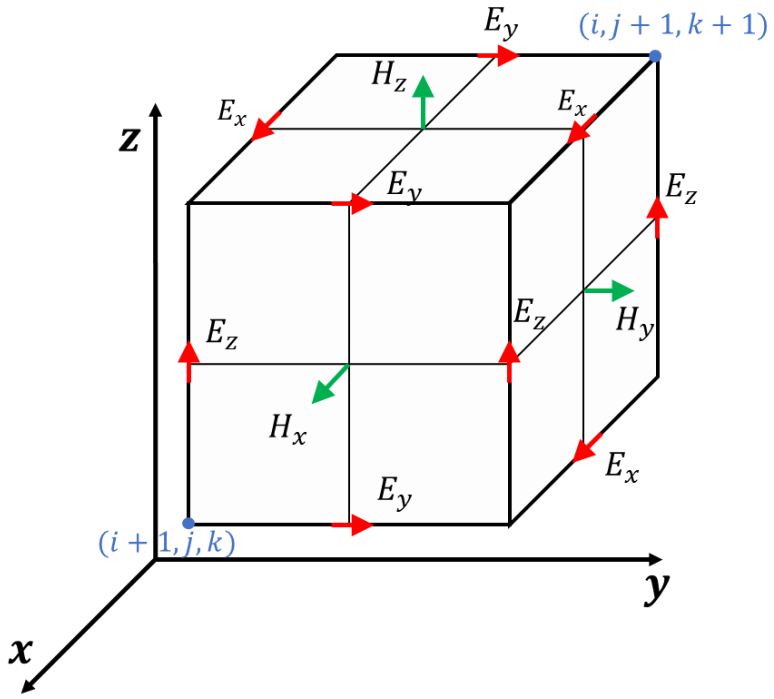


**Figure 2.12.: Diagram of the electric and magnetic fields in a Yee cell**

Use $f(x, y, z, t)$ to represent the component of $\boldsymbol{E}$ or $\boldsymbol{H}$ in the Yee cell at a certain point in time and space:

$$f(x, y, z, t) = f(i\Delta x, j\Delta y, k\Delta z, n\Delta t) = f^n(i, j, k) \qquad (2-52)$$

Take central difference approximation of $f(x, y, z, t)$ with respect to space and time respectively:

$$\left.\frac{\partial f(x, y, z, t)}{\partial x}\right|_{x=i\Delta x} = \frac{f^n\left(i+\frac{1}{2}, j, k\right) - f^n\left(i-\frac{1}{2}, j, k\right)}{\Delta x} \qquad (2-53)$$

$$\left.\frac{\partial f(x, y, z, t)}{\partial y}\right|_{y=j\Delta y} = \frac{f^n\left(i, j+\frac{1}{2}, k\right) - f^n\left(i, j-\frac{1}{2}, k\right)}{\Delta y} \qquad (2-54)$$

$$\left.\frac{\partial f(x, y, z, t)}{\partial z}\right|_{z=k\Delta z} = \frac{f^n\left(i, j, k+\frac{1}{2}\right) - f^n\left(i, j, k-\frac{1}{2}\right)}{\Delta z} \qquad (2-55)$$

$$\left.\frac{\partial f(x, y, z, t)}{\partial t}\right|_{t=n\Delta t} = \frac{f^{n+\frac{1}{2}}(i, j, k) - f^{n-\frac{1}{2}}(i, j, k)}{\Delta t} \qquad (2-56)$$

It should be noted that in order to ensure the accuracy of the central difference approximation, $\Delta x \ll \lambda$ should be satisfied. Bringing Equations (2-5) to (2-56) into Equations (2-50) and (2-51) can get the electromagnetic field distribution in the x direction:

$$E_x^{n+1}\left(i+\frac{1}{2},j,k\right)=\frac{1-\frac{\sigma_e\Delta t}{2\varepsilon}}{1+\frac{\sigma_e\Delta t}{2\varepsilon}}E_x^n\left(i+\frac{1}{2},j,k\right)$$
$$+\frac{1}{1+\frac{\sigma_e\Delta t}{2\varepsilon}}\left\{\frac{\Delta t}{\varepsilon\Delta y}\left[H_z^{n+\frac{1}{2}}\left(i+\frac{1}{2},j+\frac{1}{2},k\right)-H_z^{n+\frac{1}{2}}\left(i+\frac{1}{2},j-\frac{1}{2},k\right)\right]\right.$$
$$\left.-\frac{\Delta t}{\varepsilon\Delta z}\left[H_y^{n+\frac{1}{2}}\left(i+\frac{1}{2},j,k+\frac{1}{2}\right)-H_y^{n+\frac{1}{2}}\left(i+\frac{1}{2},j,k-\frac{1}{2}\right)\right]\right\}$$

$$H_x^{n+\frac{1}{2}}\left(i,j+\frac{1}{2},k+\frac{1}{2}\right)=\frac{1-\frac{\sigma_m\Delta t}{2\mu}}{1+\frac{\sigma_m\Delta t}{2\mu}}H_x^{n-\frac{1}{2}}\left(i,j+\frac{1}{2},k+\frac{1}{2}\right)$$
$$+\frac{1}{1+\frac{\sigma_m\Delta t}{2\mu}}\left\{\frac{\Delta t}{\mu\Delta z}\left[E_y^n\left(i,j+\frac{1}{2},k+1\right)-E_y^n\left(i,j+\frac{1}{2},k\right)\right]\right.$$
$$\left.-\frac{\Delta t}{\mu\Delta y}\left[E_z^n\left(i,j+1,k+\frac{1}{2}\right)-E_z^n\left(i,j,k+\frac{1}{2}\right)\right]\right\}$$

Similar equations describing the distribution of electric field and magnetic field along the y and z axes can be formulated.

It is imperative to highlight that the Finite-Difference Time-Domain (FDTD) method relies on discrete difference equations as a substitute for electromagnetic field differential equations. Ensuring the stability and convergence of the solutions to these discrete equations is critical to accuracy. Therefore, when discretizing space and time, it is essential that the discrete intervals adhere to the Courant stability condition:

$$c\Delta t\le\frac{1}{\sqrt{\frac{1}{(\Delta x)^2}+\frac{1}{(\Delta y)^2}+\frac{1}{(\Delta z)^2}}} \qquad (2-57)$$

When applying the FDTD for simulating practical problems, several challenges arise. In scenarios involving two materials with distinct properties, Maxwell's equations become inadequate at the boundary. A practical and effective solution to solve this problem is to employ the average values of $\varepsilon$ and $\mu$ when calculating the interface between the two media. In addition, FDTD simulations are inherently confined to limited spatial domains. Consequently, when addressing problems under unbounded regions, adding perfectly matching layers on the boundaries becomes essential. This layer serves the crucial function of absorbing signals at the boundary, thereby eliminating reflections of electromagnetic fields and ensuring the accuracy of simulation results.

The FDTD has demonstrated its efficacy in computing in most conditions. However, when confronted with complex structures, achieving accurate results with FDTD demands the utilization of very fine meshes. This, in turn, consumes significant computing resources and

prolongs simulation times. Therefore, in most of the metasurface simulations covered in this thesis, a more time-efficient simulation method, RCWA will be employed to strike a balance between computational efficiency and result accuracy.

### 2.5.2 Rigorous Coupled Wave Analysis

Rigorous Coupled Wave Analysis (RCWA) is an algorithm grounded in Fourier expansion proposed by Moharam and Gaylord in the 1980s [87, 91, 92], which is well-suited for solving periodic electromagnetic fields. As a rigorously vector-based calculation method, its precision is contingent upon the order of expanded harmonic numbers. Relative to alternative numerical calculation methods, RCWA exhibits rapid computational speed and high accuracy. Consequently, it finds widespread application in the analysis of diffraction characteristics across a spectrum of periodic structures.

In this context, we will use the one-dimensional periodic gratings depicted in Figure 2.13 as an illustrative example to understand the fundamental principles of RCWA. A linearly polarized plane wave is incident at an arbitrary angle of incidence $\theta$ and at an azimuthal angle $\phi$ upon the gratings. The grating is situated between two distinct media with refractive indices $n_{\mathrm{I}}$ and $n_{\mathrm{II}}$ and the period of grating is $\Lambda$. In the grating region (0<Z<d), the relative permittivity is periodic, so it can be expanded in a Fourier series [88]:

$$\varepsilon(x) = \sum_{h} \varepsilon_h e^{\frac{2\pi h}{\Lambda}} \qquad (2-58)$$

where $\varepsilon_h$ is the $h$th Fourier component of the relative permittivity in the grating region. For simplicity, Eq(2-58) can also be written as:

$$\varepsilon_0 = n_{rd}^2 f + n_{rg}^2 (1-f) \qquad (2-59)$$

$$\varepsilon_h = \left(n_{rd}^2 - n_{rg}^2\right) \frac{sin(\pi h f)}{\pi h} \qquad (2-60)$$

where $n_{rd}$ and $n_{rg}$ are the refractive index of ridge and groove, respectively. The parameter $f$ represents the fraction of the grating period occupied by the region with index $n_{rd}$ and $\varepsilon_0$ is the average value of the relative permittivity, not the permittivity of free space.

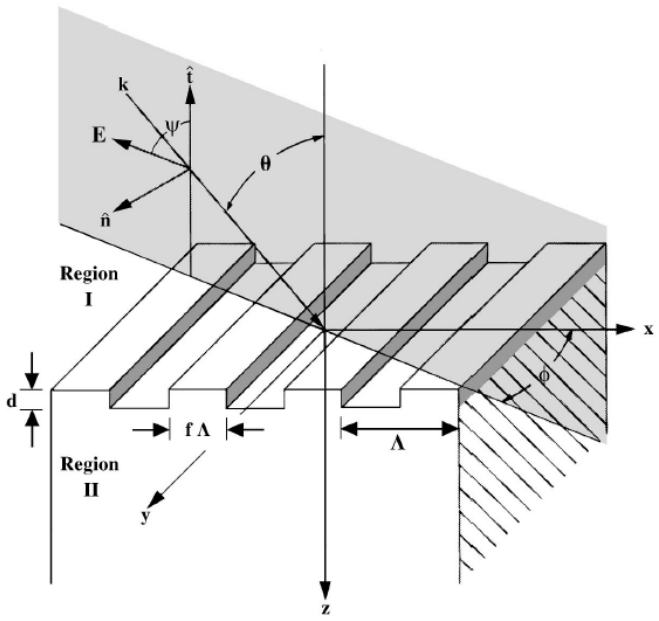


**Figure 2.13.: Geometry for the binary rectangular groove grating diffraction problem analyzed herein.**

The approach to solving the electromagnetic field distribution problem in the grating is to find solutions to Maxwell's equations within the three distinct regions (input, grating, and output), and ensure that the tangential electric field and magnetic field components at the two boundaries match. Considering that the incident plane wave can be decomposed into Transverse Electric (TE) and Transverse Magnetic (TM) polarizations, the initial focus is on the case of TE polarization incidence.

The expression for the incident normalized electric field perpendicular to the plane of incidence is:

$$E_{inc,\ y} = e^{-ik_0 n_{\mathrm{I}}[sin(\theta x)+cos(\theta z)]} \qquad (2-61)$$

Where $k_0 = \frac{2\pi}{\lambda_0}$ and $\lambda_0$ is the wavelength of the light in free space. The normalized solutions in region I and in region II are given by:

$$E_{\mathrm{I},\ y} = E_{inc,\ y} + \sum_j R_j e^{-i(k_{xj}-\mathrm{k_{I,zj}}z)} \qquad (2-62)$$

$$E_{\mathrm{II},\ y} = \sum_j T_j e^{-i[k_{xj}-k_{\mathrm{II},zj}(z-d)]} \qquad (2-63)$$

In the provided context, $j$ represents the order of diffraction, $R_j$ is the and $T_j$ are the normalized amplitudes of $i$-th order reflection in region I and transmission waves in region II, respectively. $k_{xj}$ denotes the wave vector component in the x direction.:

$$k_{xj} = k_0\left(n_1 \sin\theta - j\frac{\lambda_0}{\Lambda}\right) \quad (2-64)$$

and $k_{l,zj}$ is the wave vector component in the z direction:

$$k_{l,zj} = \begin{cases} +k_0\sqrt{n_l^2 - \left(\frac{k_{xj}}{k_0}\right)^2}, & k_0 n_l > k_{xj} \\ -ik_0\sqrt{\frac{k_{xj}}{k_0} - n_l^2}, & k_0 n_l < k_{xj} \\ & l = \mathrm{I}, \mathrm{II} \end{cases} \quad (2-65)$$

In accordance with Maxwell's equations, the magnetic field distribution in region I and region II is given by:

$$\boldsymbol{H} = \left(\frac{i}{\omega\mu}\right)\nabla \times \boldsymbol{E} \quad (2-66)$$

where $\mu$ is the permeability of the region and $\omega$ is the angular frequency of incident light.

Within the grating region, the tangential electric ($y$-component) and magnetic ($x$–component) fields are expressed with a Fourier expansion in terms of space harmonic fields:

$$E_{gy} = \sum_j S_{yj}(z)e^{-ik_{xj}x} \quad (2-67)$$

$$H_{gx} = -i\sqrt{\frac{\varepsilon_0}{\mu_0}}\sum_j U_{xj}(z)e^{-ik_{xj}x} \quad (2-68)$$

$S_{yj}(z)$ and $U_{xj}(z)$ are the normalized amplitudes of the electric field and magnetic field of the $j$-order diffracted wave respectively. The electromagnetic field distribution in the grating region is expressed by Maxwell's equations and expanded using Fourier series:

$$\frac{\partial E_{gy}}{\partial z} = i\omega\mu_0 H_{gx} \quad (2-69)$$

$$\frac{\partial H_{gx}}{\partial z} = i\omega\varepsilon_0\varepsilon(x)E_{gy} + \frac{\partial H_{gz}}{\partial x} \quad (2-70)$$

By substituting Equation (2-67) and (2-68) into Equation (2-69) and (2-70) and eliminating $H_{gz}$, we obtain the coupled-wave equations:

$$\frac{\partial S_{yj}}{\partial z} = k_0 U_{xj} \quad (2-71)$$

$$\frac{\partial U_{xj}}{\partial z} = \left(\frac{k_{xj}^2}{k_0}\right)S_{yj} - k_0\sum_p \varepsilon_{(j-p)}S_{yp} \quad (2-72)$$

The Equation (2-71) and (2-72) can be expressed in matrix form as:

$$\begin{bmatrix} \frac{\partial \boldsymbol{S}_y}{\partial(z')} \\ \frac{\partial \boldsymbol{U}_x}{\partial(z')} \end{bmatrix} = \begin{bmatrix} \boldsymbol{0} & \boldsymbol{I} \\ \boldsymbol{A} & \boldsymbol{0} \end{bmatrix} \begin{bmatrix} \boldsymbol{S}_y \\ \boldsymbol{U}_x \end{bmatrix} \tag{2-73}$$

which can be further simplified to:

$$\left[\frac{\partial^2 \boldsymbol{S}_y}{\partial(z')^2}\right] = [\boldsymbol{A}][\boldsymbol{S}_y] \tag{2-74}$$

Here, $z' = kz_0$ and $\boldsymbol{A} = \boldsymbol{K}_x^2 - \boldsymbol{E}$. $\boldsymbol{E}$ is the matrix formed by the permittivity harmonic components, with the $j, p$ element being equal to $\varepsilon_{(j-p)}$. $\boldsymbol{K}_x$ is a diagonal matrix, with the $j, j$ element being equal to $\frac{k_{xj}}{k_0}$. And $\boldsymbol{I}$ is the identity matrix.

The space harmonics of the tangential electric and magnetic fields in the grating region are then given by:

$$S_{yj}(z) = \sum_{m=1}^{n} w_{j,m}\left[c_m^+ e^{-k_0 q_m z} + c_m^- e^{k_0 q_m (z-d)}\right] \tag{2-75}$$

$$U_{xj}(z) = \sum_{m=1}^{n} v_{j,m}\left[-c_m^+ e^{-k_0 q_m z} + c_m^- e^{k_0 q_m (z-d)}\right] \tag{2-76}$$

where $w_{i,m}$ and $q_m$ are the elements of the eigenvector matrix $\boldsymbol{W}$ and the positive square root of the eigenvalues of the matrix $\boldsymbol{A}$, respectively. The quantity $v_{j,m} = q_m w_{j,m}$ is the $j$, $m$ element of the matrix $\boldsymbol{V} = \boldsymbol{WQ}$, where $\boldsymbol{Q}$ is a diagonal matrix with the elements $q_m$. The quantities $c_m^+$ and $c_m^-$ are unknown constants to be determined from the boundary conditions.

Considering the requirement for equality in the tangential components of the electric and magnetic fields at the interface, the conditions at $z = 0$ are as follows:

$$\delta_{j0} + R_j = \sum_{m=1}^{n} w_{j,m}(c_m^+ + c_m^- e^{-k_0 q_m d}) \tag{2-77}$$

$$i\left(n_{\mathrm{I}} \cos\theta\, \delta_{j0} - \frac{k_{\mathrm{I},zj}}{k_0} R_j\right) = \sum_{m=1}^{n} v_{j,m}(c_m^+ + c_m^- e^{-k_0 q_m d}) \tag{2-78}$$

Similarly, at $Z = d$:

$$T_j = \sum_{m=1}^{n} w_{j,m}(c_m^+ e^{-k_0 q_m d} + c_m^-) \tag{2-79}$$

$$i\frac{k_{\mathrm{II},zj}}{k_0}R_j = \sum_{m=1}^{n} v_{j,m}(c_m^+ e^{-k_0 q_m d} + c_m^-) \qquad (2-80)$$

where $\delta_{i0} = 1$ for $j = 0$ and $\delta_{j0} = 0$ for $j \neq 0$.

Finally, we use Equation (2-77) and (2-78) to eliminate $R_j$, Equation (2-75) and (2-76) to eliminate $T_j$, subsequently amalgamate the two sets of equations to remove the positional parameters $c_m^+$ and $c_m^-$. This systematic approach leads to the determination of the ultimate grating diffraction efficiency:

$$DE_{rj} = R_j R_j^* Re\left(\frac{k_{\mathrm{I},zj}}{k_0 n_{\mathrm{I}} cos\,\theta}\right) \qquad (2-81)$$

$$DE_{tj} = T_j T_j^* Re\left(\frac{k_{\mathrm{II},zj}}{k_0 n_{\mathrm{I}} cos\,\theta}\right) \qquad (2-82)$$

For TM-polarized light, we can employ the same methodology to derive its grating diffraction efficiency:

$$DE_{rj} = R_j R_j^* Re\left(\frac{k_{\mathrm{I},zj}}{k_0 n_{\mathrm{I}} cos\,\theta}\right) \qquad (2-83)$$

$$DE_{tj} = T_j T_j^* \frac{Re\left(\frac{k_{\mathrm{II},zj}}{n_{\mathrm{II}}^2}\right)}{\frac{k_0 cos\,\theta}{n_{\mathrm{I}}}} \qquad (2-84)$$

# 3. Methodology and experimental methods

This chapter delineates the methodology and experimental techniques utilized in the thesis. The first section elucidates the methodology and workflow applied in the context of this dissertation research project. Subsequently, attention is directed towards the 3D meta-atoms employed in this thesis, with a comprehensive exploration of their physical principles in light manipulation and numerical simulation details. The third part of the chapter is dedicated to a elaborating the fabrication process of the 3D meta-atoms, including processing flow, parameter optimization, and other pertinent experimental details.

## 3.1 General flow

Figure 3.1 provides a comprehensive overview of the research workflow outlined in this thesis, comprising five key stages: motivation, simulation calculation, metasurface device fabrication, experimental characterization, and results analysis and presentation.

The initiation of any project research is typically rooted in a specific motivation, often derived from practical problems or findings in the existing literature. When a problem is encountered or an idea is proposed, a plan is developed through a thorough review of relevant literature. In this thesis, the plans mainly revolve around designing metasurface-based optical devices tailored to meet specific requirements for achieving unique optical properties and applications.

Upon conceptualizing an idea, we initiate theoretical simulations to validate the plan's feasibility. This process typically involves two main steps. Firstly, leveraging optical principles, we derive the necessary phase or polarization distribution. Subsequently, using numerical simulation software, we systematically scan parameters such as the shape and size of nanostructures, generating a comprehensive database of optical parameters, including intensity and phase. The next step involves matching the target phase with the parameters in the database to derive the design parameters for the metasurface.

The designed metasurface is then fabricated using laser direct writing technology. The processed samples undergo optimization through morphological and optical characterization to ensure that the actual samples achieve the desired light field distribution. Following fabrication, optical characterization is conducted to detect and assess the optical properties and performance of the processed samples.

In the final stage, we organize and analyze the experimental results and data obtained and publish the results.

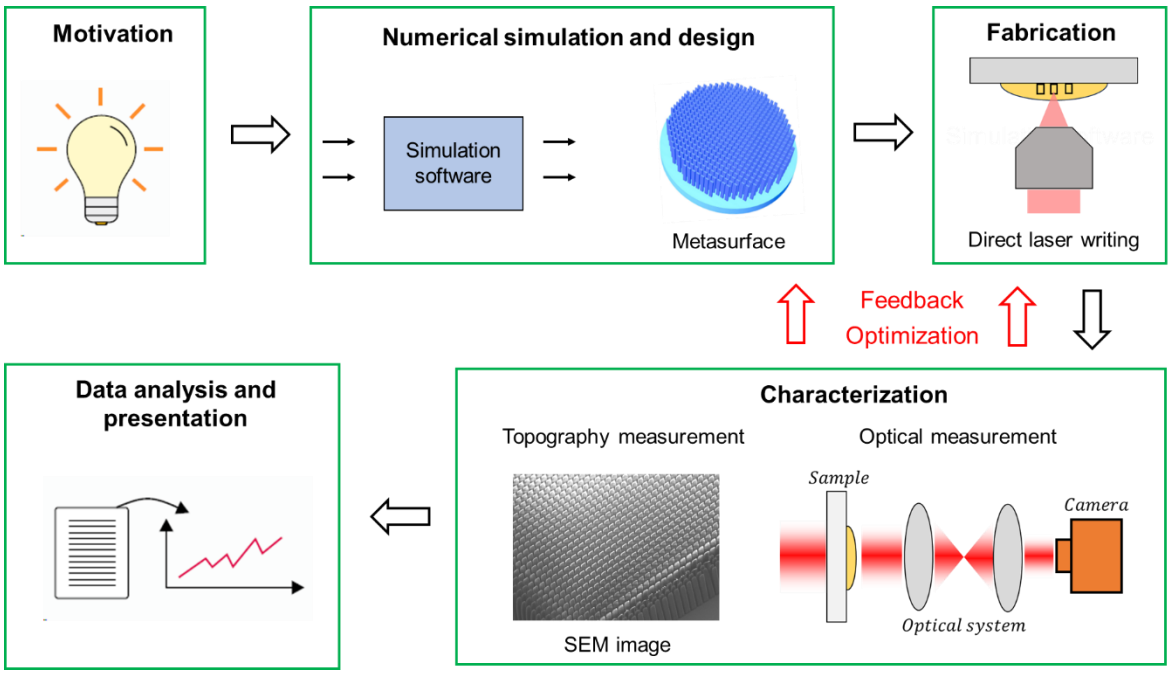


**Figure 3.1.: General workflow for research projects in this thesis.**

## 3.2 Fabrication

In this section, our focus will be on the manufacturing process of 3D meta-atoms using DLW. We will begin by outlining the general process flow of 3D printing. Subsequently, we will delve into more detailed experimental aspects, including the optimization of recipes and processing accuracy. Finally, we will discuss the process of assembling multiple structures and printing structures on the fiber end face.

### 3.2.1 General fabrication flow

The 3D metasurface processing in this dissertation mainly uses Nanoscribe Company's commercial laser direct writing equipment Nanoscribe GT. The general fabrication flow consists of the following three parts:

1) Clean the substrate to ensure that no dust and impurities will affect printing. Drop the photoresist onto the sample and load the sample into the system.

2) Find the substrate surface and start printing. Given the nanoscale nature of the structure, opt for a 63x objective lens for printing. Since the focal length of the objective lens is smaller than the thickness of the substrate, printing mode is set to dip-in mode. Utilize galvo mirrors for scanning in the XY plane and a piezo stage for scanning in the Z direction. The photoresist used in this paper is IP-L resin provided by Nanoscribe.

3) After the sample printing is completed, we use wet development to process the sample. Samples will be immersed in Propylene glycol methyl ether acetate (PGMEA), isopropanol (IPA) and Novc 7100 for 20, 5 and 2 minutes, respectively.

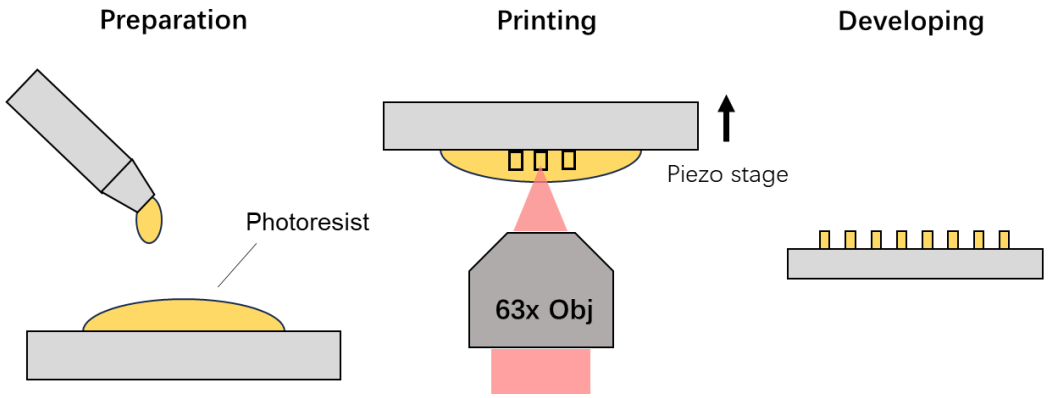


**Figure 3.2.: General process flow chart of laser direct writing manufacturing**

## 3.2.2 Recipe test

In laser direct writing processing, the exposure amount is undeniably the most crucial parameter, as it determines whether the photoresist can polymerize effectively. In the Nanoscribe GT system, exposure is primarily adjusted through two parameters: laser intensity and scanning speed. Therefore, prior to processing the metasurface, it is essential to conduct a recipe test to identify the most suitable processing parameters.

In the recipe test, we varied the laser power and scan rate separately. We selected a nanopillar metasurface array with dimensions of 1 µm in length, 600 nm in width, 6 µm in height, and a period of 1.5 µm as the test sample. For the laser energy scanning, the power was set to 60% to 80% of the laser's standard power. In the scan rate test, the scan rate ranged from 6000 to 14000µm/s. SEM images of the scanned samples were then captured to observe the morphology of the metasurface.

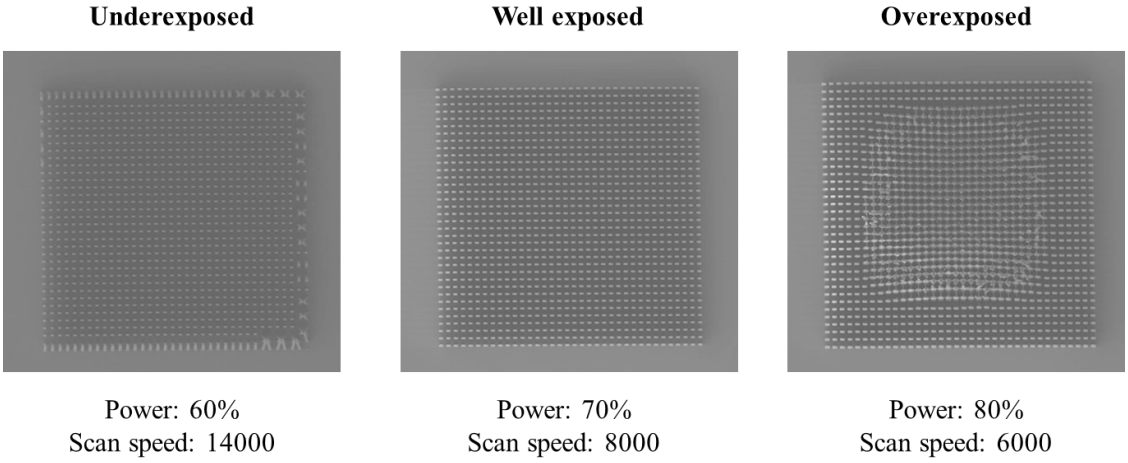


**Figure 3.3.: SEM images of nanopillars under different exposure levels**

Clearly, as the laser power increases (or as the scan speed decreases), the exposure also increases. As illustrated in Figure 3.3, when the laser power is set to 60% and the scanning rate is 14,000µm/s, the nanopillars at the edge collapse, indicating insufficient exposure and inadequate polymerization of the photoresist. Conversely, when the laser power is 70% and the

scanning speed is 8000μm/s, the resulting metasurface exhibits a desirable morphology, suggesting that the exposure amount is appropriate. However, when the laser power is increased to 80% and the scanning speed is reduced to 6000μm/s, overexposure is evident in the middle part of the metasurface.

### 3.2.3 Printing accuracy calibration

In photolithography, one unavoidable challenge is the diffraction limit, which imposes constraints on the achievable resolution. Although the Nanoscribe GT system, based on the two-photon absorption principle, can achieve a processing accuracy of 200 nm, such errors are unacceptable for submicron metasurface structures. Figure 3.4 illustrates the principle of error generated by DLW. As depicted, the actual processed structure tends to be larger than the designed structure. Consequently, when designing metasurfaces, it is essential to modify the size of the nanopillars to account for this inherent error.

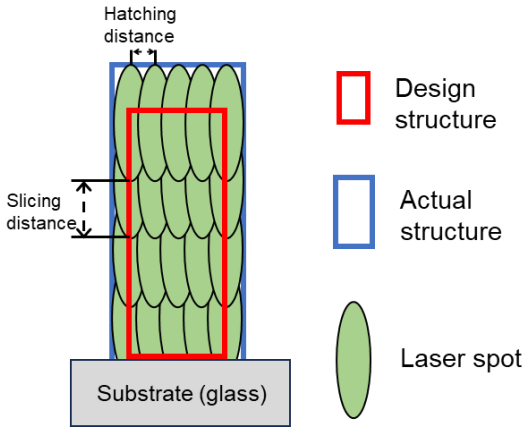


**Figure 3.4.: Schematic diagram of the 3D printing process**

Indeed, the discrepancy between the designed size and the processed size primarily arises from the finite volume of the light spot. As the area of TPP increases with exposure, adjustments to the processing parameters can impact the final dimensions of the fabricated structures. To achieve higher processing accuracy, it's crucial to stabilize the processing recipe before proceeding with dimensional calibration.

For the error analysis similar to the formulation test, we opted to assess the discrepancy between the designed size and the processed size by designing nanostructures of varying dimensions and measuring them using SEM. Given that the metasurface we employ is a three-dimensional structure, corrections must be applied across all three dimensions: $x$, $y$ and $z$.

**Lateral size calibration**

In lateral size calibration, the calibration was done for nanopillar length and width dimensions. In horizontal direction, we design different nanopillars with length changing from 600nm to 1200nm with a step of 100nm. We measured the length of pillars under SEM and obtained the relationship between the design and measured results by fitting (Figure 3.5).

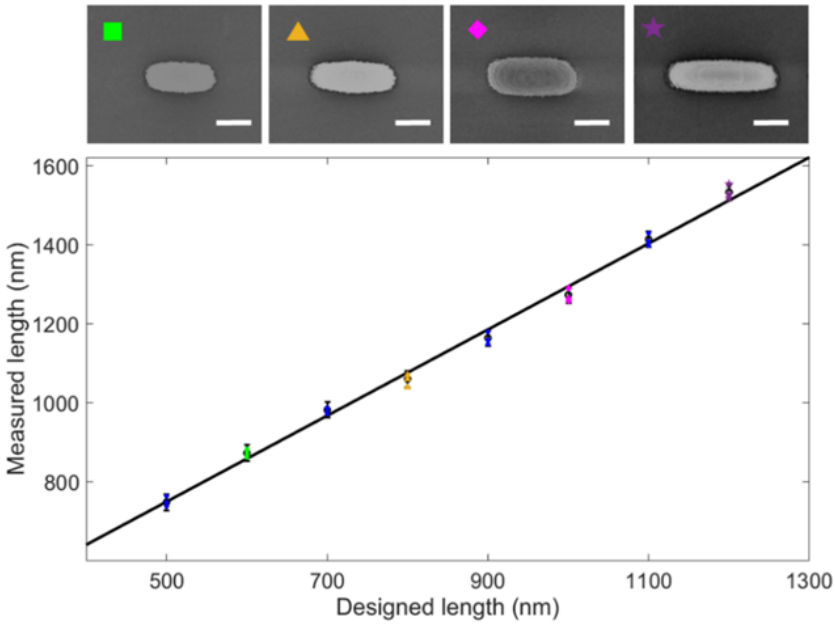


**Figure 3.5. Fitting relationship between design length and measured length.** The images on top are the SEM image for different length of pillars. (scale bar: 500nm) From left to right images are design lengths of 600nm, 800nm, 1000nm and 1200nm.

There is a linear relationship between the design and the actual printing size. So, the fitting relationship is written as:

$$W_{measured} = 1.03 * W_{designed} + 341.2$$

The same method is used for the width characterization and the experiment results are shown in Figure 3.6. Similarly, relationship between design and actual printed size can be written as:

$$W_{measured} = 1.03 * W_{designed} + 341.2$$

It should be noted that although we have reduced the error by compensating in the design, it can be obtained from the experimental results that there are still some errors, which can be reduced by further optimization.

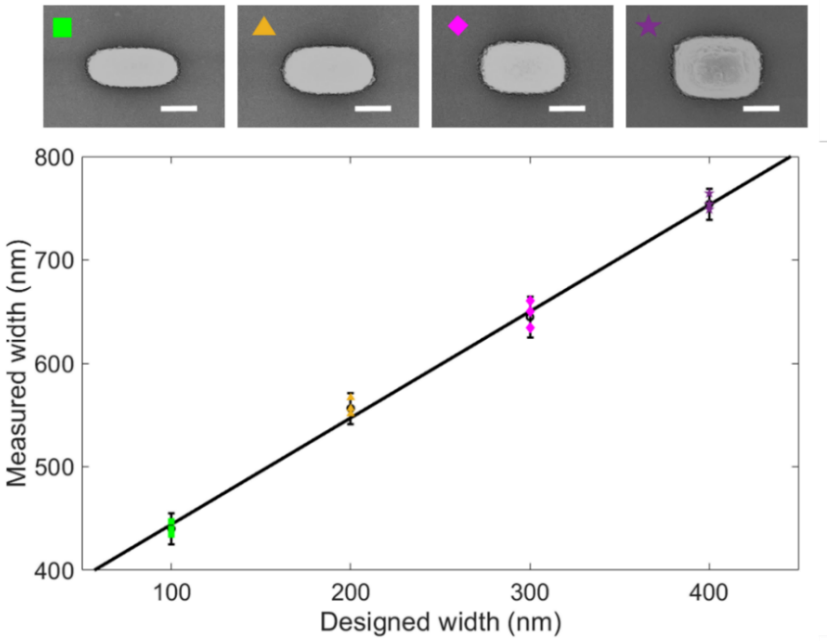


**Figure 3.6.: Fitting relationship between design width and measured width.** The images on top are the SEM image for different width of pillars. (scale bar: 500nm) From left to right images are design width of 100nm, 200nm, 300nm and 400nm.

**Axial calibration of nanopillar**

In the height calibration, we design different nanopillars with height from 6µm to 10µm with an increment of 1µm, which cover most heights of pillars used in our 3D design library. In order to make the measurement more accurate, we decided to push down the nanopillars instead of measuring height at a tilt angle of SEM imaging. It should be mentioned that the height resolution (smallest variation in height) is controlled by the slicing accuracy in the nanoprinting process, which was set to be 20nm in our experiment.

To provide a precise characterization, the actual procedure includes fabrication of nanopillars of different heights on a glass substrate, turning the sample upside down and placing it on a smooth platform, and slightly sliding the sample. This forces the nanopillars to be pushed down on the surface. (Figure 3.7)

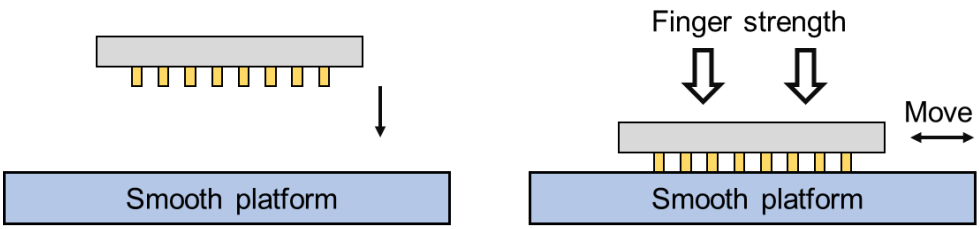


**Figure 3.7.: Process used to push down nanopillars.**

Undamaged pillars were measured under SEM and compared to the designed heights. Thus, we obtain a relationship between design and the actual height of the nanopillars. Selected SEM images of pulled down nanopillars and their corresponding heights are shown in Figure 3.8.

The relationship between designed height and measured height is linearly fitted with the following expression:

$$H_{measured} = H_{design} + 0.48\mu m$$

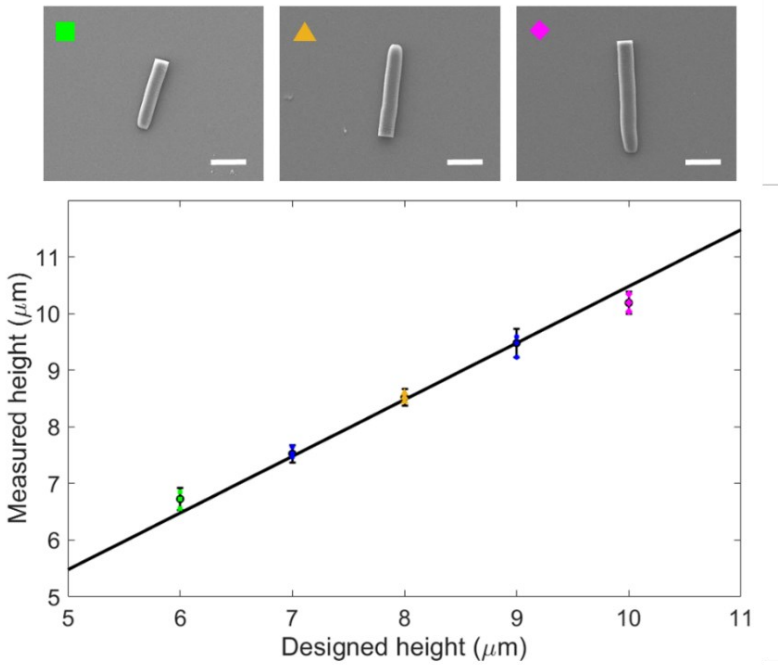


**Figure 3.8.: Fitting relationship between designed height and measured height.** Top images: SEM images of three selected heights of nanopillars with designed heights of 6 μm, 8 μm and 10 μm, respectively (scale bar: 3μm).

## 3.2.4 Multiple structure printing

In the preceding discourse, it has been established that the actual printed dimensions may exceed those of the intended structure. Consequently, when printing multiple structures, meticulous adjustment of the inter-structure spacing along Z direction becomes imperative to ensure precise printing, particularly in the case of 3D meta-atoms (since the height is related to the accumulated phase). In pursuit of this aim, we have devised a structure wherein nanopillars are supported by a circular buffer layer. By fine-tuning the spacing between structures, we guarantee congruence between the height of the nanopillars and the predetermined design specifications.

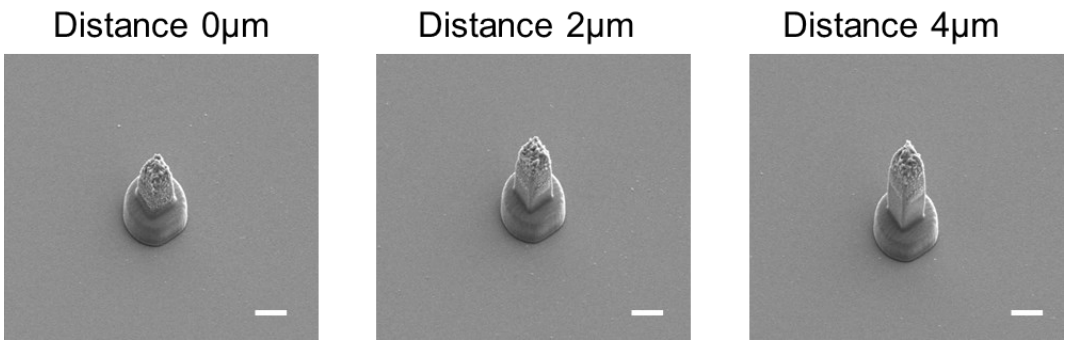


**Figure 3.9.: SEM images of multiple structures.** From left to right, the distance between the nanopillar and buffer layer is 0, 2, and 4μm, respectively. (scale bar: 5μm)

In the experiment, we designed a buffer layer of 2μm height and used Z-drive printing mode. The nanopillar, set at a height of 5μm, utilized the piezo stage printing mode. The spacing between buffer layer and the nanopillar was systematically varied from 0 to 4μm, with increments of 0.5μm. Figure 3.9 depicts an SEM image of the test sample, with a tilt angle of 45°. Evidently, the distance between the buffer layer and the nanopillar exerts a discernible influence on the actual height of the nanopillars. Notably, when the inter-layer distance is set at 2μm, the actual height of the nanopillars is consistent with the predetermined design height.

### 3.2.5 Fabrication flow on fiber

The procedural workflow for printing on fiber endfaces closely parallels that for glass substrates. However, due to the diminutive size of the fiber end face, typically spanning only a few hundred microns, precise fiber positioning assumes paramount importance. Figure 3.10 elucidates the comprehensive process of printing on the fiber end face, comprising four sequential steps:

1) Preparation: Commences with the removal of cladding from the fiber and subsequent precision cutting to ensure a clean and flat end face of the fiber. Then the processed fiber is loaded into a fiber connecter (B30126A9, Thorlabs) with a fiber terminator (BFT1, Thorlabs) for subsequent printing.

2) Location: Involves the insertion of the optical fiber into the Nanoscribe system, positioning it beneath an objective lens featuring a 20x magnification, and recording the precise coordinates.

3) Printing: Entails the deposition of photoresist onto the fiber end face, followed by transitioning to an objective lens boasting a 63x magnification to pinpoint the fiber's position and commence the printing process.

4) Developing: Entails subjecting the printed optical fiber to the development process, culminating in the acquisition of the final sample.

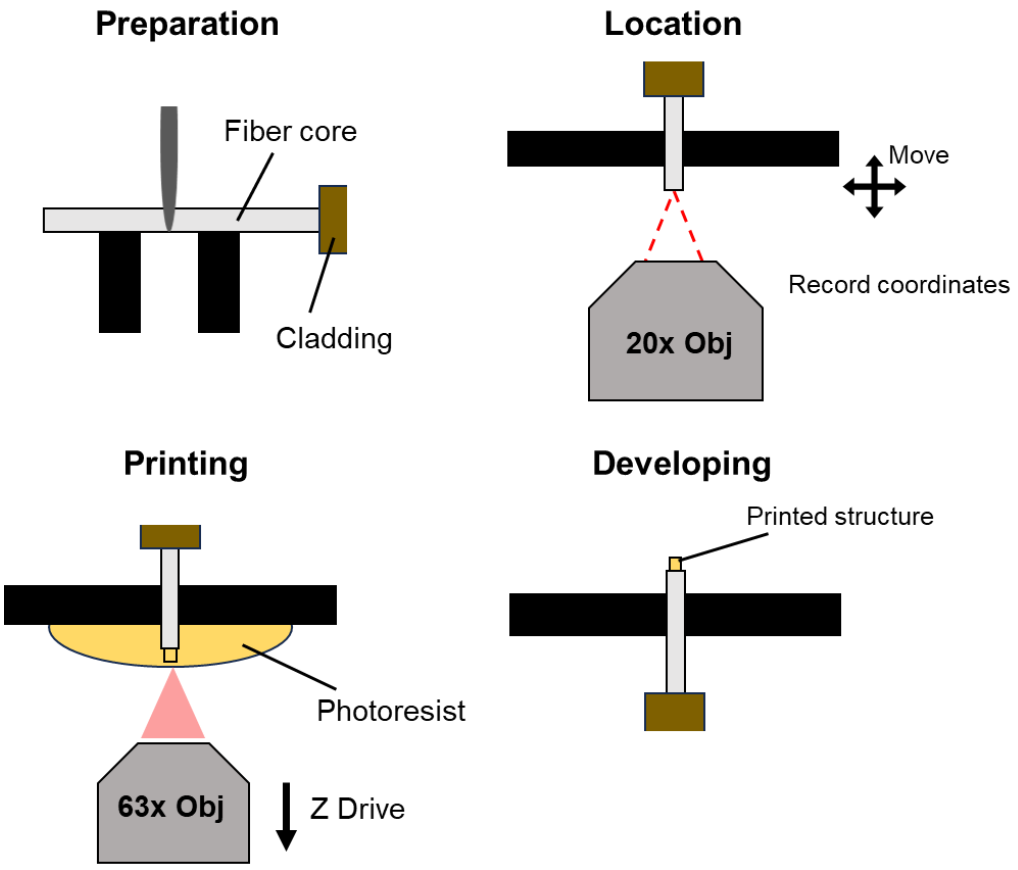


**Figure 3.10. : General process flow chart of laser direct writing manufacturing on a fiber.**

# 4. Dispersion control based on 3D metasurface.

*The results presented in this chapter are published in the scientific open-access journal Nature Communications (Haoran Ren, Jaehyuck Jang, **Chenhao Li**, (contribution equally) et al. Nature Communications 13, 4183 (2022), see ref.[93]). As a basis of the chapter, the peer-reviewed manuscript is used and complete sentences or even paragraphs will be taken word by word from the manuscript along with graphic content/figures since Springer Nature allows the reprinting of own contributions in theses, also in accordance with the terms of the CC-BY Creative Commons Attribution 4.0 International license http://creativecommons.org/licenses/by/4.0/.*

Optical fibers hold significant technological importance owing to their unique attributes, such as flexible handling, robust light confinement, and efficient light transportation over extensive distances, leading to a multitude of applications in modern optics, including fiber communications, optical trapping, nonlinear light generation, and endoscopic imaging. Notably, fiber imaging plays an important role in medical diagnostics due to its ability to scan and image internal tissues in living environments. However, conventional endoscopic imaging typically relies on bulky gradient index lenses or refractive ball lenses on the fiber end face to collect scattered and emitted light from objects. This approach may lead to pronounced chromatic aberration, adversely affecting imaging quality. In this context, we present an innovative solution to mitigate chromatic aberration by designing and nanoprinting a 3D achromatic diffractive metalens on the end face of a single-mode fiber. This metalens exhibits the ability for achromatic and polarization-insensitive focusing across the entire near-infrared telecommunication wavelength band, ranging from 1.25 to 1.65 μm.

## 4.1 Introduction

Optical dispersion is a natural phenomenon where the group velocity of a wave varies with its frequency. Since Sir Isaac Newton historically used a prism to decompose sunlight into different colors, dispersion has gained prominence and attracted the interest of researchers (Fig. 4.1 a). Natural materials typically exhibit positive dispersion, wherein the refractive index decreases with increasing wavelength. Figure 4.1b illustrates the relationship between the refractive index of commonly used optical materials and wavelength. It's evident that different materials exhibit varying refractive index changes in the visible light region. The rate of change of refractive index with wavelength is defined as the dispersion rate.

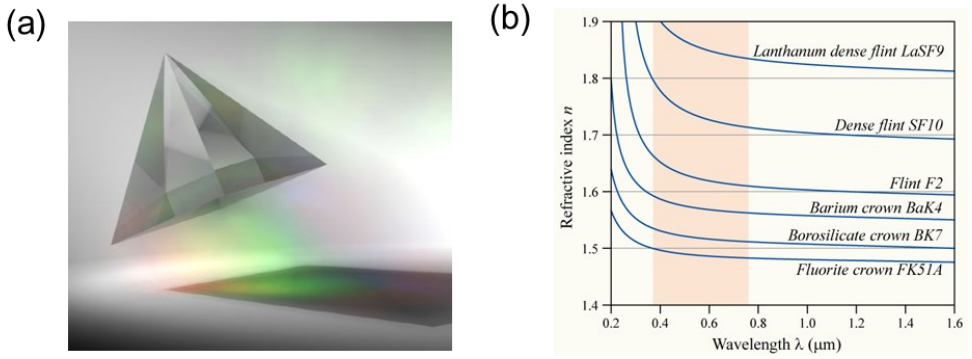


**Figure 4.1.: Dispersion phenomenon and dispersion rate of conventional glass material.** (a) Sunlight is split into polychromatic light by a prism. (b) The relationship between refractive index and wavelength for ordinary optical materials. Adapted under the terms of the Creative Commons Attribution-Share Alike 3.0 Unported. *https://commons.wikimedia.org/wiki/File:Dispersion-curve.png*

According to Snell's law, an ordinary glass lens would lead short-wavelength light has a shorter focus, as shown in Figure 4.2a. This unique dispersive nature of light has thus been widely used in spectrometer systems. However, dispersion can induce chromatic aberrations in optical lenses, severely affecting the performance of optical imaging systems. Dispersion engineering is crucial for achromatic focusing and imaging in optical microscopes [94], data storage [95], optical communications [96], display systems [97], as well as for shaping ultrafast pulses in nonlinear microscopy and laser surgery [98].

The conventional method for correcting chromatic aberrations is to introduce another material with a different dispersion rate to compensate dispersion. For example, a doublet lens composed of a flint glass concave lens and a crown glass convex lens can mitigate chromatic aberration, as depicted in Fig 4.2b. However, this achromatic method is constrained by material properties and cannot continuously compensate for dispersion across a broadband spectrum. On the other hand, this approach inevitably results in a thicker and bulkier optical lens system, posing a significant challenge for device miniaturization and photonic integration.

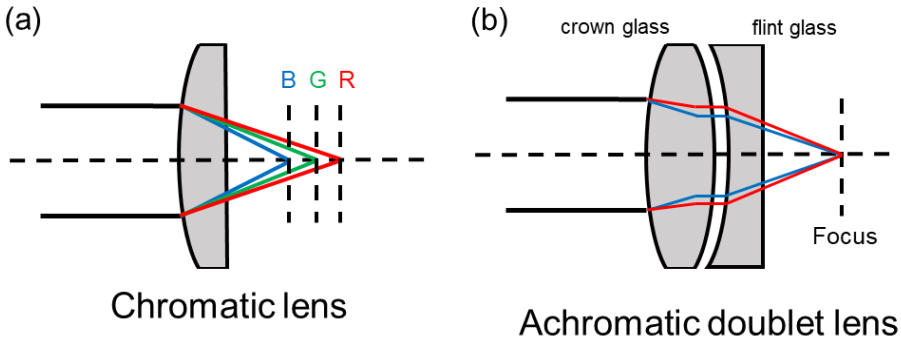


**Figure 4.2.: The schematic diagrams illustrating dispersion and chromatic aberration reduction in traditional optical lenses.** (a) Chromatic aberration of a single lens causes different wavelengths being focused to different planes. (b) An achromatic doublet in a bulky form converges different wavelengths to a common focal point.

In addressing the challenges in conventional optical systems, the emergence of metasurfaces has opened transformative avenues to optics-related fields. Metasurfaces have garnered considerable attention owing to their unparalleled capabilities for shaping light properties, encompassing phase, amplitude, and polarization. This control is achieved through the manipulation of subwavelength meta-atoms, where the shape, physical size, and orientation play pivotal roles in determining the optical behavior (the pixels of a metasurface). Due to their superior advantages in light manipulation, miniaturization, and compatibility, ultrathin metasurfaces have been widely developed to realize different optical components, such as holograms [99], wave plates [100], cloaks [101], vortex plates [102], thin absorbers [103], and sensors [104]. Among these optical components, metalenses offer outstanding performance in diffraction-limited light focusing and have the potential to replace conventional bulky refractive lenses.

As we mentioned in Chapter 2, wavefront control of metasurfaces comes from the phase mutation, so the dispersion of metasurfaces is completely different from the dispersion in traditional optics. According to Fermat's principle, for a refractive lens, the optical paths of different rays must be equal, that means the phase at the focal point should follow the relationship:

$$\varphi_{ml}(r,\omega) + \varphi_p(r,\omega) = 0, \qquad (4-1)$$

where $\varphi_{ml}(r,\omega)$ and $\varphi_p(r,\omega)$ are the phase profile imparted by metalens and propagation distance, respectively. Obviously, the propagation phase is related to the propagation distance $d_p$ and satisfies the following equation:

$$\varphi_p(r,\omega) = 2\pi\frac{d_p}{\lambda} = \frac{\omega}{c}d_p, \qquad (4-2)$$

Where $\lambda$ is the wavelength and $\omega$ represents the angular frequency of light. Bringing in geometric relationships, the phase profile analytical expression of metalens can be easily written:

$$\varphi_{ml}(r,\omega) = -\frac{\omega}{c}\left(\sqrt{r^2+F^2} - F\right), \qquad (4-3)$$

where $r$ and $F$ are the lens radial coordinate and focal length of metalens, respectively.

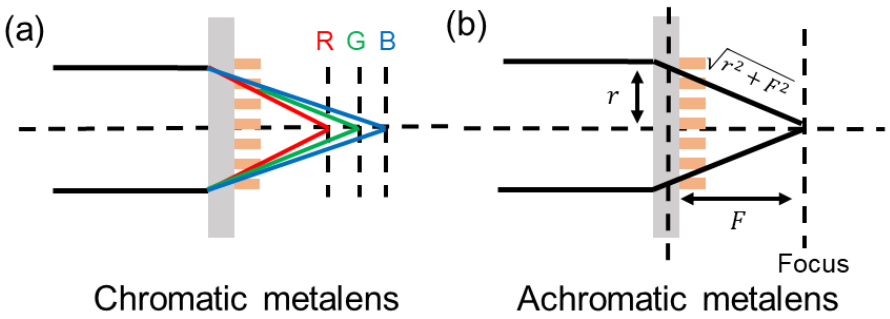


**Figure 4.3.: The schematic diagrams illustrating dispersion and chromatic aberration reduction in metalens.** (a) The chromatic aberration of the chromatic metalens causes different wavelengths to be focused into different planes. (b) Achromatic metalenses converge different wavelengths into a common focus.

Equation (4-3) represents the phase relationship that the metalens must satisfy. It's evident that the phase distribution in the equation is influenced by the angular frequency of light, leading to the dispersion of the metalens. However, for a metalens without achromatic function, same meta-atoms with different in-plane orientations (geometric phase type) or small size variations (propagation phase type) are typically used, leading to approximately the same phase profile at different angular frequencies. As a result, a larger (smaller) angular frequency incident on the metalens could lengthen (shorten) the focal length. This leads the metalens exhibit a negative dispersion property that are different from traditional lenses, that is, short-wavelength (high-frequency) light has a longer focus. Therefore, to reduce the chromatic aberration, the achromatic metalens has to impart a specific phase profile for each wavelength of the incident light to compensate for the phase difference caused by dispersion.

Since dispersion is related to frequency, phase profile equation can be Taylor expanded around a design frequency $\omega_d$, which is usually chosen at the center of the bandwidth of interest:

$$\varphi(r,\omega) = \varphi(r,\omega_d) + \left.\frac{\partial\varphi(r,\omega)}{\partial\omega}\right|_{\omega=\omega_d}(\omega-\omega_d) + \frac{1}{2}\left.\frac{\partial^2\varphi(r,\omega)}{\partial\omega^2}\right|_{\omega=\omega_d}(\omega-\omega_d)^2 + \cdots, \quad (4-4)$$

where $\varphi(r,\omega_d)$ represents the required phase at the center wavelength, and $\frac{\partial\varphi(r,\omega)}{\partial\omega}$ and $\frac{\partial^2\varphi(r,\omega)}{\partial\omega^2}$ denote the group delay and group delay dispersion, respectively. Since the phase of the achromatic metalens is leaner to the angular frequency $\omega$ (as shown in equation (4-3)), the second-order and higher-order terms in equation (4-4) are zero. By deriving equation (4-4) with respect to the angular frequency ω of light, the expression for the group delay can be obtained:

$$\frac{\partial\varphi(r,\omega)}{\partial\omega} = -\frac{\sqrt{r^2+F^2}-F}{c} \quad (4-5)$$

the group delay which can be also seen as the slope between phase and the angular frequency.

To gain a more intuitive understanding of the achromatic principle of the metalens, consider Figure 4.4, where incident polychromatic light is envisioned as individual wave packets. The requisite phase guides each wave packet toward the focus, while the group delay serves as a temporal adjustment compensating for variations in optical path lengths. This ensures that wave packets of differing frequencies originating from distinct radial coordinates converge at the focus simultaneously. Consequently, the phase and group delay generated by the achromatic metalens must concurrently adhere to equations (4-3) and (4-5).

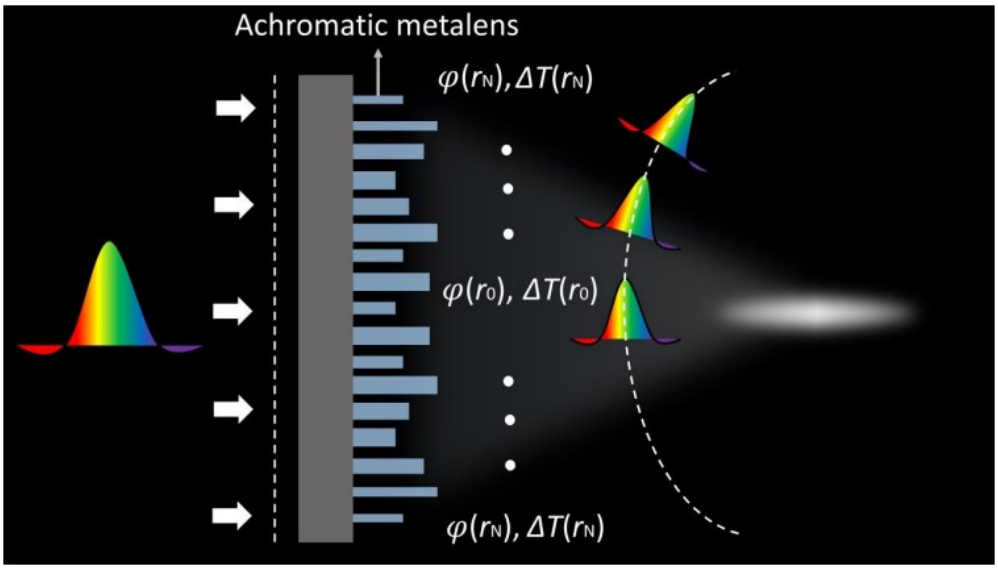


**Figure 4.4.: Principle of an ultrathin diffractive achromatic metalens.** To realize achromatic focusing, the radially (r) arranged phase profile of $\varphi(r)$ creates a spherical wavefront for focusing, while the group delay profile of $\Delta T(r)$ compensates the difference in arrival times at the focus for broadband light.

## 4.2 Theory

In Chapter 2, we already proved that 3D meta-atoms can adjust the phase. Now, we aim to theoretically demonstrate that meta-atoms possess the capability to adjust the group delay.

For a 3D nanopillar, the phase can be described by:

$$\varphi(\omega, H) = \frac{\omega}{c} n(\omega) H \qquad (4-6)$$

Where $\omega$is the angular frequency of light, $c$ is the speed of light, $n(\omega)$ is the effective refractive index corresponding to the $\omega$, and $H$ is the height of the nanopillar. As we analyzed earlier, the group delay is the first derivative of the phase with respect to angular frequency $\omega$; thus, the group delay of the 3D nanopillar can be written as

$$\frac{\partial \varphi(\omega_d, H)}{\partial \omega} = \frac{1}{c}\left(n(\omega_d) + \omega_d \frac{\partial n(\omega)}{\partial \omega}\right) H \qquad (4-7)$$

where $\omega_d$ is the nominal frequency at which the achromatic metalens is designed. Apparently, according to equation (4-7), the group delay is contingent upon the effective refractive index of the metasurface and the height of the 3D nanopillar. Considering that the photoresist utilized in 3D nanoprinting is typically a polymer, its refractive index can be regarded as constant in the near-infrared region. As discussed in Chapter 2, the effective refractive index is primarily determined by the lateral dimensions of the nanopillar. Therefore, the group delay can be tuned by finely controlling the size of the nanopillars. In addition, the group delay of nanopillars is linearly related to the height of the nanopillar, which means that the high degree of freedom can significantly expand the group delay response, which has great potential to provide better performance of achromatic metalens.

Group delay can be conceptualized as the temporal delay experienced by the signal envelope within the time domain. To gain deeper insight into this phenomenon, it is valuable to scrutinize group delay from a temporal perspective. Essentially, group delay represents the time difference during the propagation of light of different frequencies.

For the light propagation in a waveguide with restricted transverse extension, the phase constant of the waveguide equals the wavenumber in the vacuum $k_0$ times the effective refractive index $n_{eff}$: $k = k_0 n_{eff} = n_{eff}\frac{\omega}{c}$. The nanopillar waveguide can be regarded as a dielectric lossless slow-light device with a group velocity $v_g$ can be derived as:

$$v_g = \frac{\partial \omega}{\partial k} = \frac{c}{n_{eff} + \omega \frac{dn_{eff}}{d\omega}} \qquad (4-8)$$

The group index $S(\omega)$ can be defined as:

$$S(\omega) = \frac{\mathrm{c}}{v_g} = n_{eff} + \omega \frac{dn_{eff}}{d\omega} \qquad (4-9)$$

For a polymer nanopillar waveguide used in the spectral range of our interest, the dispersion of the effective refractive index is linear to the frequency as shown in Figure 4.5, thus:

$$\frac{dn_{eff}}{d\omega} = \frac{n_{max} - n_{min}}{\omega_{max} - \omega_{min}} \qquad (4-10)$$

Where $n_{min}$ and $n_{max}$ are the minimum and maximum effective refractive indices of the waveguide across the frequency range from $\omega_{min}$ to $\omega_{max}$.

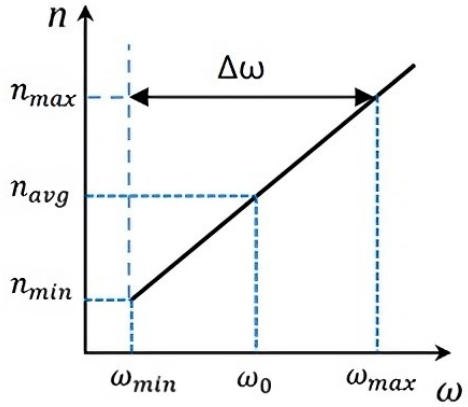


**Figure 4.5.: The relationship between effective refractive index and angular frequency**

Therefore, the group index at a designed frequency $\omega_{\mathrm{d}}$ can be rewritten as:

$$S(\omega_{\mathrm{d}}) = n_{eff} + \omega_{\mathrm{d}} \frac{n_{max} - n_{min}}{\Delta\omega} \qquad (4-11)$$

Where $\Delta\omega$ is the difference between $\omega_{min}$ and $\omega_{max}$.Therefore, the group velocity of the ideal device can therefore be calculated as:

$$v_g = \frac{\mathrm{c}}{S(\omega_{\mathrm{d}})} = \frac{\mathrm{c}}{n_{eff} + \omega_{\mathrm{d}} \frac{n_{max} - n_{min}}{\Delta\omega}} \qquad (4-12)$$

The time delay of the waveguide medium $T$ with height $H$ can be derived as:

$$T = H\left(\frac{1}{v_g} - \frac{1}{c}\right) = H\left(\frac{n_{eff}(\omega_d) - 1}{c} + \frac{\omega_d(n_{max} - n_{min})}{c\Delta\omega}\right) \qquad (4-13)$$

Here, a parameter called time-bandwidth product (TBP) $\kappa$ is introduced to describe quantify the extent of dispersion. It is defined as the product of time and bandwidth [105]:

$$T\Delta\omega = H\left[\frac{n_{eff}(\omega_d) - 1}{c}(\omega_{max} - \omega_{min}) + \frac{(n_{max} - n_{min})}{c}\omega_d\right] \qquad (4-14)$$

In general, the frequency bandwidth of a slow-light waveguide is much smaller than the central frequency: $\omega_{max} - \omega_{min} \leq \omega_d$. Equation (4-14) can be further reduced to:

$$T\Delta\omega = \frac{\omega_d}{c}\mathrm{H}(n_{max} - n_{min}) \qquad (4-15)$$

The upper bound of the TBP imposes a fundamental bandwidth limit on an achromatic metalens, which is generally written as $\kappa \geq T\Delta\omega$, where $\kappa$ is a dimensionless quantity.

For 3D nanopillar meta-atoms, the maximal phase delay is achieved when both the effective refractive index (controlled by the transverse size of a nanopillar waveguide) and the height of a meta-atom are maximal. On the other hand, the minimal phase delay is

obtained when both quantities are minimal. Hence, the upper bound of TBP $\kappa$ of a 3D metalens can be formulated as:

$$\kappa = \frac{\omega_d}{c}(\mathrm{H}_{max} n_{max}) - \frac{\omega_d}{c}[\mathrm{H}_{min} n_{min} + (\mathrm{H}_{max} - \mathrm{H}_{min}) n_b] \qquad (4-16)$$

where $\mathrm{H}_{max}$ and $\mathrm{H}_{min}$ are the maximum and minimum height of 3D meta-atoms, respectively, where $n_b$ is the refractive index of the surrounding background hosting meta-atoms. The unleashed degree of freedom in height could thereby largely extend the upper bound of the TBP as compared to the counterparts of 2D achromatic.

## 4.3 Design and simulation.

**Achromatic metalens design**

In the preceding section, we introduced the principle of dispersion and how metalens reduce the dispersion, emphasizing that both phase and group delay should adhere to equations (4-3) and (4-5) respectively. With the aim of attaining high-quality achromatic imaging, we formulated the design parameters for the metalens: a diameter of 100μm, a focal length of 225μm, and an operating wavelength band encompassing the telecommunications range. Figure 4.6 shows the phase and group delay distribution that the achromatic metalens should meet.

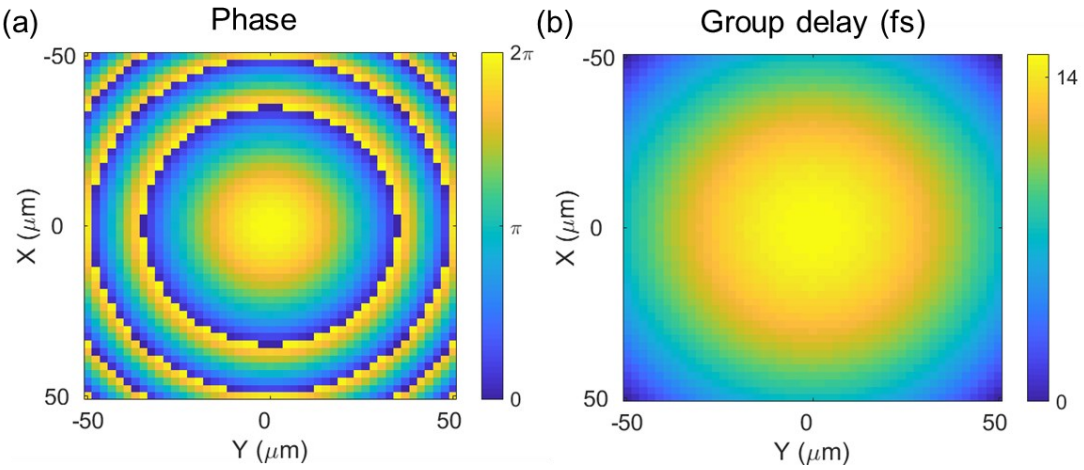


**Figure 4.6.: Phase (a) and group delay (b) distribution of the designed achromatic metalens.**

Our primary objective is to achieve corrected chromatic aberration imaging utilizing an optical fiber, necessitating consideration of the divergence of light emitted from the fiber end face. For our experiment, we opted for commercial single-mode fibers (SMF) with a numerical aperture (NA) of 0.1 from Thorlabs. To facilitate effective wavefront manipulation of the SMF output beam, we devised and fabricated a hollow tower structure on the end face of the SMF, thereby expanding its output into free space. Subsequently, we affixed the achromatic metalens atop this structure. In order to ensure that the broadband light output from the SMF can completely cover the metasurface, the height of the hollow tower structure is designed to be 525um (the mode field diameter increases from approximately 9.5 μm to 100 μm).

For the design of the achromatic optical metafiber, predicated on the spherical lens profile at the nominal wavelength of 1650 nm, the requisite phase and group delay for achieving the achromatic metalens were theoretically determined. Figure 4.7 (a) and (b) shows the phase and group delay exhibited by achromatic metafiber after taking into account the divergence of the fiber exit light, respectively. The final numerical aperture (NA) of the achromatic optical fiber was established at 0.12 and the achromatic metalens should have a group delay of 14fs.

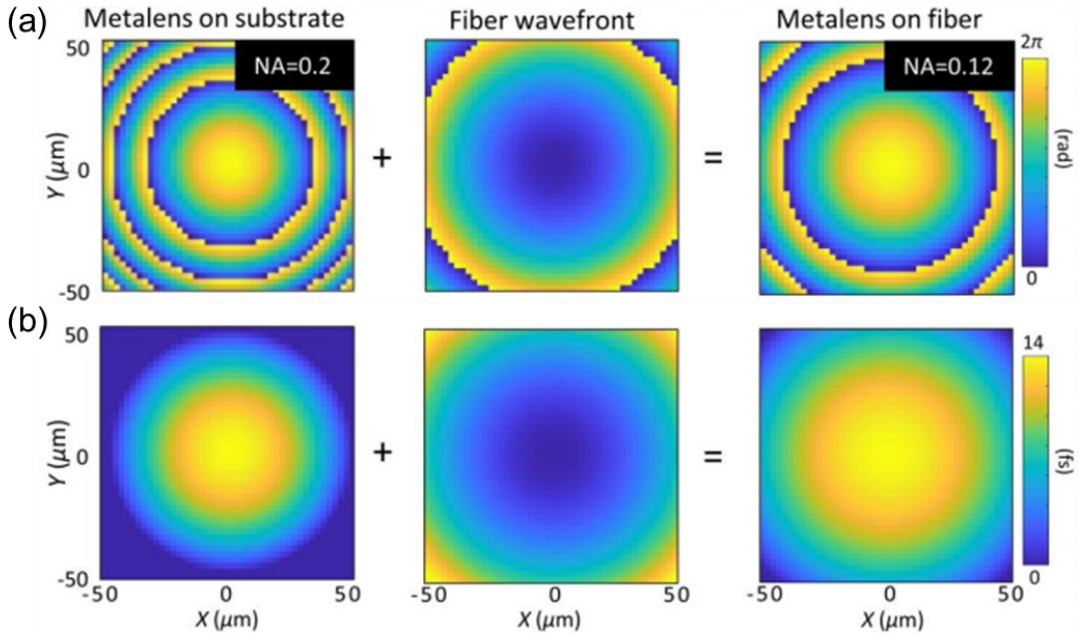


**Figure 4.7.: Theoretical design of an achromatic metalens.** (a) Phase and (b) group delay profiles of a spherical lens and a SMF output beam (at a distance of 525 μm) for the design of an achromatic metalens on a substrate and on a fiber end face, respectively. The designed was made at the maximal wavelength (1650 nm) within the working bandwidth.

**Simulation**

After obtaining the phase and group delay distributions of the achromatic metalens, we use nanopillars as shown in Figure 4.8 to achieve the required parameters for the metasurface. Due to the randomness of the polarization state of the SMF exit light, the rotation angle of the nanocolumn is set to 0 and 90° to ensure that the metasurface is not sensitive to polarization. A design library that contains phase and group delay in the cross-polarization response of 3D polymer nanopillars was constructed based on our in-house rigorous coupled-wave analysis model.

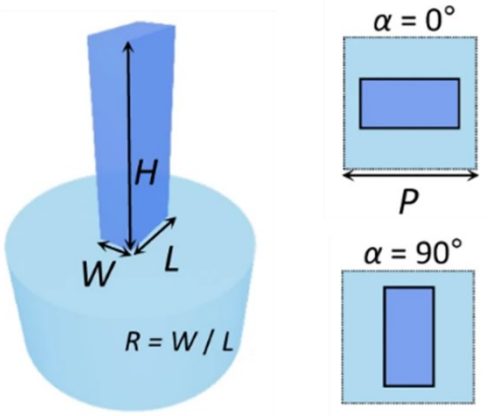


**Figure 4.8.: Schematic illustration of a nanopillar waveguide.**

In our simulation, we modeled 3D nanopillars composed of IP-L 780 polymer (Nanoscribe GmbH, Germany), featuring consistent parameters: a period (P) of 2.2 μm, length (L) ranging from 0.85 to 1.7 μm, height (H) spanning 8.5 to 13.5 μm, and an in-plane aspect ratio (R) varying between 0.3 and 0.6. As demonstrated in our previous chapter, TE and TM modes exhibit distinct effective refractive indices, and alterations in nanopillar height yield disparate group delays.

Figure 4.9 illustrates the effective refractive index and group delay responses of nanopillars with diverse lengths, widths, and heights. Notably, nanopillars with heights significantly exceeding the wavelength exhibit markedly expanded group delay and TBP, as projected by equation (4-12). Additionally, the subwavelength dimensions of 3D nanopillars induce a pronounced birefringent response, enabling the imprinting of a hyperbolic lens profile at a fixed wavelength.

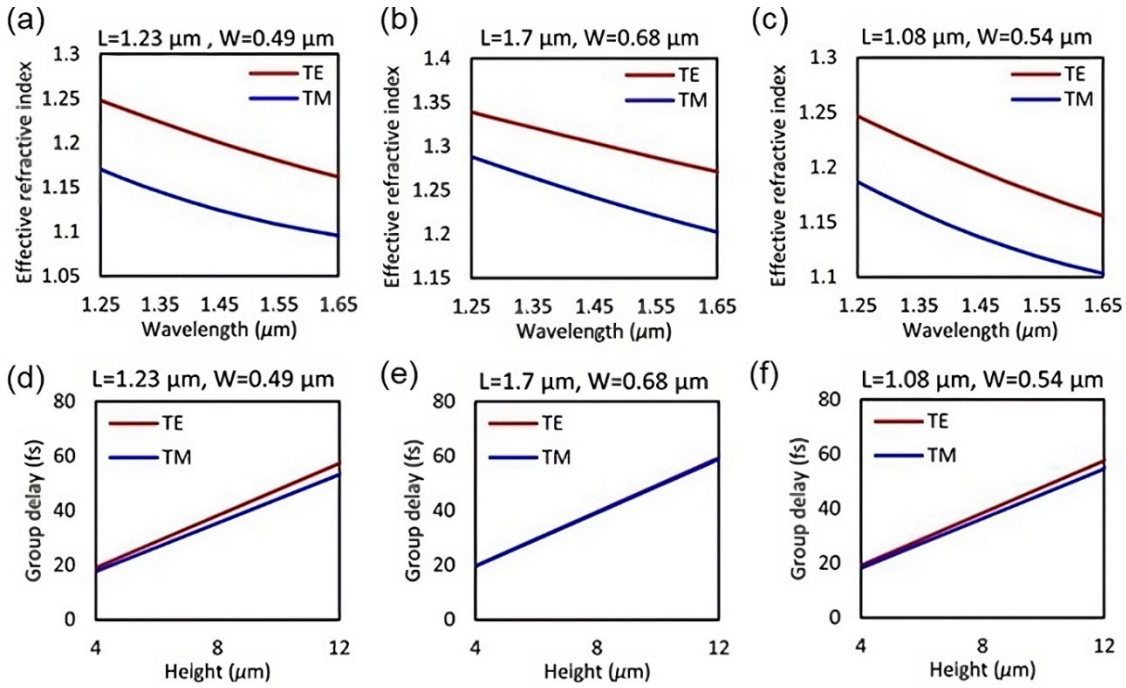


**Figure 4.9.: Effective refractive indices and group delay responses of 3D nanopillar meta-atoms.** (a-c) Effective refractive indices of the transverse electric (TE) and transverse magnetic (TM) modes as a function of wavelength for nanopillar with transverse dimensions of L = 1.23 µm, W = 0.49 µm (a); L = 1.7 µm, W = 0.68 µm (b); and L = 1.08 µm, W = 0.54 µm (c), respectively. (d-f) Group delay responses of the nanopillars in (a-c).

The resulting dataset is visualized in phase and group delay space, depicted by blue and red points in Figure 4.10. Each point corresponds to the simulation outcome of a distinct 3D nanopillar characterized by a unique combination of geometric parameters, including height and lateral dimensions. According to the principle of the Pancharatnam-Berry phase, a geometric phase is imparted to cross-polarized light that is scattered from a birefringent nanopillar by twice the amount of the in-plane rotation angle (α). Hence, the π-phase difference between the nanopillars rotated at 0 and 90 degrees enables us to fill most of the phase and modified group delay space (gray dots in Figure 4.9, each dot refers to a phase and group delay pair that is required in an achromatic lens design), in contrast being difficult to achieve for meta-atoms that are based on either resonant or propagation phase responses. To explicitly show that our 3D meta-atom library can fulfill the design of an achromatic metalens with NA = 0.2, we compared the theoretical requirements with the phase and modified group delay distributions provided by the library, as illustrated in Figure 4.11, both of which exhibit a good consistency.

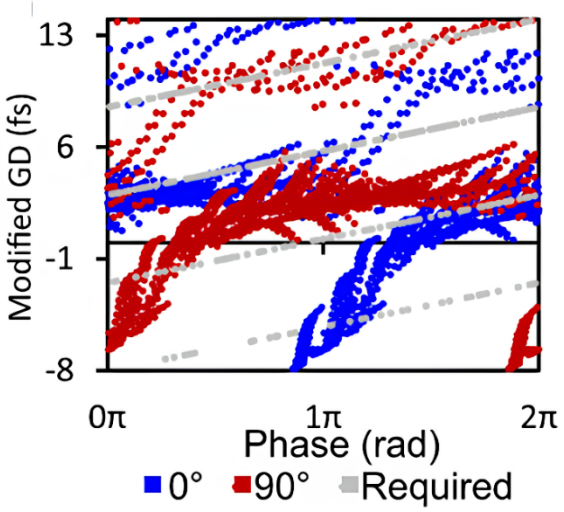


**Figure 4.10.: The designed phase and group delay library.** Gray dots: required pairs by an achromatic lens design; blue dots: simulated pairs based on the nanopillars with an orientation of 0 degree; red dots: simulated pairs based on the nanopillars with an orientation of 90 degrees.

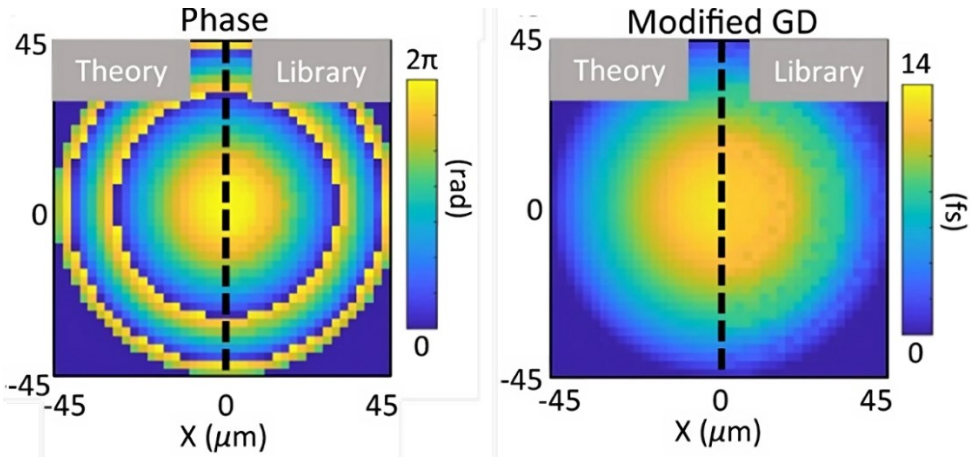


**Figure 4.11.: Theoretical and numerical design of the phase and group delay responses of an achromatic metalens.**

## 4.4 Experiments and characterization

### Characterization of a 3D achromatic metalens on planar substrate

To experimentally demonstrate achromatic light focusing, we commenced by fabricating the designed 3D achromatic metalens, featuring a clear aperture size of 100 μm, using 3D laser nanoprinting technology onto a silica substrate. (See fabrication method details in Chapter 3) Remarkably, we achieved high aspect ratio nanopillars, with the maximal ratio between height and transverse dimension reaching up to 27. These nanopillars exhibit varied heights spanning from 8.5 to 13.5 μm, as evidenced by the side-view scanning electron microscope (SEM) image depicted in Fig. 4.12.

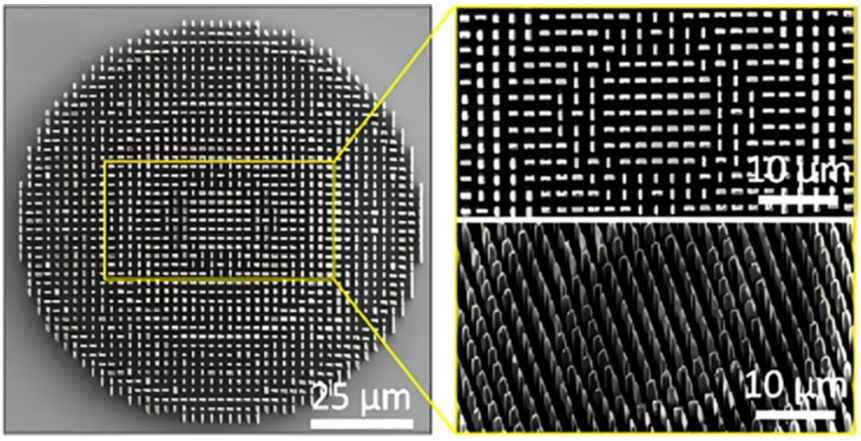


**Figure 4.12.: SEM images of the achromatic metalens.** Right: the top view and title view enlarged images

To characterize the achromatic metalens, we employed the optical setup depicted in Figure 4.13. The printed achromatic metalens is positioned on the movable nanoplatform of the piezo stage. A tunable laser beam, generated by a supercontinuum laser source (SUPERK FIANIUM, NKT Photonics) and controlled by an infrared wavelength selector (SUPERK SELECT, NKT Photonics), is directed onto the fabricated metalens. Notably, the metalens, affixed to a planar substrate, is illuminated by a collimated beam devoid of a divergent wavefront. Subsequently, the signal is captured through a microscope featuring a magnification of 10x and recorded using a near-infrared camera. This setup enables precise characterization of the achromatic metalens and assessment of its performance in focusing light across different wavelengths.

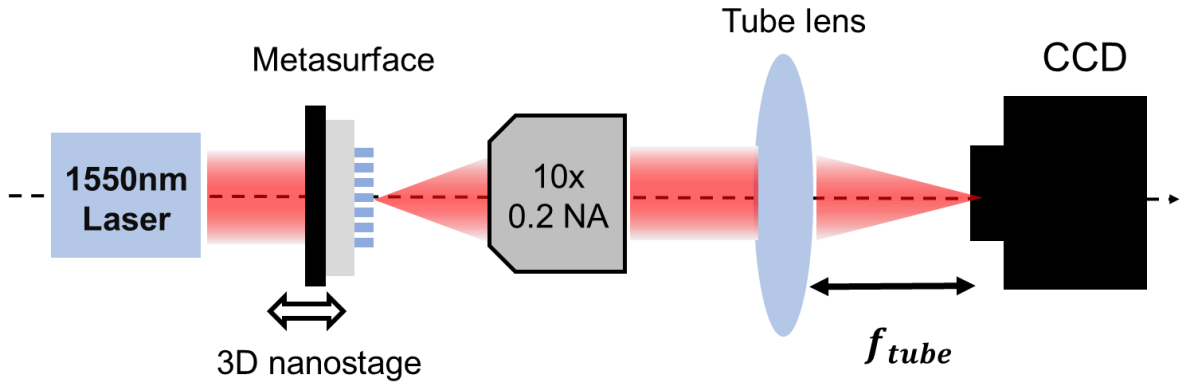


**Figure 4.13.: Optical setup diagram for measuring achromatic lens focusing.**

Through adjustment of the piezo stage, we systematically shift the achromatic metalens and measure the signal in the axial direction. Figure 4.14 illustrates that the measured axial focus position of the achromatic metalens remains consistent across different wavelengths, thus confirming the achromatic nature of our printed metalens. Consequently, an achromatic metalens fabricated on a planar substrate, with a numerical aperture (NA) of 0.2, achieves an achromatic and polarization-insensitive focus across the entirety of the telecommunications wavelength range. This validation underscores the efficacy of our design approach in realizing broadband achromatic focusing capabilities.

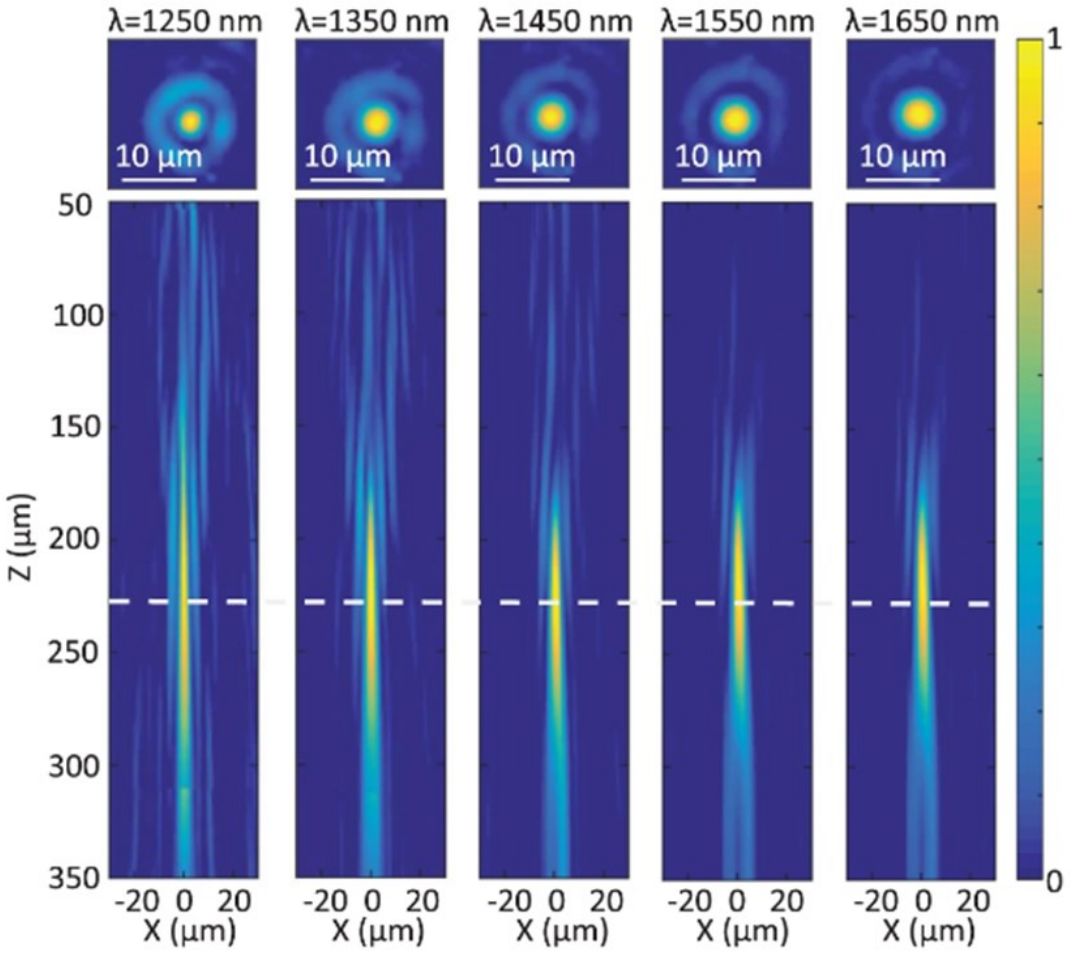


**Figure 4.14.: Experimentally characterized point-spread functions of the achromatic metalens in both transverse (top) and longitudinal (bottom) planes.**

We conducted experimental characterization of the efficiency, defined as the product of transmission efficiency and focusing efficiency, of the 3D nanoprinted achromatic metalens. Here, transmission efficiency refers to the ratio of light energy before and after it passes through the metasurface. Focusing efficiency, on the other hand, measures how much light is concentrated at the focal point. It is defined as the ratio of the energy at the focal point to the energy of the light emerging from the metasurface. For incident wavelengths spanning 1250 to 1650 nm, the efficiency values are as follows: 14.13%, 18.11%, 24.58%, 30.87%, and 32.01% for 1250, 1350, 1450, 1550, and 1650 nm, respectively (refer to Figure 4.15).

It is noteworthy to mention that our meta-atoms underwent numerical optimization, resulting in strong polarization conversion efficiency, particularly at the nominal wavelength of 1650 nm for the metalens design. (Since our meta-atoms are anisotropic, the polarization state of light changes as it passes through them i.e. the polarization conversion efficiency affects the efficiency of the metasurface.) Consequently, they exhibit higher conversion efficiency at this wavelength compared to others. As a consequence, the efficiency of the metalens is frequency-dependent and diminishes with increasing frequency.

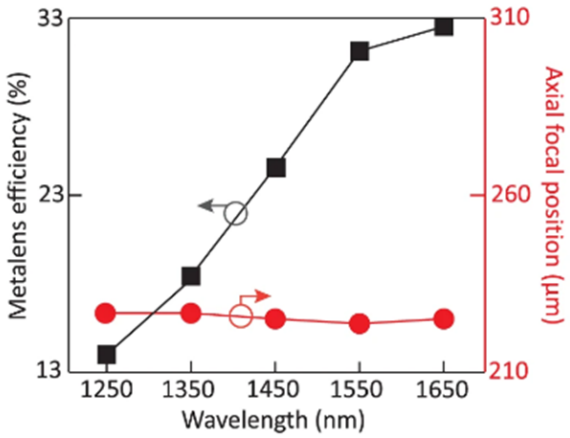


**Figure 4.15.: Experimentally characterized metalens efficiency and axial focal positions of the achromatic metalens on planar substrate at different wavelengths.**

The experimentally determined size of the achromatic focal spot consistently aligns with the diffraction-limited focus, as evidenced by a full width at half maximum (FWHM) of 3.03 μm (3.05 μm for the diffraction-limited case) for an incident wavelength of 1.25 μm. Similarly, for incident wavelengths of 1.35, 1.45, 1.55, and 1.65 μm, the FWHM values are 3.83 (3.52), 3.79 (3.82), 3.84 (4.01), and 4.24 (4.32) μm, respectively.

It's worth noting that the amplitude of the output light is strongly correlated with the height of the nanopillar. Consequently, the processed achromatic metalens may exhibit uneven amplitude due to limitations in processing accuracy. However, simulation calculations indicate that, compared to the scenario of uniform amplitude, non-uniform amplitude does not diminish the diffraction-limited focus. It yields identical half-maximum width, similar focal length, and marginally higher focusing efficiency owing to complex amplitude modulation. Therefore, the slight deviation observed in the measured FWHM values from the diffraction-limited values may stem from factors such as undersampling of the lens profile, rather than amplitude modulation alone.

In contrast, for comparison purposes, we conducted a control experiment involving the printing of a colored metalens with identical size and lens profile, but without group delay compensation (refer to Fig. 4.16). Notably, the focal position in this control scenario is significantly affected by strong dispersion, resulting in axial movement of the focal position in response to changes in incident wavelength. Specifically, as the incident wavelength transitions from 1.65 μm to 1.25 μm, the focus position shifts from 225 μm to 306 μm.

It's worth noting that for both achromatic and chromatic metalenses, a slight deviation in the focus position (f = 225 μm) is observed at a wavelength of 1.65 μm compared to the nominal design (f = 250 μm). This discrepancy arises due to spatial sampling of phase distributions and underscores the importance of careful consideration of such factors in experimental design and interpretation.

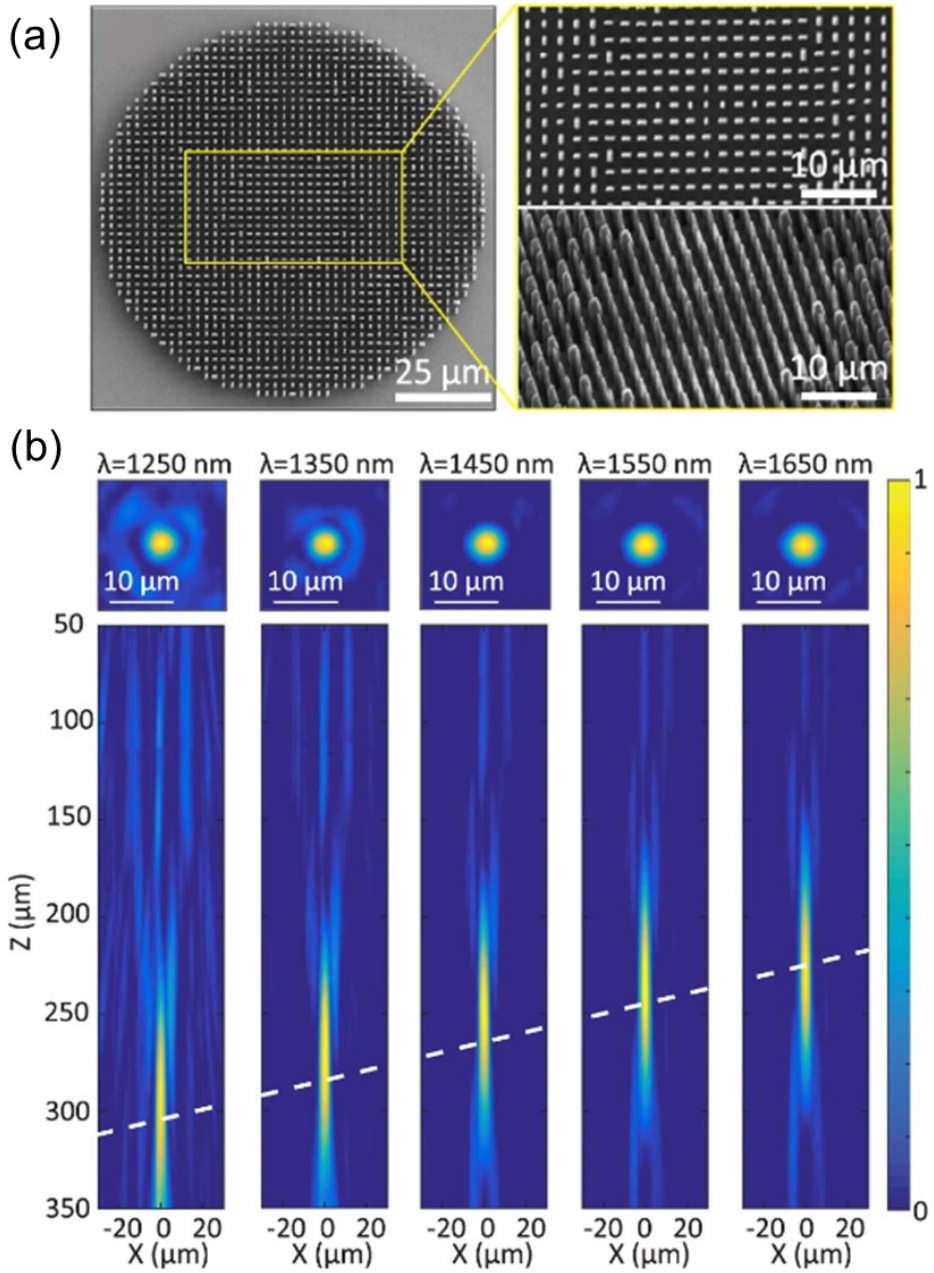


**Figure 4.16. The SEM image (a) and experimentally characterization of focusing (b) for chromatic metalens on glass. Dashed line: the position of focus at different wavelengths**.

**Characterization of an achromatic metafiber**

To demonstrate an achromatic metafiber based on this principle, we procedurally connected an achromatic metalens with a SMF and evaluated the focusing performance of the metafiber. For detailed processing methods of super optical fibers, please refer to Chapter 3. To augment the mode field diameter of the SMF output and facilitate efficient wavefront manipulation within the fiber, we fabricated a hollow tower structure on the cleaved SMF. This structure features a height of 525 μm, a diameter of 120 μm, and a sidewall thickness of 10 μm.

The diameter of the hollow tower is deliberately designed to be slightly larger than the mode field diameter of the fiber output at the metalens position, ensuring that the fiber bundle does

not contact the sidewalls of the tower. Close-up SEM images confirm the successful fabrication of the designed 3D achromatic metalens atop the fiber tower (refer to Figure 4.17).

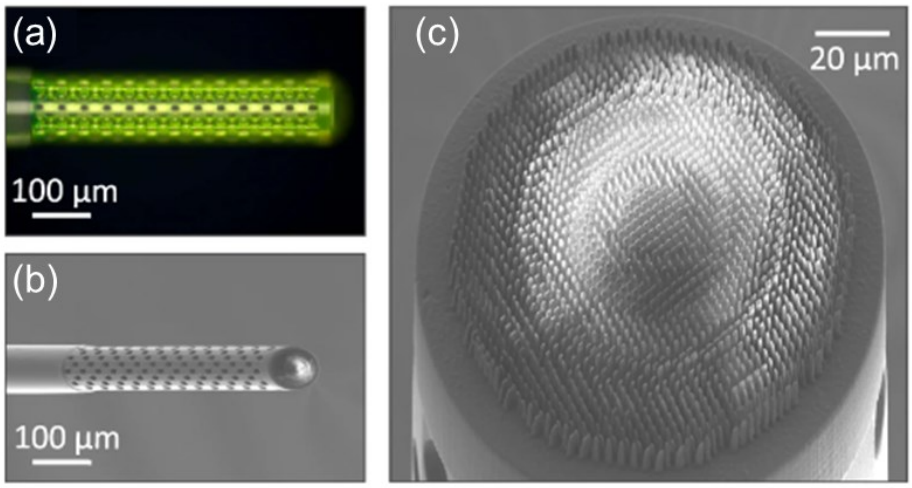


**Figure 4.17.: Optical (a) and SEM (b, c) images of the achromatic metafiber.**

The optical characterization methods employed for the metafiber are consistent with those used for flat substrate sample characterization. Experimentally obtained axial profiles of the metafiber foci at five different wavelengths (1.25, 1.35, 1.45, 1.55, and 1.65 µm) demonstrate the achromatic nature of the metafiber focus, with focal positions remaining nearly constant across the entire bandwidth of interest. Additionally, the metafiber exhibits an effective numerical aperture (NA) of 0.12.

Additionally, we further investigated the focal lateral size of the achromatic metalens, which determines its imaging resolution. The experimentally obtained full width at half maximum (FWHM) values of the achromatic metafiber focus were 4.97 µm (compared to 5.41 µm for the diffraction-limited case in our simulation), 5.45 µm (5.83 µm), 5.81 µm (6.23 µm), 6.27 µm (6.63 µm), and 6.74 µm (7.13 µm) for incident wavelengths of 1.25, 1.35, 1.45, 1.55, and 1.65 µm, respectively. The slightly smaller FWHMs observed in our measured results compared to the diffraction-limited case may be attributed to a slight over-compensation of the divergent fiber wavefront.

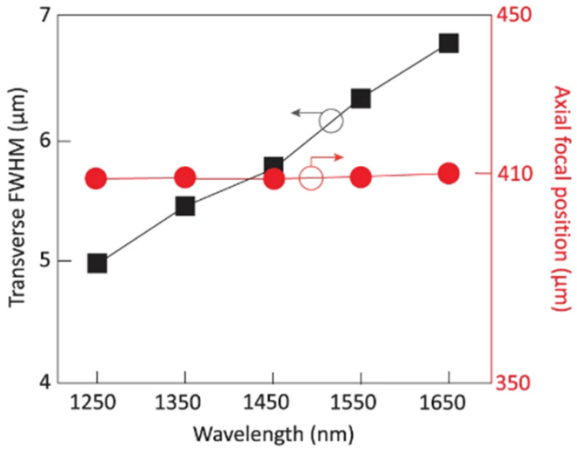


**Figure 4.18.: Experimentally characterized transverse FWHM and the axial focal positions of the achromatic metafiber at different wavelengths.**

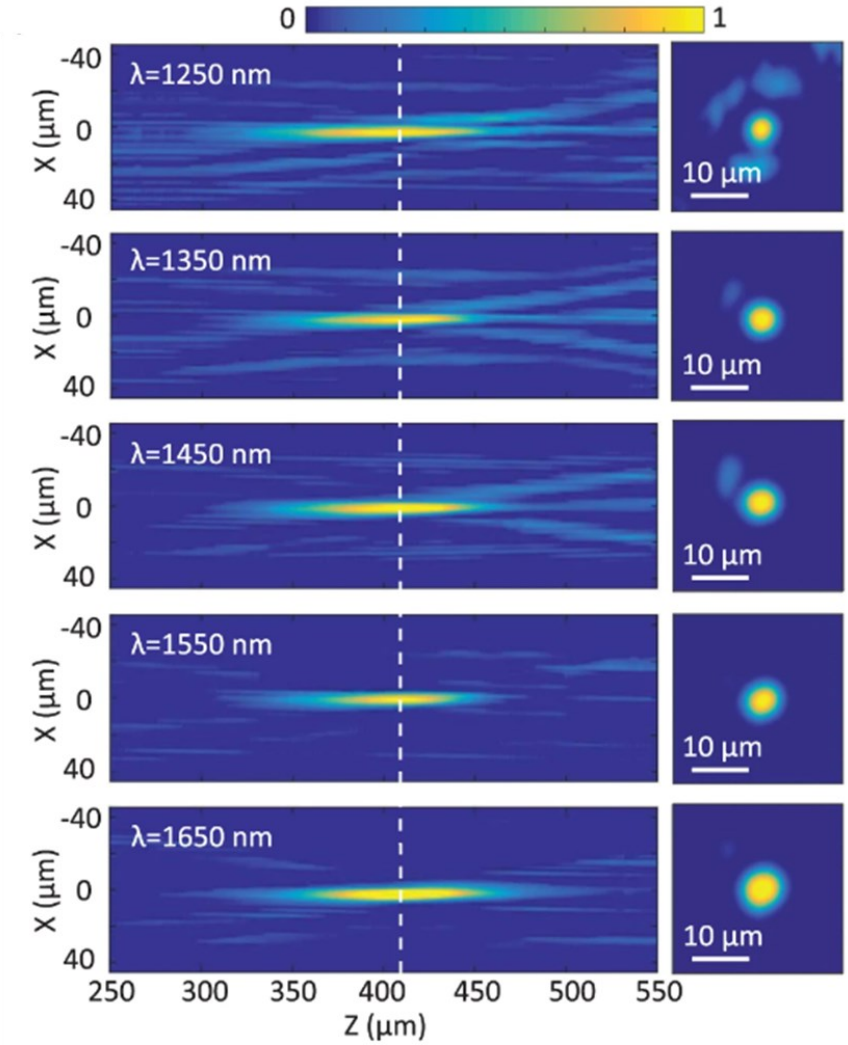


**Figure 4.19.: Experimentally characterized point-spread functions of the achromatic metafiber in both longitudinal (left) and transverse (right) planes.**

Achromatic imaging using a flexible fiber represents the ultimate objective of the developed

achromatic metafiber. While metalenses offer a promising avenue for miniaturizing fiber-optic imaging systems, their utility is impeded by severe chromatic aberrations, rendering them unsuitable for multiwavelength and broadband imaging applications. In order to explicitly demonstrate the advanced performance of an achromatic metafiber for broadband imaging, we first simulated and compared imaging results of achromatic and chromatic metalens-implemented SMFs. Owing to the confocal imaging principle, the metalens collects object signals of different wavelengths at different focal planes through convoluting diffraction-limited point-spread-functions with the corresponding object signals at different planes. Figure 4.20 is a schematic diagram of achromatic imaging. Transmitted light under a broad illumination from a moving object placed on a 3D piezo nanopositioning stage was directly collected by the achromatic metafiber (the metalens side). At its other end, the intensity of fiber transmitted light signals was measured by a Ge-amplified photodetector (PDA50B2, Thorlabs).

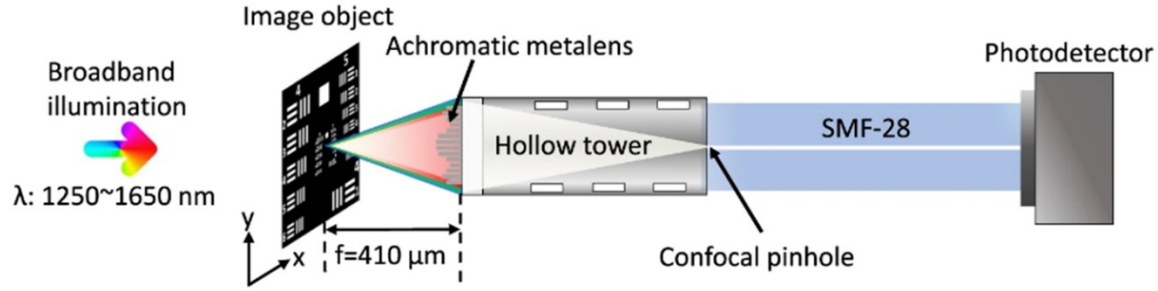


**Figure 4.20.: Schematic diagram of achromatic metafiber imaging**

Here, we applied the 3D-nanoprinted achromatic metafiber for fiber-optic confocal scanning imaging without involving any other microscope components. In our experiment, we used a standard United States Air Force (USAF) 1951 resolution chart to investigate the resolution limit of our achromatic metafiber-based confocal imaging. Figure 4.20 presents imaging results obtained using achromatic metafibers and chromatic metafibers across the entire telecommunications wavelength range from 1.25 to 1.65 μm. Sharp images of various resolution targets, ranging from 11.05 μm (Group 5 element 4) to 8.77 μm (Group 5 element 6), were successfully acquired using the achromatic metafiber. We compared the imaging performance of achromatic metafibers and chromatic metafibers by scanning the same target area. The results demonstrate that when using colored metafibers, the image response becomes blurred, and the image intensity and contrast at different wavelengths are significantly reduced. This degradation can be attributed to the inherent axial and lateral chromatic aberration of colored metalenses, which impede clear focused imaging responses, thus adversely affecting image collection efficiency and contrast in confocal scanning images.

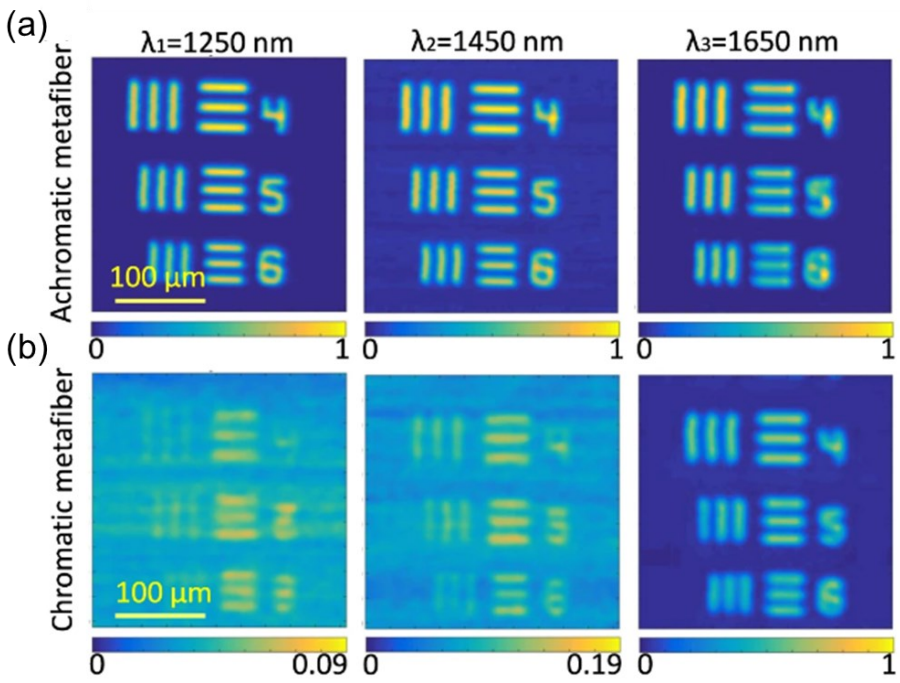


**Figure 4.21.: Experimentally obtained confocal imaging results of the USAF resolution test chart based on the achromatic metafiber (a) and chromatic metafiber (b).**

We also conducted a comparative analysis of the imaging capabilities of achromatic and chromatic super optical fibers across a broad spectrum. (Figure 4.22) Our experimental findings reveal that the flexible achromatic metafiber generates in-focus images under broadband light illumination spanning the entire telecommunication regime, with a spatial resolution up to 4.92 µm. These results show that the achromatic metafiber we designed and fabricated, demonstrating excellent optical performance and diffraction-limited imaging capabilities. Moreover, our 3D optics facilitate not only the miniaturization of endoscopic imaging systems but also extend their wavelength coverage by delivering high image quality under broadband illumination.

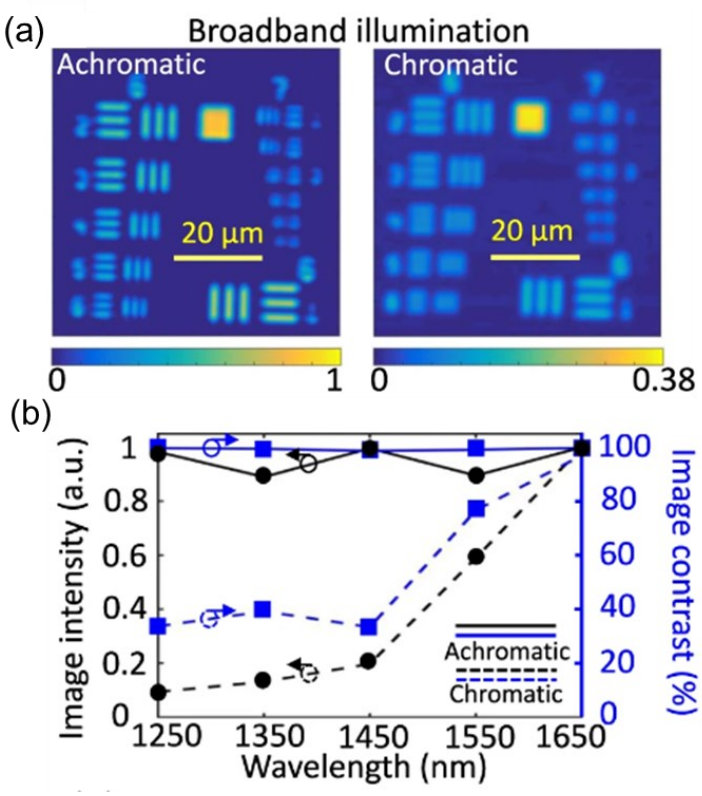


**Figure 4.22.: Achromatic and chromatic metafiber characterization results under broadband illumination.** (a) Experimentally obtained confocal imaging results based on the achromatic (left) and chromatic (right) metafibers under broadband illumination that consists of 8 equally spaced wavelength channels ranging from 1250 to 1650 nm. (b) Averaged image intensity (black color) and image contrast (blue color) of the experimentally obtained images at different wavelengths, based on the achromatic (solid lines) and chromatic (dashed lines) metafibers, respectively.

## 4.5 Conclusion

We have successfully demonstrated the compensation of chromatic dispersion in a fiber-integrated lens using 3D-nanoprinted meta-optics, thereby enabling a wide modulation range of the TBP and group delay. By fixing the in-plane rotation angles of nanopillar meta-atoms to 0 and 90 degrees, our 3D achromatic metalens achieves insensitivity to the incident polarization of light. Experimentally characterizing the focusing performance of a miniaturized 3D-nanoprinted achromatic metafiber, we observed an achromatic focus with a consistent focal length across the entire telecommunication and single-mode domain of a commercial SMF, spanning from 1.25 to 1.65 µm. Furthermore, direct confocal scanning imaging with our developed flexible achromatic metafiber produced in-focus sharp images (with spatial resolution up to 4.92 µm) under broadband light illumination.

We foresee that our compact and flexible achromatic metafiber could serve as a replacement for conventional optical table-based confocal imaging systems, offering enhanced flexibility and reduced alignment challenges. Additionally, our achromatic metafiber holds promise for

femtosecond laser-assisted therapy and surgery, facilitating the achromatic focusing of femtosecond laser pulses with typical bandwidths of several hundreds of nanometers. Alternatively, while multimode fibers have been developed for endoscopic imaging, their use typically necessitates a calibration setup to measure the fiber's transmission matrix, increasing the complexity of a fiber endoscope compared to single-mode fibers. Moreover, employing a single-mode delivery fiber mitigates the fiber's susceptibility to external influences such as bending, making it particularly advantageous for remote applications like in vivo optical coherence tomography and optical sensing.

Therefore, our demonstrated highly compact and flexible achromatic metafiber unlocks the full potential of fiber meta-optics for diverse photonic applications, encompassing nonlinear fiber lasers, wavelength-multiplexing-based fiber-optic communications, deep tissue imaging, and hyperspectral imaging in confocal endomicroscopy.

# 5. Phase and polarization control based on 3D metasurface.

*The results presented in this chapter are published in the scientific open-access journal Nature Communications (**Chenhao Li**, et al. Nature Communications 14, 7222 (2023), see ref.[106]). As a basis of the chapter, the peer-reviewed manuscript is used and complete sentences or even paragraphs will be taken word by word from the manuscript along with graphic content/figures since Springer Nature allows the reprinting of own contributions in theses, also in accordance with the terms of the CC-BY Creative Commons Attribution 4.0 International license http://creativecommons.org/licenses/by/4.0/.*

Structured light has emerged as a valuable tool across various photonic applications. However, its utilization within optical fiber science and technology is presently constrained by challenges such as mode mixing and the absence of integrated optical elements for on-fiber wavefront engineering. Consequently, the generation of structured light predominantly occurs external to the fiber, relying on bulky optics in free space. In this study, we present a novel metafiber platform capable of generating arbitrarily structured light on the hybrid-order Poincaré sphere. Utilizing polymeric metasurfaces endowed with a height degree of freedom in height and an expanded library of 3D meta-atoms, we employed 3D laser nanoprinting techniques to fabricate these metasurfaces. Subsequently, we interfaced them with polarization-maintaining single-mode fibers. Through this integration, multiple metasurfaces were affixed onto the fiber end-faces, facilitating the transformation of the fiber output into diverse structured light fields. These included cylindrical vector beams, circularly polarized vortex beams, and arbitrary vector fields.

## 5.1 Introduction

Light, as an electromagnetic wave, has a variety of properties that can be used to encode information, including amplitude, wavelength, phase, and polarization (the vibration direction of the electric field in the transverse plane). Mathematically, light can be represented by $A\vec{e}cos(kx + \omega t + \varphi)$, where each degree of freedom (DoFs) corresponds to an intrinsic property (Figure 5.1) [107]. These configurations of light, often referred to as structured light, encompass the arbitrarily light field across all DoFs, spanning from space to time. Structured light with complex light fields can theoretically encode unlimited information, thus has board prospects in communications.

The origins of structured light research can be traced back to the seminal experiment conducted by Thomas Young. He observed a stripe pattern resulting from the interference of double-slit plane waves, thereby revealing the existence of one-dimensional (1D) intensity structured light while also providing evidence for the wave nature of light [108]. Following Young's experiment,

research on structured light progressed steadily, evolving from the study of simple 1D structured light to investigations involving higher dimensions.

This discovery revolutionized the field, demonstrating that by manipulating the phase of light, it is possible to generate photons that carry orbital angular momentum. However, the truly exciting aspect of this field lies in combining degrees of freedom to create exotic structured light. A significant milestone is the realization that by combining polarization and phase, vector vortex light can be obtained. Vector vortex light is a polarization spatial vector that carries a coupled mode of spin angular momentum (SAM) and OAM. The inseparable superposition state, composed of SAM-OAM dual degrees of freedom, also corresponds precisely to the two-bit quantum entangled state. This finding holds immense value for studying basic physical phenomena such as the interaction between light and matter, as well as classical quantum coupling systems. Furthermore, it has found applications in various fields, including advanced areas like high-capacity optical communications [109, 110], light detection and sensing [111-114], optical tweezers and particle manipulation [115-119], superresolution [67, 120-122], phase-contrast imaging [123-125], pattern recognition [126]. Therefore, vector vortex light is currently the most important and widely used structured light. The purpose of this chapter is to regulate the polarization and phase of the optical fiber exit light field, that is, to generate vector vortex light.

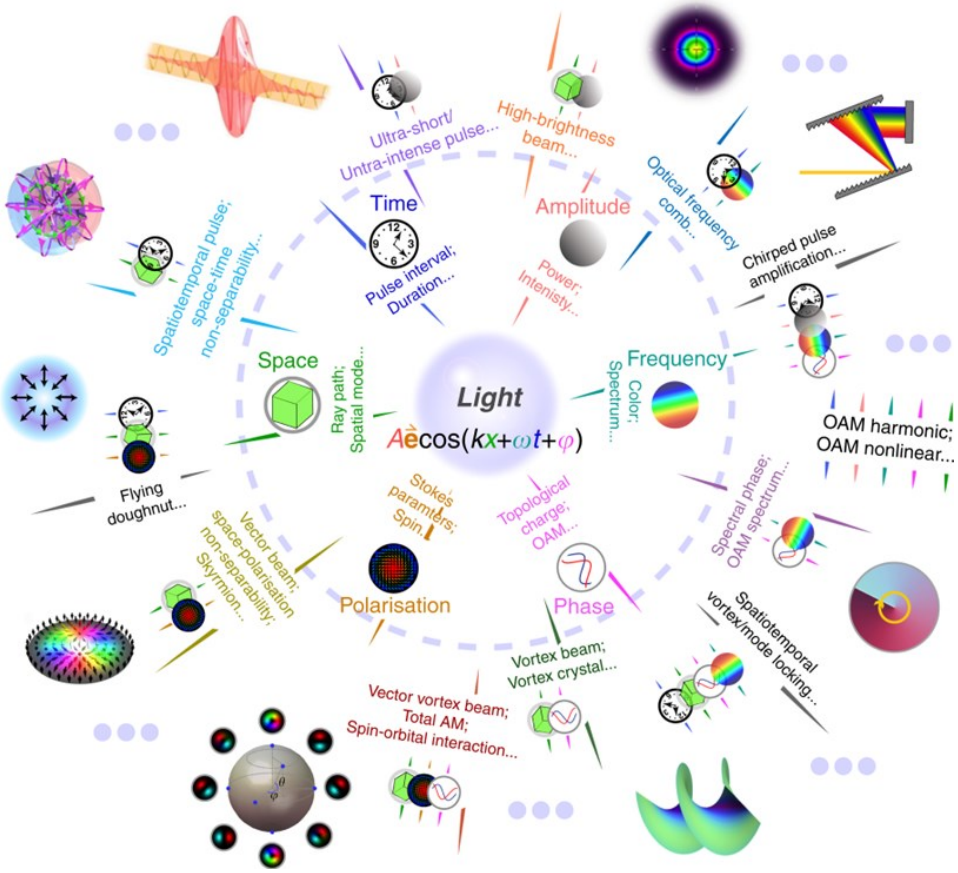


**Figure 5.1. By tailoring the on-demand structured light distributions of combined DoFs, various non-separable states can be produced.** Adapted from [107].

The mathematical description of vector vortex light can be derived from Maxwell's equations.

Beginning with the Helmholtz equation and considering the paraxial approximation, the wave equation can be expressed as:

$$\left(\nabla^2 + 2ik\frac{\partial}{\partial z}\right)\psi(\boldsymbol{r}) = 0, \qquad (5-1)$$

where $\nabla^2$ is the Laplace operator, $\boldsymbol{r}$ is the coordinate vector and $\psi$ represents the distribution field of light. Solving equation (5-1) yields various modes, with three particularly significant ones: the Hermite Gaussian (HG) mode, the Laguerre Gaussian (LG) mode, and the Ince-Gaussian (IG) mode. The HG mode embodies vector light, the LG mode is associated with OAM, and the IG mode serves as an intermediate mode between the two. Since the three modes are all solutions of the wave equation under paraxial approximation conditions, they can be transformed into each other according to orthogonal completeness. In addition, the orthogonal complete solution also enables the linear superposition of any mode in a set of modes to still satisfy the wave equation, so the superposition of the light fields of these modes usually produces light fields with new structures and characteristics.

Conventional methods for generating structured light often rely on multiple cascaded phase and wave plates, such as bulky spatial light modulators. However, recent advancements in metasurfaces, composed of subwavelength meta-atoms, have revolutionized photonic design by enabling the creation, detection, and manipulation of structured light using ultrathin photonic devices. Plasmonic and dielectric meta-atoms, capable of imparting phase shifts ranging from 0 to $2\pi$ on scattered light, have been developed to generate phase singularities carrying the orbital angular momentum (OAM) of light. Additionally, anisotropic meta-atoms have been engineered to act as subwavelength waveplates, allowing for the imprinting of polarization singularities in cylindrical vector beams and perfect Poincaré beams.

While implementing structured light on optical fibers holds significant promise for a wide range of fiber applications, including fiber communications, fiber lasers, and fiber sensors, practical challenges remain. Modal crosstalk, polarization mixing, and the lack of integrated optical elements for complex wavefront manipulation hinder the widespread use of structured light from optical fibers. Currently, structured light generation predominantly occurs outside the fiber using bulky optics in free space, limiting its deployment in fiber science and technology and partially negating the advantages of optical fibers, such as flexible light guidance. Several promising approaches have been explored to integrate meta-structures onto fiber end faces, facilitating the demonstration of Bessel beam converters [127], fiber couplers [128], polarization controllers, and waveplates [129]. Although techniques such as electron- [130-132] and ion-beam [133, 134] lithography, nanoimprinting [135], and chemical etching [136] have been proposed for fabricating metasurfaces on fiber end faces, these methods often involve complex manufacturing processes or encounter difficulties in interfacing arbitrary 3D nanostructures for efficient wavefront engineering.

3D laser nanoprinting, based on two-photon polymerization, has emerged as a promising technique for interfacing 3D micro-optics on fiber tips. Laser-nanoprinted lenses with high numerical aperture, achromatic focusing, multifocus generation, and inverse-design optimization have been successfully integrated onto fiber end faces to enhance fiber functionalities and applications. However, the direct realization of arbitrarily structured light

on optical fibers remains a challenge.

## 5.2 Theory

Just as polarized light can be parameterized using a Poincaré sphere, structured Gaussian modes can also be represented on this sphere. LG modes, which carry OAM with opposite signs, correspond to points at the north and south poles, akin to circular polarization states on a High-order Poincaré sphere (HOPS), as shown in Figure 5.2. Hermite-Gaussian HG modes, displaying different orientations, akin to linear polarization states, are situated on the equator. The counterparts of elliptical polarization states are the IG modes, which occupy positions between LG and HG beams on the sphere.

Due to orthogonal completeness, an arbitrarily structured light field on the HOPS can be defined mathematically as a superposition of left- and right-handed circular polarization components ($|L\rangle$ and $|R\rangle$) carrying different OAM modes:

$$|\psi\rangle = \cos\left(\frac{\theta}{2}\right)|m\rangle|R\rangle + e^{i\alpha}\sin\left(\frac{\theta}{2}\right)|n\rangle|L\rangle, \qquad (5-2)$$

where $\theta$ and $\alpha$ represent the weighted amplitude parameter and relative phase contributions of the circular polarization components, respectively. $m$ and $n$ denote the topological charges of the OAM modes in the right- and left-handed circular polarization components, respectively.

By mathematical transformation, Equation (5-2) can be rewritten as Jones vectors in the linear polarization basis (x-linear and y-linear polarizations):

$$|\psi\rangle = \frac{1}{\sqrt{2}}\begin{bmatrix} \cos\left(\frac{\theta}{2}\right)e^{im\zeta} + \sin\left(\frac{\theta}{2}\right)e^{in\zeta}e^{i\alpha} \\ -i\left(\cos\left(\frac{\theta}{2}\right)e^{im\zeta} - \sin\left(\frac{\theta}{2}\right)e^{in\zeta}e^{i\alpha}\right) \end{bmatrix}, \qquad (5-3)$$

where $\zeta$ is the azimuthal angle in the transverse cross-section plane of a structured light field. Equation (5-3) can be used to define different vector beams on the HOPS with spatially variant polarization distributions.

In this chapter, our objective is to develop a highly versatile optical fiber platform capable of generating arbitrary structured light on the HOPS. To illustrate our concept effectively, we present the design and implementation of several diverse structured light-generating metafibers (SLGM). These SLGM variants exhibit a range of structured light outputs, including radial polarization (SLGM-1), azimuthal polarization (SLGM-2), Circularly Polarized Vortex Beams with topological charges of -1 (SLGM-3) and -3 (SLGM-4), and spatially varying localized elliptical polarization representing arbitrary vector fields on HOPS (SLGM-5). Refer to Figure 5.2 I-V for visual representations of these SLGM configurations.

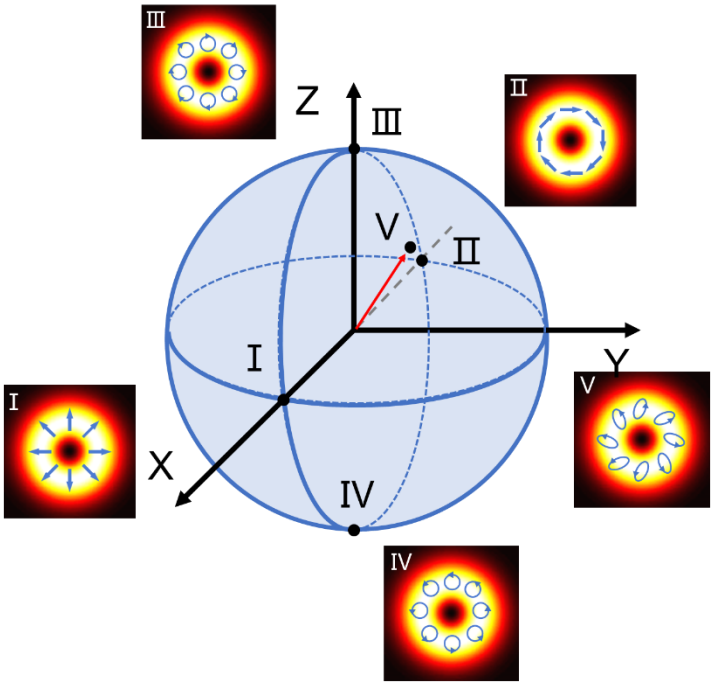


**Figure 5.2. The realized structured light fields on a HOPS carry spatially variant polarization distributions, with some examples indicated by the states I to V.** The arrows refer to the local polarization of the electric field.

## 5.3 Design

Here, we present the methodology for designing 3D polymeric metasurfaces tailored for the realization of vector beams on the HOPS. Utilizing advanced 3D laser-nanoprinting techniques, nanopillar waveguides were fabricated within a polymer matrix, serving as the fundamental building blocks or meta-atoms (see Figure 5.3). In order to impart robust birefringence essential for precise polarization manipulation, we engineered these nanopillars to exhibit anisotropic characteristics, featuring rectangular cross-sections. These structures support distinct waveguide modes associated with polarizations along their short and long axes. Consequently, the meta-atom's behavior aligns with that of a linearly birefringent wave plate, as described by its corresponding Jones matrix:

$$M = R(\gamma)\begin{bmatrix} t_x e^{i\varphi_x} & 0 \\ 0 & t_y e^{i\varphi_y} \end{bmatrix} R^{-1}(\gamma) \qquad (5-4)$$

where $\gamma$ is the in-plane rotation angle of the nanopillar, $t_x$ and $t_y$ are the absolute transmission amplitudes of the transverse modes polarized in the x and y directions, respectively. This element introduces both amplitude ($t_x$, $t_y$) and phase ($\varphi_x$, $\varphi_y$) modulations on light linearly polarized along the x and y axes. The rotation matrix $R(\gamma)$ is defined as $\begin{bmatrix} \cos(\gamma) & \sin(\gamma) \\ -\sin(\gamma) & \cos(\gamma) \end{bmatrix}$, representing a coordinate system transformation.

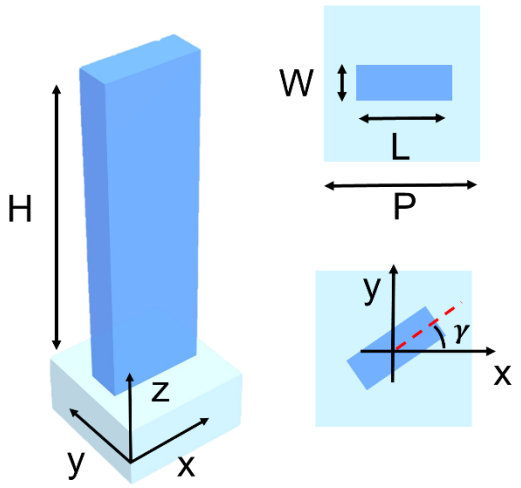


**Figure 5.3. Schematic of a 3D laser nanoprinted nanopillar waveguide in a polymer matrix**

Therefore, considering an arbitrary input light with a characteristic electric field $E_{in}$ passing through the meta-atoms, the resultant output light electric field can be represented as $E_{out} = ME_{in}$.

In this specific scenario, we assume the incident light to be linearly polarized along the x-axis. This selection is prompted by the prevalent uncertainty regarding the polarization state of outgoing light in typical commercial optical fibers. To ensure the polarization state of the outgoing light is stable, we opt for commercial polarization-maintaining single-mode fiber (PM-SMF, PM1550-XP, Thorlabs) to build up the metafiber platform, where the outgoing light emerges as linearly polarized.

Given this setup, the Jones matrix describing the polarization state of the incident light is represented as $\begin{bmatrix}1\\0\end{bmatrix}$. Consequently, the expression for the output light electric field is formulated as:

$$E_{\text{out}} = \begin{bmatrix} t_{\text{x}}\cos^2(\gamma)e^{i\varphi_{\text{x}}} + t_{\text{y}}\sin^2(\gamma)e^{i\varphi_y} \\ \cos(\gamma)\sin(\gamma)\,t_{\text{y}}e^{i\varphi_y} - \cos(\gamma)\sin(\gamma)\,t_{\text{x}}e^{i\varphi_x} \end{bmatrix} \qquad (5-5)$$

Upon simplification, the output light after passing through an anisotropic nanopillar waveguide can be expressed as:

$$E_{\text{out}} = e^{i\varphi_{\text{x}}} \begin{bmatrix} t_{\text{x}}\cos^2(\gamma) + t_{\text{y}}\sin^2(\gamma)e^{i\Delta\varphi} \\ \frac{1}{2}(t_{\text{x}} - t_{\text{y}}e^{i\Delta\varphi})\sin(2\gamma) \end{bmatrix} \qquad (5-6)$$

Where $\Delta\varphi = \varphi_{\text{x}} - \varphi_{\text{y}}$ is the phase difference between the modes polarized along the x and y axes, respectively. All these parameters are spatially dependent as functions of x and y.

Equation (5-6) indicates that both the polarization (controlled by $\Delta\varphi$) and phase ($\varphi_{\text{x}}$) of an output beam can be controlled simultaneously by a single nanopillar, which forms the physical

basis for implementing any arbitrarily structured light field. The key to our design is to find 3D nanopillars to be arranged in a particular distribution so that their optical responses can be precisely matched with any desired structured light field defined in Equation (5-3).

We have established a comprehensive 3D meta-atom library utilizing the rigorous coupled-wave analysis method, specifically tailored for a telecommunication wavelength of 1550 nm (refer to Figure 5.4 a). Notably, the inclusion of the height degree of freedom in our 3D nanopillars results in a significantly expanded meta-atom library, characterized by a rich 3D dataset. This expanded repertoire equips us with a versatile resource capable of precisely matching any desired polarization and phase responses.

Our simulation endeavors focus on elucidating the phase difference between the x- and y-polarized transverse modes, along with the propagation phase of the x-linear polarization. For these simulations, we consider 3D nanopillars fabricated from a lossless commercial polymer material IP-L, boasting an index of 1.5. These nanopillars feature a fixed pitch distance of P = 2.2 μm, a length L in the range of 0.8-1.8 μm, a width W of 0.5-1.1 μm, and a height H of 6-14 μm. Both the polarization eigenstates feature high transmission efficiency.

Our investigations reveal that 3D nanopillars boast a wide dynamic range, spanning from 0 to π in the phase difference. Consequently, they function effectively as waveplates, capable of converting an incident x-linear polarization into various polarization outputs. Specifically, when the phase difference equals π, the corresponding nanopillars operate as half-wave plates, facilitating the rotation of the incident linear polarization angle. This capability lays the groundwork for the generation of diverse cylindrical vector beams positioned on the equator of the HOPS.

In contrast, when the phase difference equals π/2, each nanopillar functions as a quarter-wave plate, transforming the linear polarization input into circular polarization. This configuration enables access to the poles of the HOPS. Moreover, for phase differences other than π or π/2, the nanopillars can convert the linear polarization into various elliptical polarizations, thereby enabling access to any desired state on the HOPS.

To enhance the visualization of the extensive coverage offered by our 3D meta-atom library in terms of phase difference and propagation phase responses, we highlight three distinct planes within our dataset, featuring nanopillar heights of $H$=8, 10, and 12$\mu m$ (as depicted in Figure 5.4 b). For instance, by selecting 3D nanopillars of varying heights, we can effectively emulate the functionality of half- or quarter-wave plates, while simultaneously spanning the entire range (0 to 2$\pi$) of the phase response. Therefore, our results suggest that 3D nanopillars with the unlocked height degree of freedom provide a powerful platform for implementing arbitrarily structured light.

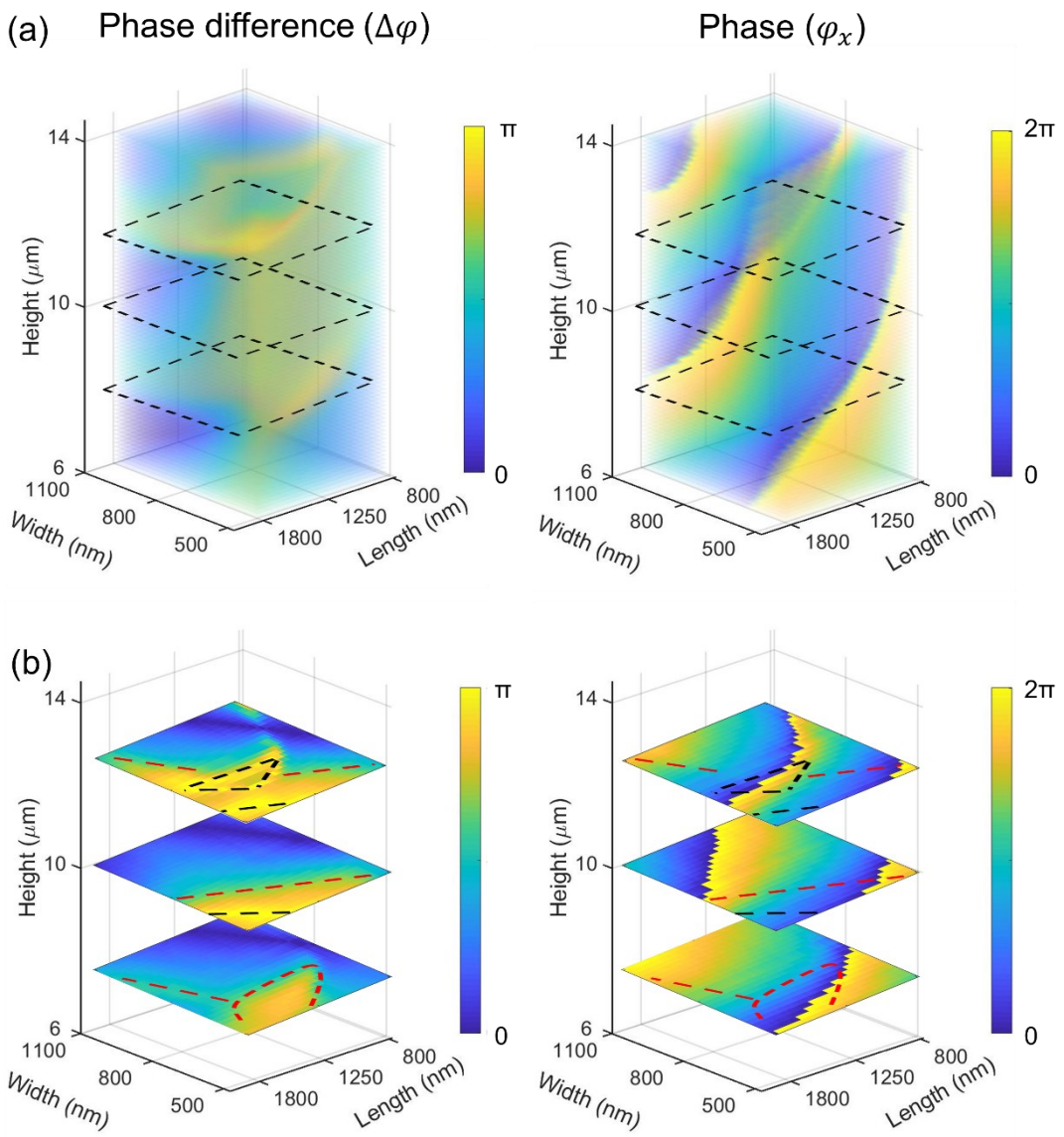


**Figure 5.4. Simulation library of the 3D meta-atom (**a) Simulated 3D meta-atom library consists of the phase difference between the x- and y-linear transverse modes (left) and the propagation phase of the light polarized along the x-direction (right). (b) Three exemplary data planes in the meta-atom library are highlighted, with heights of H = 8, 10, 12 μm, respectively. Red and black dashed lines mark the 3D nanopillars satisfying phase differences of π /2 and π, respectively.

## 5.4 Experiments and characterization

In this section, we picked up five distinct vector states situated on the HOPS to demonstrate our SLGM concept. These include cylindrical vector beams on the equator of the first-order HOPS, circularly polarized vortex beams carrying different OAM modes sitting on the poles of the first- and third-order HOPS, and an arbitrary vector state on the HOPS carrying a spatially variant elliptical polarization distribution.

### Cylindrical vector beams on SLGMs

Cylindrical vector beams, located at the equator of the first-order HOPS ($m = -n = 1$), are a special group of spatially variant vector beams with localized linear polarization. As typical examples of cylindrical vector beams, we experimentally demonstrate two SLGMs that can produce radial (SLGM-1) and azimuthal (SLGM-2) polarizations. To obtain these states, the weighted amplitude parameter $\theta$ in Equation (5-3) is set to $\frac{\pi}{2}$ and relative phase $\alpha$ to 0 and π, respectively. The resulting radial and azimuthal polarization states are given as $|\psi_r\rangle = \begin{bmatrix} cos\zeta(x,y) \\ sin\zeta(x,y) \end{bmatrix}$ and $|\psi_a\rangle = \begin{bmatrix} sin\zeta(x,y) \\ -cos\zeta(x,y) \end{bmatrix}$, respectively, where $\zeta(x,y)$ is the azimuthal angle in the transverse cross-section of the vector beams.

To fulfill the requisite polarization distributions, we employed a single-sized 3D nanopillar (Figure. 5.5 a) that behaves like a half-wave plate. The nanopillar waveguide has a length L of 1.60 μm, a width W of 0.55 μm, and a height H of 11 μm. Notably, our analysis demonstrates that this nanopillar exhibits both high transmission efficiency and a $\pi$ phase difference between the x- and y-linear transverse modes across the entire S, C and L telecommunication bands, from 1.45 to 1.65 μm as illustrated in Figure 5.5b. In this case, Equation (5-6) can then be simplified as $E_{out}(x,y) = \begin{bmatrix} \cos[2\gamma(x,y)] \\ \sin[2\gamma(x,y)] \end{bmatrix}$ by assuming $t_x \approx t_y \approx 1$.

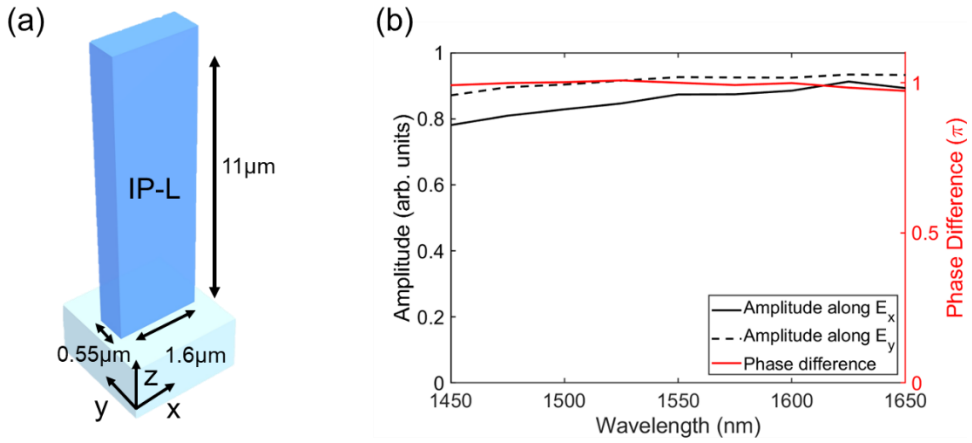


**Figure 5.5.: The 3D meta-atom for cylindrical vector beam generation.** (a) Schematic representation of the used 3D nanopillar meta-atom. (b) Simulated nanopillar response across a broad spectral range across the whole telecommunication band.

As such, for the radial polarization output, its localized linear polarization angle $\zeta(x,y)$ can be easily controlled by the in-plane rotation angle $\gamma(x,y)$ of the nanopillar. Figure 5.6 shows the relationship between polarization angle and meta-atom rotation angle. To achieve the azimuthal polarization output, we can simply rotate all the nanopillars used for the above radial polarization by 45 degrees.

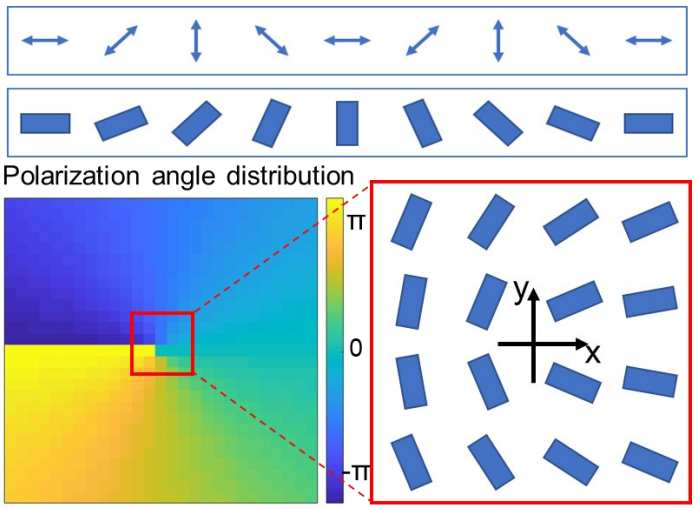


**Figure 5.6.: Illustration of the in-plane angle distribution of 3D nanopillars used for creating the radial vector state.**

After finalizing the design of the super optical fiber, we applied the methodology described in Chapter 3 to process and fabricate SLGMs capable of generating radial and azimuthal vector light. To ensure that the emergent light fully covers the metasurface, a cylindrical vector beam metasurface with a diameter of 100 µm was 3D laser nanoprinted on top of a hollow tower structure (height 550 µm) and connected to the PM-SMF end face. Figure 5.7 presents a side-view scanning electron microscope (SEM) image of SLGM-1, which produces a radially polarized output, clearly showing the 3D nanopillar metasurface at the top of the tower.

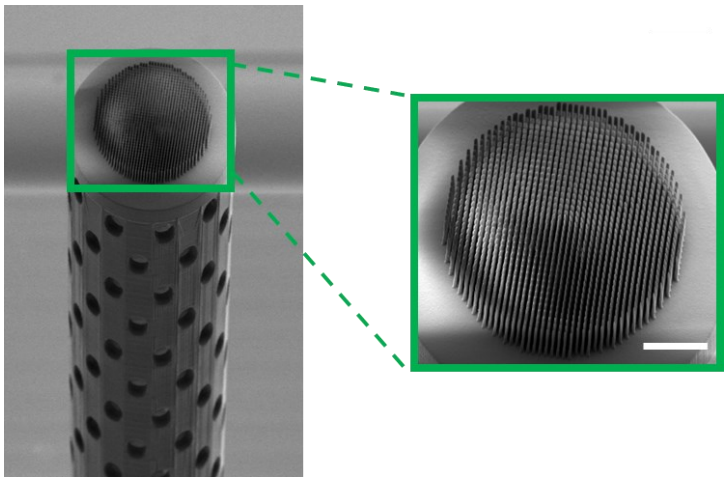

**Figure 5.7.: SEM image of SLGM-1 used for creating the radial vector beam.** (scale bar: 25 µm)

To characterize the cylindrical vector beams generated by the SLGMs, we constructed the optical system capable of imaging in momentum-space, as shown in Figure 5.8. A linearly polarized 1550 nm laser beam from a supercontinuum laser source (SuperK Fianium, NKT Photonics) and an infrared wavelength selector (SuperK Select, NKT Photonics) was coupled into the unstructured end of the SLGMs. The SLGM outputs were characterized using a home-built optical imaging setup with 15x magnification and the results were recorded using a near-

infrared camera (Raptor, Owl 640 M).

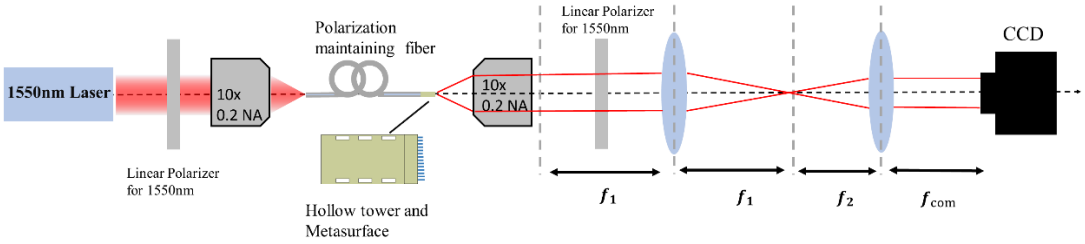


**Figure 5.8.: Optical setup for SLM characterization in momentum-space.**

Subsequently, the placement of a linear polarizer in front of the camera, and rotation of the polarizer produces a double-lobed intensity pattern aligned with the linear polarizer axis, enabling us to identify the SLGM output as radial (Figure 5.9a) and azimuthal (Figure 5.9b) vector beams. Specifically, the lobes follow the direction of the linear polarizer's axis, confirming the generation of a cylindrically polarized beam. It is worth noting that the intensity of the lobe pattern appears non-uniform, which may be attributed to misalignment between the fiber output beam and the metasurface. Further details will be discussed later.

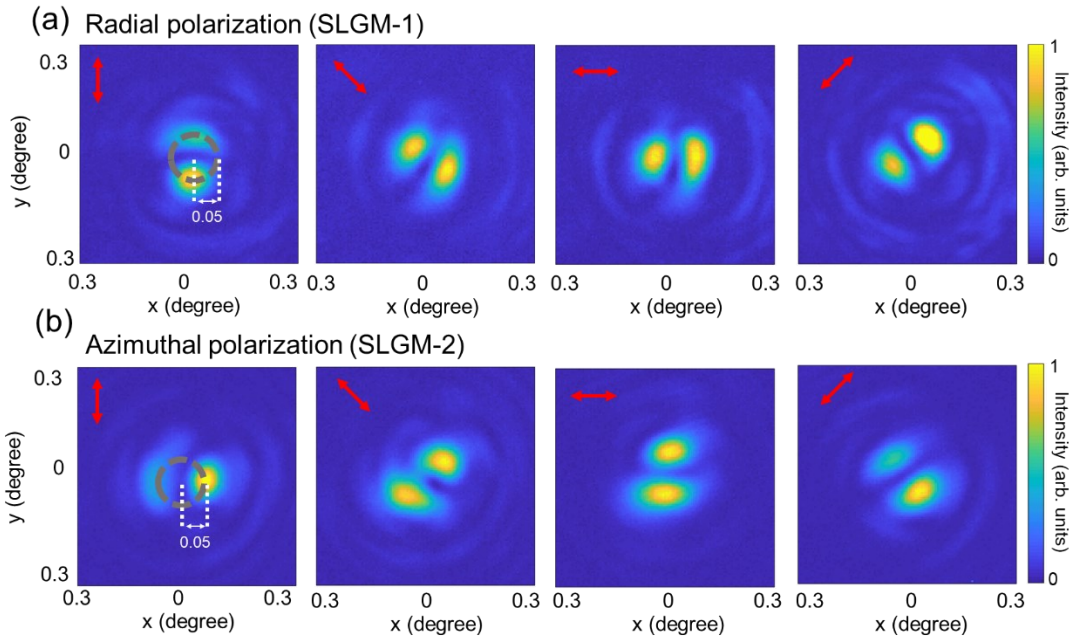


**Figure 5.9.: Experimentally measured intensity patterns of the SLGM outputs of the radial (a) and azimuthal (b) vector beams, respectively.** The red arrows mark the polarization filtering axis of a linear polarizer inserted in front of the camera used for recording the polarization-dependent intensity profiles.

### Circularly polarized vortex beams on SLGMs

The circularly polarized vortex beams located at the poles of the HOPS represent the fundamental vector states of the generalized light field on the HOPS (see Equation 5-3). To fully demonstrate that our metafiber can generate arbitrary circularly polarized vortex beams,

we now present two additional SLGMs, which are capable of generating right- and left-handed circularly polarized vortex beams with topological charges of -1 and -3, respectively. (SLGM-3 and SLGM-4).

For the circularly polarized vortex beam at the north pole of the first-order HOPS ($m = -n = 1$), both the weighted amplitude parameter $\theta$ and relative phase $\alpha$ in Equation 5-3 are set to 0 (yielding sample SLGM-3). The corresponding circularly polarized vortex beam can be described mathematically as $|\psi_{R,-1}\rangle = \frac{1}{\sqrt{2}} e^{-i\zeta(x,y)} \begin{bmatrix} 1 \\ -i \end{bmatrix}$.

Similarly, for the circularly polarized vortex beam at the south pole of the third-order HOPS ($m = -n = 3$, for SLGM-4), the weighted amplitude parameter $\theta$ and relative phase $\alpha$ in Equation 5-3 are set to 0 and π, respectively, and the resulting beam is given as $|\psi_{L,-3}\rangle = \frac{1}{\sqrt{2}} e^{-i3\zeta(x,y)} \begin{bmatrix} 1 \\ i \end{bmatrix}$. To realize such vector states through a metasurface, independent control of both polarization and propagation phase is necessary.

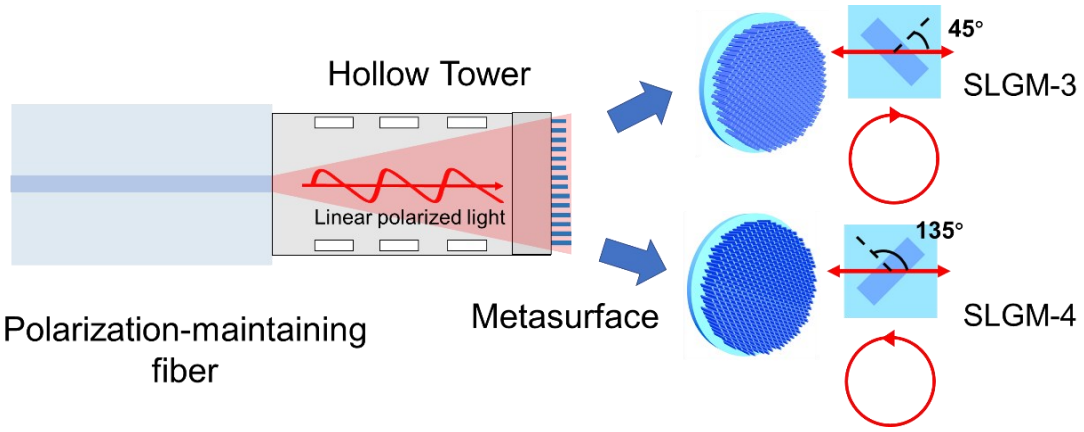


**Figure 5.10.: Schematic illustration of creating circularly polarized vortex beam outputs on metafibers**

We designed nanopillars to function like quarter-wave plates, having high transmission efficiency ($t_x \approx t_y \approx 1$) as well as a phase difference of $\frac{\pi}{2}$ between the x- and y-linear polarization modes. According to Equation (5-5), the nanopillar output should be expressed as $E_{out}(x,y) = e^{i\varphi_x(x,y)} \begin{bmatrix} \cos^2[\gamma(x,y)] + i * \sin^2[\gamma(x,y)] \\ \frac{1}{2}(1-i)\sin[2\gamma(x,y)] \end{bmatrix}$. By setting the in-plane rotation angle $\gamma(x,y)$ of the nanopillars to $\frac{\pi}{4}$ or $\frac{3\pi}{4}$, the outputs become right- or left-handed circularly polarized beams in the forms of $e^{i\varphi_x(x,y)} \begin{bmatrix} 1 \\ -i \end{bmatrix}$ and $e^{i\varphi_x(x,y)} \begin{bmatrix} 1 \\ i \end{bmatrix}$, respectively. Moreover, the propagation phase of x-linear polarization $\varphi_x$ can satisfy a helical phase distribution $e^{il\zeta}$, where $l$ denotes the topological charge of the OAM mode. Owing to the greatly extended 3D meta-atom library, we can find 3D nanopillars with the propagation phase response from 0 to $2\pi$,

allowing us to imprint different OAM modes while maintaining a nearly constant phase difference of $\frac{\pi}{2}$, as illustrated in figure 5.11.

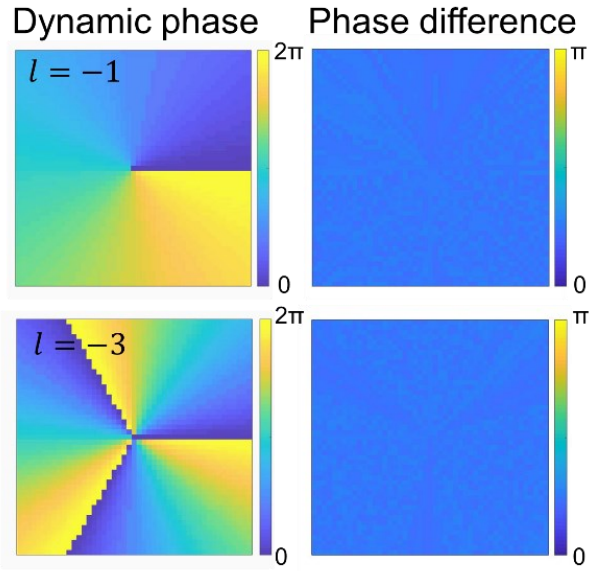


**Figure 5.11.: The specific propagation phase ($\varphi_x$) and phase difference ($\Delta\varphi$) maps for creating circularly polarized vortex beams of $|\psi_{R,-1}\rangle$ and $|\psi_{L,-3}\rangle$**

We utilized the same fabrication process described earlier to print two additional SLGMs with circularly polarized vortex beam outputs. Figure 5.12 presents the side-view SEM images of these SLGMs. To ensure precise polarization conversion, the x-axis of nanopillars were carefully aligned with respect to the polarization axis of the PM-SMFs by rotating them 45 and 135 degrees for the right- and left-handed circular polarization outputs, respectively.

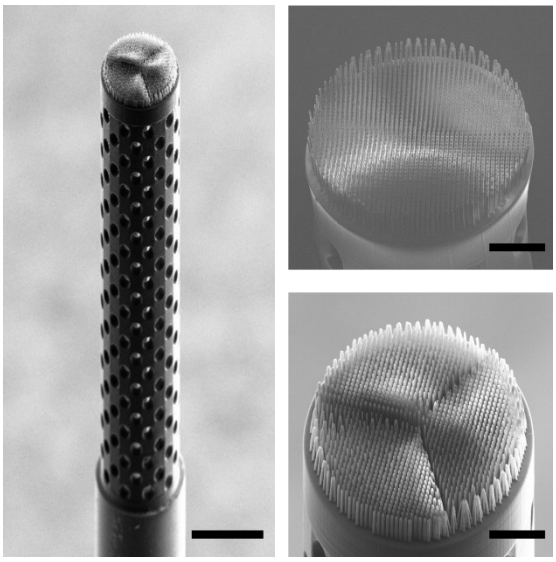

**Figure 5.12.: SEM images of the fabricated metafibers of SLGM-3.** (Scale bar: 100 μm). Bottom left and right: zoom-in areas of SLGM-3 and SLGM-4. (Scale bars: 25 μm).

To characterize the helical beams of the fiber outputs, we measured the Fourier plane image of the SLGMs (Figure 5.13). We found that doughnut-shaped beam patterns in the Fourier plane exhibit consistent divergence angles (SLGM3: 0.05° and SLGM4: 0.1°) with our simulation results, corroborating the nature of the transformed OAM beams. To consider only the OAM-induced beam divergence, we experimentally characterized the OAM beam divergence at a shifted Fourier plane that has the smallest beam sizes, through which we the fiber divergence is compensated.

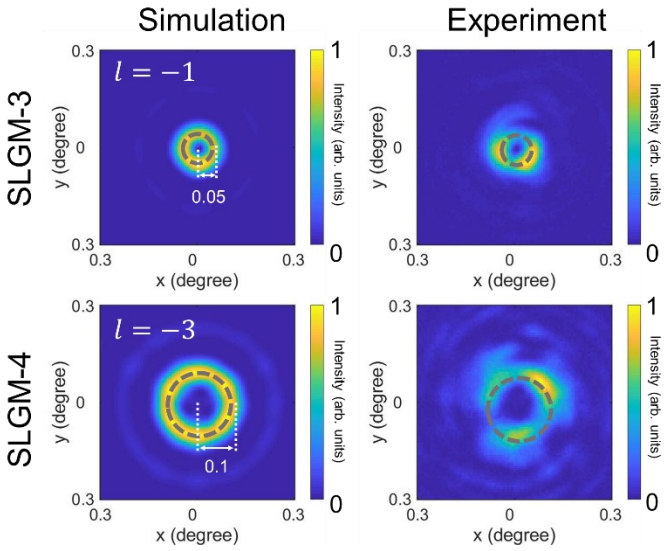


**Figure 5.13.: Simulation (left column) and experimental (right column) results of the intensity distributions of the two SLGMs in the Fourier plane.** The dashed circles mark the beam divergence angles of 0.05 and 0.1 degrees.

In addition, we noticed some interference effects in the intensity patterns, which we believe are mainly due to imperfect fiber cleaver such that the fiber output was not uniformly incident on the metasurfaces. A tilt of the fiber end face with respect to the fiber axis leads to a slightly tilted beam (Figure 5.14 a), which could be caused by imperfect fiber cleaving technique. This misalignment mainly results from the fiber cleaving quality, with the ideal situation that the cutting cross-section is flat and perpendicular to the fiber axis. For practical fiber cleaving, however, there is some imperfection that leads to a shifted fiber beam output.

To verify its impact, we simulated the influence of misalignment for the case of the sample producing azimuthal output polarization. Here we assume that the metasurface was misaligned by 20µm in x-direction and 5µm along the y-axis (after propagating 550µm from an imperfect cleaved fiber end face) with respect to the fiber output on the exit plane of the fiber tower. Here we calculate the impact of this misalignment on the generated OAM modes with different topological charges of -1 and -3.

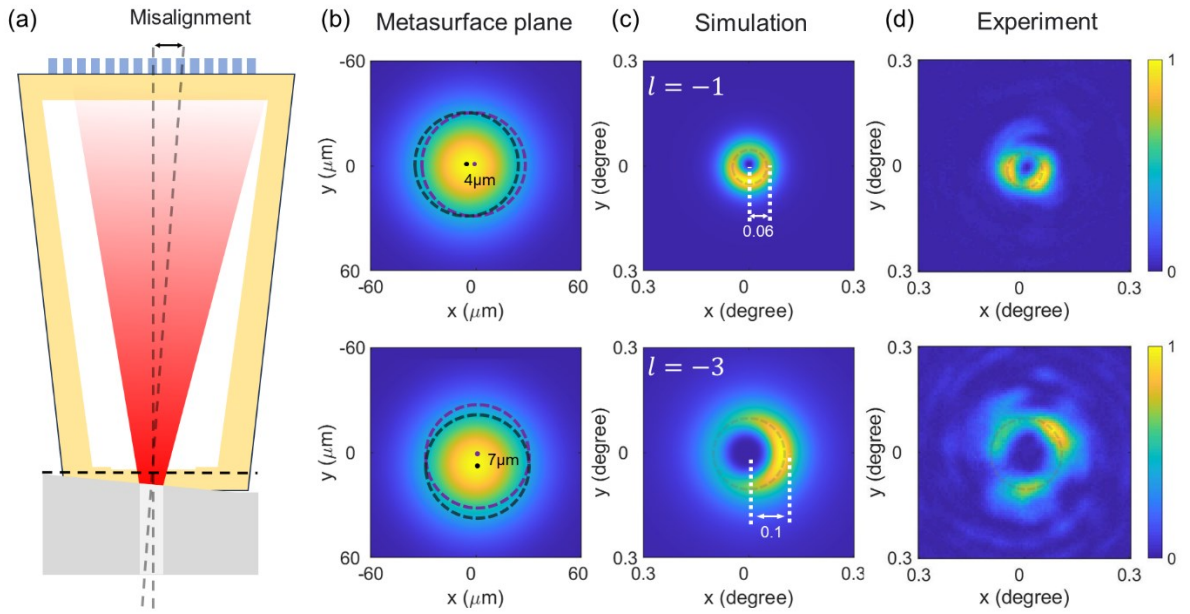


**Figure 5.14.: Impact of misalignment between the fiber output and metasurface on the structured light transformation.** (a) Schematic diagram of misalignment resulting from the cleaved fiber end face not being perpendicular to the fiber axis. (b) Simulation results of the OAM beam output carrying $l = -1$, considering a 4 μm shift along the x direction (top), and output beam carrying $l = -3$ with a 7 μm shift along the y-axis in the metasurface plane (bottom). The black and purple dots and the corresponding dotted lines represent the beam and metasurface, respectively. (c) Simulation results in Fourier Plane with the incident beam in (b). (d) The experiment results in our SLGM3 and 4. The dashed circles in (c) mark the beam divergence angle of 0.06 and 0.1, respectively.

Finally, to verify that the emitted light is circularly polarized, we placed a linear polarizer in front of the camera in figure 5.8 to detect its polarization state. By measuring the intensity of pattern at different polarizer angles, the polarization states of SLGM-3 and SLGM-4 were obtained. (Figure 5.15) Our experimental results confirm the successful generation of circularly polarized vortex beam outputs in both SLGMs, demonstrating a high degree of circular polarization.

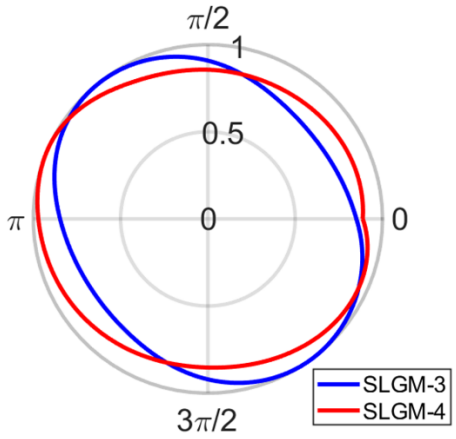


**Figure 5.15.: Polarization ellipticity analysis of the SLGMs measured by inserting a rotating linear polarizer before the camera.** The grey curve marks a perfectly circular polarized output.

**Arbitrarily structured light on SLGMs**

To further demonstrate the superiority of 3D metasurfaces, we randomly chose an arbitrary state on the first-order HOPS ($m = -n = 1$) and demonstrate the transformation of such state by designing, fabricating, and employing another SLGM (SLGM-5). The weighted amplitude parameter $\theta$ and relative phase $\alpha$ in Equation (5-3) are set as $2\tan^{-1}\left(\frac{1}{3}\right)$ and $\frac{\pi}{4}$, respectively, leading to a vector state written as $|\psi\rangle = \frac{\sqrt{2}}{20}\begin{bmatrix} 3e^{i\zeta(x,y)} + e^{-i(\zeta(x,y)-\frac{\pi}{4})} \\ -i(3e^{i\zeta(x,y)} - e^{-i(\zeta(x,y)-\frac{\pi}{4})}) \end{bmatrix}$. It corresponds to an elliptically polarized state with an ellipticity ratio (a/b defined in Figure. 5.16b) of 2 and the polarization directions $\psi$ (semi-major axes) are spatially related to azimuthal angle $\zeta(x, y)$.

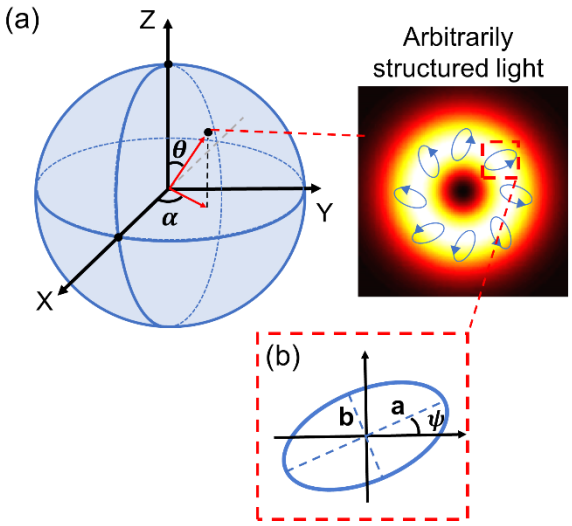


**Figure 5.16.: An arbitrarily structured light on HOPS.** (a) Schematic representation of the desired arbitrarily structured light field on the HOPS including the intensity and polarization distributions. (b) Close-up view of a local vector state of the structured light field, in which the ellipticity ratio and polarization direction angle are defined as $a/b$ and $\psi$, respectively.

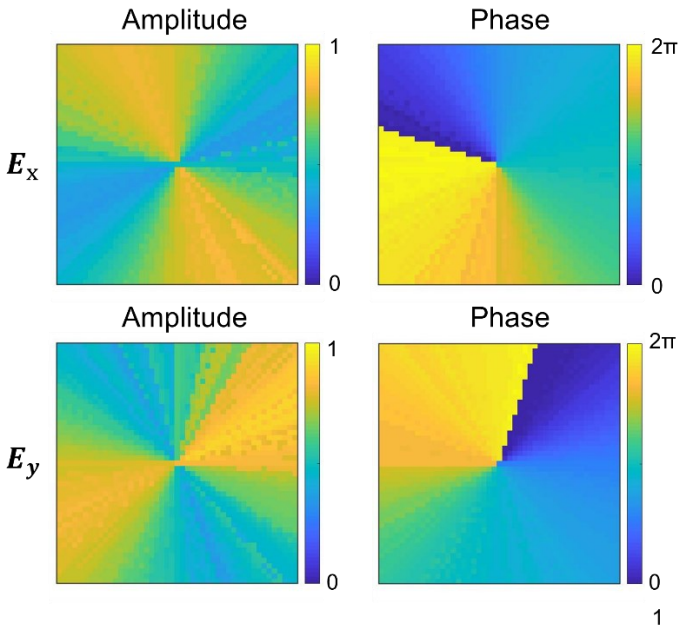


**Figure 5.17.: The amplitude and phase distributions of both polarization components, based on optical responses of selectively matched 3D meta-atoms.**

Based on the vector diffraction theory, we numerically simulated the diffraction pattern of the vector beam in the Fourier plane, where the polarization components along the x and y directions are shown in Figure 5.17.

We selected 3D nanopillars with matched optical responses based on Equation (5-6) to fulfill the desired amplitude and phase requirements. We also calculated the intensity response of our designed meta-atoms in the Fourier plane, which shows great agreement with our theoretical results. The resultant doughnut-shaped total intensity in the Fourier plane and the rotated two-lobe polarization patterns are consistent with our desired vector state (as shown in Figure 5.19). As such, the newly fabricated metafiber, SLGM-5 (Figure 5.18), was experimentally characterized by measuring the total intensity and polarization filtered images in the Fourier plane of the metafiber, finding a good agreement with our theoretical and simulation results.

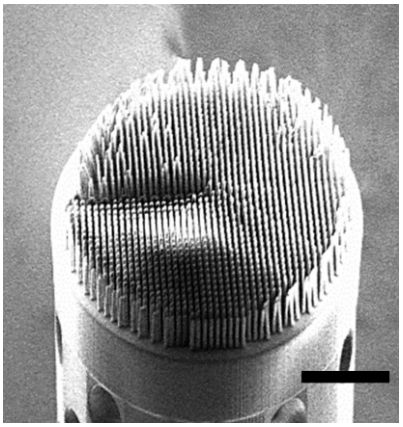

**Figure 5.18.: SEM image of SLGM-5.** (Scale bar: 30 μm.)

Our simulation and experimental results show a consistent divergence angle of 0.05° induced by the first-order OAM beam of the SLGM-5 output. As such, we have experimentally verified that our metafiber platform is able to transform an arbitrary structured light field directly on the end face of a PM-SMF.

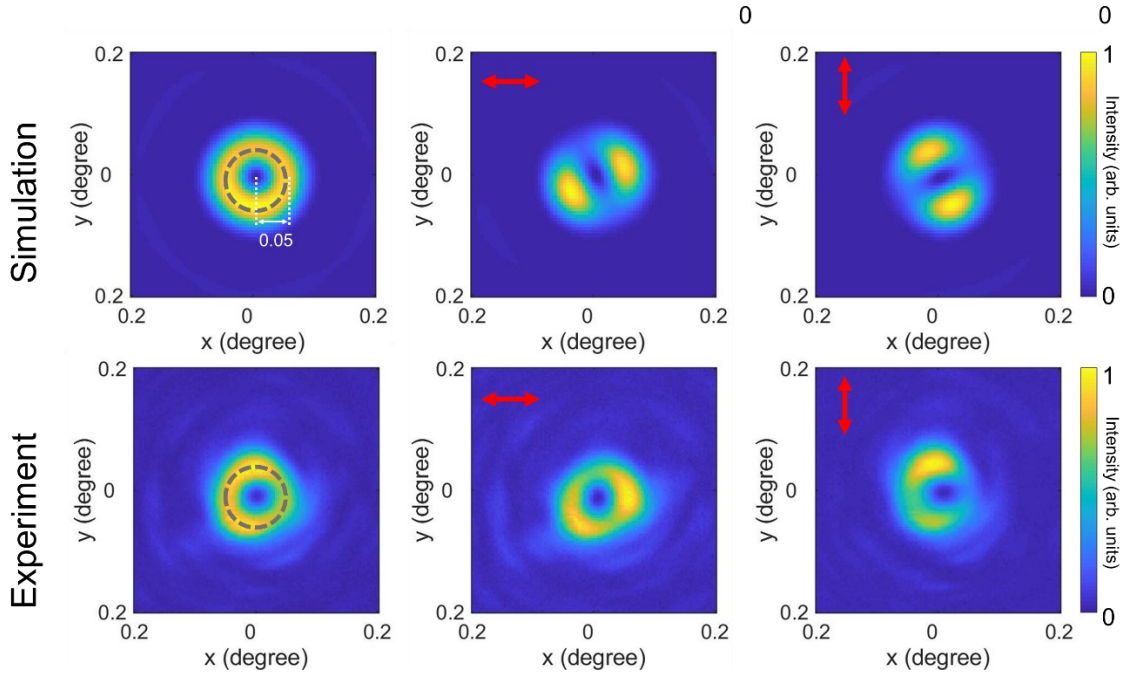


**Figure 5.19.: Simulation and experimentally measured intensity distributions of SLGM-5 in the Fourier plane.** Total intensity (first column) and polarization filtered intensity images (second and third columns, in which red arrows label the polarization axis of the linear polarizer). The dashed circles mark the beam divergence angle of 0.05 degrees.

## 5.5 Conclusion

We have demonstrated a novel metafiber platform that transforms the output of a single-mode fiber into arbitrarily structured light on the HOPS using nanoprinted metasurfaces. We successfully created polymeric 3D metasurfaces on commercial polarization-maintaining single-mode fibers. The additional height degree of freedom in 3D nanopillar meta-atoms significantly expands the 3D meta-atom library, enabling independent, complete, and precise control of polarization and phase at the level of individual meta-atoms. Several Structured Light-Generating Metafibers were designed, 3D laser nanoprinted, and characterized, facilitating the on-fiber realization of five representative structured-light fields on the HOPS. These include radial and azimuthal polarizations, circularly polarized vortex beams with different topological charges, and an arbitrary vector state from the HOPS with a spatially variant elliptical polarization distribution.

The implementation of structured light directly on optical fibers, owing to its simplicity and integration, presents a new paradigm for advancing optical fiber science and technology towards multimode light shaping and multi-dimensional light-matter interactions. For instance, long-distance transmission and delivery of structured light modes may no longer require

sophisticated multimode fibers, which typically suffer from intrinsic modal crosstalk and polarization mixing. Instead, our metafiber platform enables arbitrarily structured light transformation at the fiber end-faces, producing well-defined structured light modes of high quality that are resilient to bending and reproducible. Therefore, we believe that our demonstrated structured-light metafibers hold significant potential for various applications, including but not limited to fiber communications, fiber lasers, fiber sensors, endoscopic imaging, fiber lithography, and lab-on-fiber technology.

# 6. Polarimeter based on 3D metasurface

*This article is being prepared for submission.*

Polarization describes the direction of electromagnetic oscillation and, like phase and intensity, serves as a vital carrier of information. Notably, light reflected by various species and materials in nature exhibits distinct polarization characteristics, enabling the extraction of additional target information by detecting the polarization of light. Consequently, polarization detection is extensively employed in remote sensing[137], target recognition[138], and biological imaging [139]. However, current polarization detection systems are often large and complex, limiting their practical applications. In this chapter, we propose a 3D-printed metasurface with polarization detection capabilities. This metasurface can accurately obtain the polarization information of incident light with a single measurement. Furthermore, 3D nanoprinting technology endows the metasurface with excellent on-chip compatibility, paving the way for the miniaturization of polarization detection and imaging systems.

## 6.1 Introduction

In classical electromagnetics, light is a transverse wave, meaning the oscillation direction of the light field vector is perpendicular to the propagation direction of the light wave. Typically, within the vibration plane, the oscillation direction of the light field is asymmetric relative to the propagation direction, a property known as the polarization of light waves. This characteristic distinguishes transverse waves from longitudinal waves. Based on the shape of the projection of the vibration plane on the wavefront, polarization can be categorized into linear polarization, circular polarization, and elliptical polarization.

In 1941, Jones used vectors (column matrices) to represent the x and y components of the electric vector in order to describe the polarization state [140]:

$$\boldsymbol{E} = \begin{bmatrix} E_x \\ E_y \end{bmatrix}, \qquad (6-1)$$

where $E_x$, $E_y$ are the electric field vectors along the x and y axes respectively. The Jones vector represents the amplitude and phase of two orthogonal components of light at the same time and location, regardless of time. In addition, Jones also used a $2 \times 2$ matrix called the Jones matrix to describe the polarization conversion characteristics of optical components. For light with any polarization state, when it passes through multiple optical elements, the Jones vector of the outgoing light, that is, the polarization state, can be obtained by multiplying the Jones matrix of the element and the Jones vector of the incident light. This allows people to easily calculate the polarization state of light after passing through complex optical systems.

However, the Jones vector can only be used for fully polarized light and cannot describe complex polarization states. Therefore, in 1852, Stokes proposed using a matrix containing four parameters to represent the intensity and polarization state of light waves:

$$\boldsymbol{E} = \begin{bmatrix} S_0 \\ S_1 \\ S_2 \\ S_3 \end{bmatrix} = \begin{bmatrix} E_x^2 + E_y^2 \\ E_x^2 - E_y^2 \\ 2E_xE_ycos\delta \\ 2E_xE_ysin\delta \end{bmatrix} = \begin{bmatrix} I_x + I_y \\ I_x - I_y \\ I_{45°} - I_{-45°} \\ I_R - I_L \end{bmatrix} \quad (6-2)$$

where,$\delta$ represents the phase difference between the x and y components.

Among the Stokes parameters, the polarization of light can be completely expressed by four parameters from $S_0$ to $S_3$. The meanings represented by each parameter are:

- $S_0$ is the total light intensity. Usually expressed in unit 1, the other three values are normalized accordingly.
- $S_1$ represents the difference between horizontally polarized light intensity and vertically polarized light intensity. A value of +1 indicates that all light is horizontally polarized, and -1 indicates that all light is vertically polarized.
- $S_2$ represents the difference between +45° polarized light intensity and -45° polarized light intensity. A value of +1 indicates that all is +45° polarized light, and -1 indicates that all is -45° polarized light.
- $S_3$ represents the difference between the intensity of right-handed circularly polarized light and the intensity of left-handed circularly polarized light. A value of +1 indicates that all is right-handed circularly polarized light, and -1 indicates that all is left-handed circularly polarized light.

By measuring the intensities of these polarization states, we can determine the Stokes parameters and thus calculate the polarization of the light. The advantage of this method is its capability to represent not only fully polarized light but also partially polarized and natural (unpolarized) light.

Furthermore, the Poincaré sphere offers a more intuitive depiction of light's polarization state. Illustrated in Figure 6.1, the Poincaré sphere presents a geometric representation of light's polarization states. The sphere's radius denoted as $S_0$ symbolizes the total light intensity. Any point on the sphere can be characterized by the Stokes parameters $S_1$, $S_2$, $S_3$. Left-hand polarized light and right-hand polarized light occupy the south and north poles of the sphere, respectively, while linearly polarized light is situated along the equator. The remaining points on the sphere represent elliptically polarized states, with those in the upper hemisphere corresponding to right-handed elliptical polarization and those in the lower hemisphere representing left-handed elliptical polarization.

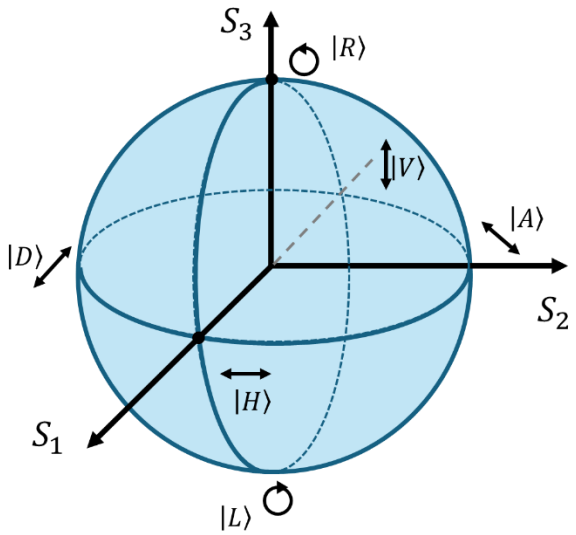


**Figure 6.1.: The Poincaré sphere used to represent polarization states of light.**

Since the polarization of the reflected or transmitted light of the object contains rich information that cannot be obtained from the intensity, so the polarization detection has important applications in the field of film thickness measurement, remote sensing, machine vision and so on. Traditional spatial light path measurement requires discrete optical components, which results in a complex system and requires multiple measurements. The metasurface has a unique polarization control capability and multi-functional integration capabilities, making it an attractive platform for polarization detection. And because of its features of ultra-light and ultra-compact, it is expected to achieve a more integrated optical system.

## 6.2 Theory

When light interacts with an object, its polarization state changes. Hans Mueller used a 4x4 matrix $\boldsymbol{M}$ containing 16 parameters to describe this polarization change relationship. This matrix, known as the Mueller matrix, is defined as[141]:

$$\boldsymbol{M} = \begin{bmatrix} m_{00} & m_{01} & m_{02} & m_{03} \\ m_{10} & m_{11} & m_{12} & m_{13} \\ m_{20} & m_{21} & m_{22} & m_{23} \\ m_{30} & m_{31} & m_{32} & m_3 \end{bmatrix} \qquad (6-3)$$

If the Stokes parameter of the incident light is $\boldsymbol{S_{in}}$, after interacting with the object, the Stokes parameter of the outgoing light is $\boldsymbol{S_{out}}$. This relationship between them can be described by:

$$\boldsymbol{S_{out} = MS_{in}} \qquad \boldsymbol{(6-4)}$$

To find the Stokes parameters of the incident light from the outgoing light, do matrix transformation:

$$\boldsymbol{S_{in} = M^{-1}S_{out}} \qquad \boldsymbol{(6-5)}$$

Where $\boldsymbol{M^{-1}}$ is the inverse matrix of the Mueller matrix of $\boldsymbol{M}$.

If the parameters of the outgoing light and the Mueller matrix of the object are known, the polarization state of the incident light can be determined through inversion. This principle forms the basis of the polarization detector we designed.

In actual measurements, only the intensity information of the emitted light ($S_0$) can be directly obtained. Since the Stokes parameters of the emitted light consist of four parameters, at least four measurements are required to acquire complete polarization information. This is also the reason why traditional polarization detection setup is bulky and complicated.

To simplify the design and reduce processing complexity, we selected a metasurface with wave plate functionality for polarization measurement. A fixed polarizer is placed on the backside of the metasurface to analyze the Stokes parameters of the outgoing light. We chose a configuration where complete polarization information can be obtained by rotating the wave plate and measuring the outgoing light intensity at four different angles (Figure 6.2).

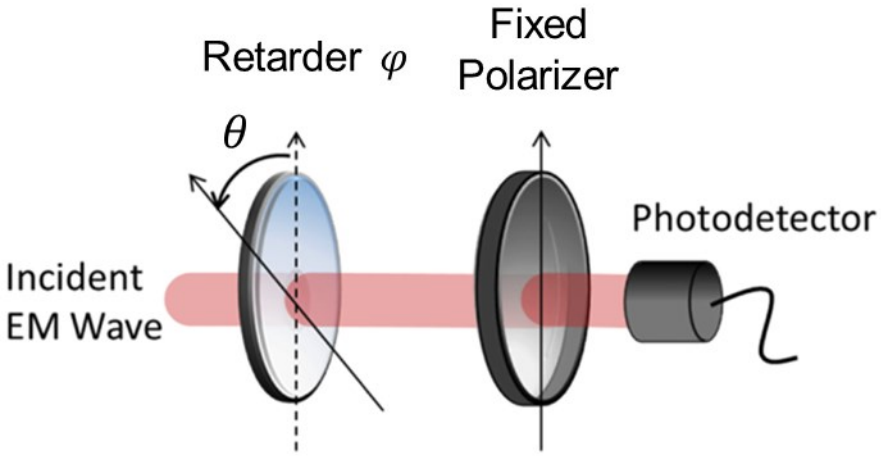


**Figure 6.2.: Schematic diagram of polarization detection system**

In our polarization detection system, the Mueller matrix of the metasurface is $\boldsymbol{M_j}$ ($j$=0, 1, 2, 3 represents the Mueller matrix at different rotation angles). The Mueller matrix of the analyzer is $M_{pol}$. For incident light with polarization $S_{in}$, the following relationship holds:

$$\boldsymbol{S_j = M_{pol} * M_j * S_{in}} \qquad (6-6)$$

In actual measurements, we cannot directly measure the Stokes parameters but can only measure the intensity of the emitted light. Therefore, we introduce the vector $\boldsymbol{I}$ representing the light intensity and the measurement matrix $\boldsymbol{W}$. The relationship between them is given by:

$$\boldsymbol{I = WS_{in}} \qquad (6-7)$$

The first term $S_0$ in $\boldsymbol{S_j}$ represents the light intensity. Thus, according to matrix operations, we have:

$$\boldsymbol{I_j = A_j S_{in}} \qquad (6-8)$$

Here $\boldsymbol{A_j}$ is the first projector of $\boldsymbol{M_{pol} * M_j}$. Obviously, there is:

$$\boldsymbol{W} = \begin{bmatrix} \boldsymbol{A_0} \\ \boldsymbol{A_1} \\ \boldsymbol{A_2} \\ \boldsymbol{A_3} \end{bmatrix} \tag{6-9}$$

From equation (6-7), we get:

$$\boldsymbol{S_{in}} = \boldsymbol{W^{-1}I} \tag{6-10}$$

This means that if the Mueller matrix is obtained for each measurement, the measurement matrix $\boldsymbol{W}$ can be calculated. The goal then becomes obtaining the Mueller matrix of the wave plate at different rotation angles.

For an arbitrary wave plate, its Jones matrix can be expressed as[142]:

$$\boldsymbol{E} = \begin{bmatrix} t_p e^{i\varphi_p} & 0 \\ 0 & t_s e^{i\varphi_s} \end{bmatrix} \tag{6-11}$$

Here $\mathrm{t_p}$ and $\mathrm{t_s}$ the amplitude of the electric field for parallel and perpendicular polarized light, respectively. $\varphi_p$ and $\varphi_s$ denote the phase shifts induced by the wave plate on the parallel and perpendicular components of light. Equation 6-11 can be reformulated in the representation of a Mueller matrix:

$$\boldsymbol{M_{wp}} = \begin{bmatrix} \frac{1}{2}\left(t_p{}^2 + t_s{}^2\right) & \frac{1}{2}\left(t_p{}^2 - t_s{}^2\right) & 0 & 0 \\ \frac{1}{2}\left(t_p{}^2 - t_s{}^2\right) & \frac{1}{2}\left(t_p{}^2 + t_s{}^2\right) & 0 & 0 \\ 0 & 0 & t_p t_s cos\left(\varphi_p - \varphi_s\right) & t_p t_s sin\left(\varphi_p - \varphi_s\right) \\ 0 & 0 & -t_p t_s sin\left(\varphi_p - \varphi_s\right) & t_p t_s cos\left(\varphi_p - \varphi_s\right) \end{bmatrix} \tag{6-12}$$

For waveplates incorporating rotation angles, it is necessary to introduce a rotation matrix:

$$\boldsymbol{M_R}(\theta) = \boldsymbol{M_R}(-2\theta) \cdot \boldsymbol{M_{wp}} \cdot \boldsymbol{M_R}(2\theta) \tag{6-13}$$

Where $\boldsymbol{M_R}$ represents the Mueller matrix of the optical element after rotating it by an angle $\theta$:

$$\boldsymbol{M_R}(\theta) = \begin{bmatrix} 1 & 0 & 0 & 0 \\ 0 & cos(2\theta) & sin(2\theta) & 0 \\ 0 & -sin(2\theta) & cos(2\theta) & 0 \\ 0 & 0 & 0 & 1 \end{bmatrix} \tag{6-14}$$

Hence, in the case of our metasurface wave plate, once the transmission and phase information are determined, it becomes feasible to compute the Mueller matrix at any given angle $\theta$.

## 6.3 Design

As in the previous chapter, we employ rectangular nanopillars as metasurfaces to function as wave plates (Figure 6.3). The RCWA method was utilized to simulate these nanopillars. In our simulations, we modeled 3D nanopillars with consistent parameters: a period (P) of 2 μm, lengths (L) ranging from 0.85 to 1.7 μm, heights (H) ranging from 6 to 10 μm, and in-plane aspect ratios (R) varying from 0.3 to 0.6. Since the relevant simulation data has been clearly displayed in previous chapters, we will not display and discuss it in detail here.

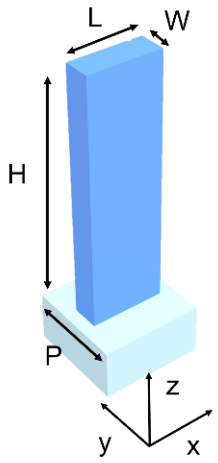


**Figure 6.3.: Schematic diagram of nanopillars.**

We introduce a parameter called Equally Weighted Variance (EWV) to represent the accuracy of polarization measurement. In our polarization measurement system, the results obtained are considered accurate when the EWV is below 15.

We chose nanopillars with two sets of parameters to realize the wave plate function. The first type of nanopillar has a length of 1600 nm, a width of 600 nm, and a height of 9.7 μm. Its phase difference between s and p modes is 110°, and it has different transmittances, thus it is termed the attenuating type (metasurface MS1). The second type of nanopillar has a length of 1625 nm, a width of 650 nm, and a height of 8.6 μm. It exhibits a phase difference of 130° between s and p polarizations and equal transmittance, thus it is termed the non-attenuating type (metasurface MS2).

## 6.4 Experiments and characterization

We use the method in Chapter 3 to process the wave plate metasurface. The metasurface was directly printed onto a glass substrate. Figure 6.4a and Figure 6.4b show SEM images of two metasurface samples, respectively.

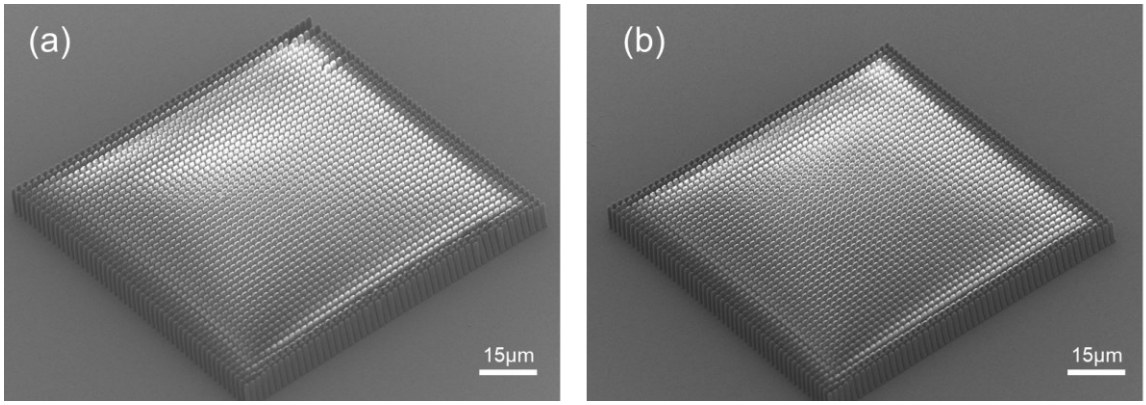


**Figure 6.4.: SEM image of nanoprinted attenuating metasurface (a) and non-attenuating metasurface (b).** (tilted view).

### Retardance calculation method

Although the SEM images show that the fabricated sample has an ideal size and good morphology, there will still be size discrepancies between the 3D nanoprinted samples and the designed samples. Therefore, further testing of the phase retardation and transmittance of the nanoprinted metasurface along the x and y axes is necessary.

We use the setup shown in Figure 6.5 to measure the transmission and phase retardation of the metasurface. A polarizer is placed in front of the metasurface, initially set at angles of 0° and 90° to measure the transmission along the metasurface. The signal is passed through a 10x microscope system and captured by a camera. The sample is moved in and out using the stage, and images are captured in both states. (Figure 6.6) By analyzing the intensity at the same position in the two images, the transmittance values for p and s polarizations of the attenuating sample were found to be 0.72 and 0.57, respectively. The polarizer was then set to +45° and -45°, and the light intensity was measured again. Through these measurements, the phase retardance of the attenuating sample was calculated to be 112.7°. The discrepancy from the theoretical phase delay is attributed to fabrication errors. Based on the measured transmittance and phase retardation, we determined that the four rotation angles of the metasurface that minimize the EWV, and thus the polarization measurement error, should be 53°, 15°, -15°, and -53°.

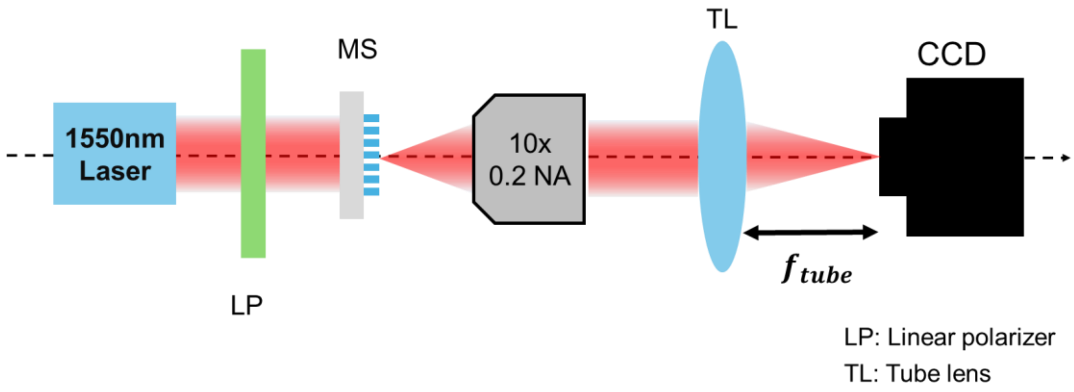


**Figure 6.5.: Optical setup diagram for measuring transmission in neutral line.**

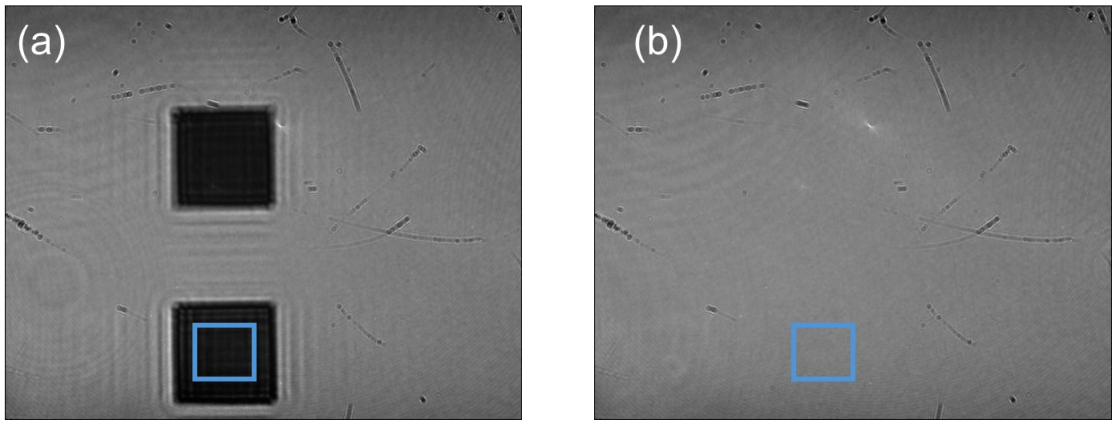


**Figure 6.6.: Raw data map detected by CCD.** (a) Image of the metasurface as it moves into the field of view. (b) Image of the metasurface as it moves out of the field of view. (The blue square is the area used to calculate transmission)

According to Equations (6-6) to (6-13), the Mueller matrix at four angles is obtained, and the first projector is taken to form the test matrix $\boldsymbol{W_{MS1}}$.

$$\boldsymbol{W_{MS1}} = \begin{bmatrix} 0.3122 & -0.1000 & -0.0821 & 0.2841 \\ 0.3550 & 0.2435 & 0.2119 & 0.1478 \\ 0.3550 & 0.2435 & -0.2119 & -0.1478 \\ 0.3122 & -0.1000 & 0.0821 & -0.2841 \end{bmatrix}$$

At this time, the theoretical EWV is 11, and the polarization state of the incident light can be accurately measured.

In the same way, we measured the phase retardation of the non-attenuated sample to be 132°, and the transmittance of p light and s-light in the neutral state to be 0.77 and 0.75, respectively. The four rotation angles for this sample are 52°, 15°, -15°, and -52°. Subsequently, the measurement matrix $\boldsymbol{W_{MS2}}$ of the non-attenuating sample can be calculated:

$$\boldsymbol{W_{MS2}} = \begin{bmatrix} 0.3788 & -0.2188 & -0.1441 & 0.2735 \\ 0.3843 & 0.2256 & 0.2774 & 0.1410 \\ 0.3843 & 0.2256 & -0.2774 & -0.1410 \\ 0.3788 & -0.2188 & 0.1441 & -0.2735 \end{bmatrix}$$

The theoretical EWV of the non-attenuating sample is 10, which means that the sample can accurately detect polarization.

**Measurement method**

It should be noted that in actual measurements, optical elements are not ideal devices and measurement errors can occur during the polarization measurement process. Therefore, in addition to using the theoretical calculation method, we also employ a predetermined polarized light incident polarization measurement system to obtain the measured measurement matrix $\boldsymbol{W}^*$. (Here we add * in the upper right corner of the measured measurement matrix to distinguish.)

From Equation (6-7), we know that if the Stokes parameters of the incident light and the

intensity of the outgoing light are known, the measured matrix $\boldsymbol{W}^*$ can be calculated as follows:

$$\boldsymbol{W}^* = \boldsymbol{I}/\boldsymbol{S_{in}} \qquad (6-14)$$

Since $\boldsymbol{W}^*$ is a 4x4 matrix, at least 16 measurements are needed to calculate $\boldsymbol{W}^*$. To simplify the calculations and reduce measurement errors, the polarization generation system is configured into six states: vertical (0°), horizontal (90°), +45°, -45°, left-handed, and right-handed polarized light. The generation of circularly polarized light is achieved by adding a quarter-wave plate after the polarizer.

Specific polarized light is then sequentially illuminated on the metasurface and analyzer (set at 0°) to obtain all necessary information (Figure 6.7). For each incident polarized light, four states can be achieved by rotating the metasurface, resulting in a total of 24 states (6x4) in the experiment. The incident light source is a laser with a wavelength of 1550 nm. The signal passing through the analyzer is magnified by a 10x microscope system and finally captured by an infrared camera.

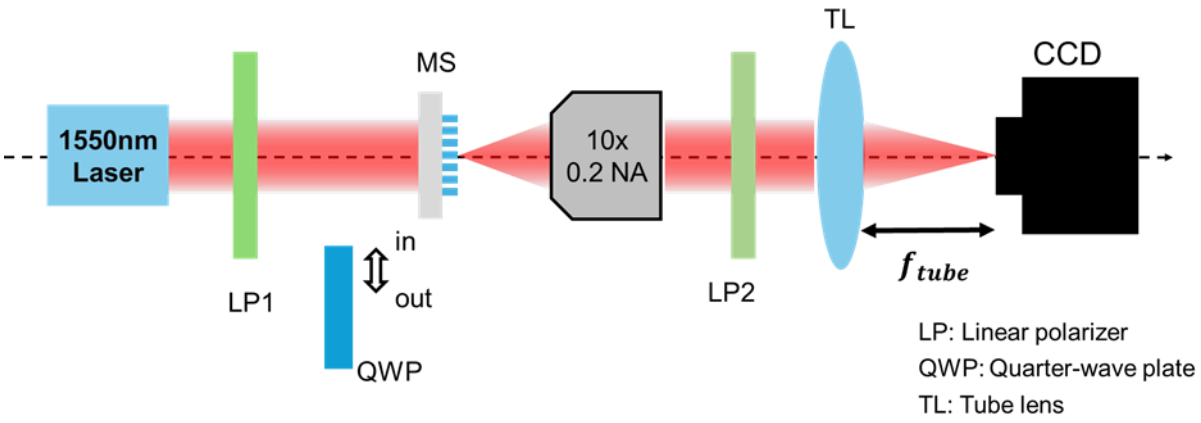


**Figure 6.7.: Diagram of the optical setup for measuring the measured matrix $\boldsymbol{W}^*$.**

To enhance the accuracy of the experiment, we conducted measurements with the metasurface, without the metasurface, and for background noise separately in each instance. The experimental results are presented in the form of a 6x4 matrix.

$$\boldsymbol{I} = \begin{bmatrix} 0.19 & 0.34 & 0.20 & 0.36 & 0.57 & 0.50 \\ 0.58 & 0.07 & 0.57 & 0.12 & 0.46 & 0.19 \\ 0.60 & 0.06 & 0.12 & 0.58 & 0.19 & 0.47 \\ 0.18 & 0.35 & 0.36 & 0.22 & 0.05 & 0.58 \end{bmatrix}$$

Perform simultaneous calculations on the matrix $\boldsymbol{I}$ to obtain the measurement matrix $\boldsymbol{W}^*_{\boldsymbol{MS1}}$:

$$\boldsymbol{W}^*_{\boldsymbol{MS1}} = \begin{bmatrix} 0.2852 & -0.0745 & -0.0802 & 0.2601 \\ 0.3309 & 0.2549 & 0.2251 & 0.1350 \\ 0.3343 & 0.2698 & -0.2299 & -0.1400 \\ 0.2907 & -0.0845 & 0.0697 & -0.2651 \end{bmatrix}$$

The EWV of the $\boldsymbol{W}^*_{\boldsymbol{MS1}}$ is 11.5.

In the same way, we can calculate the measurement matrix $\boldsymbol{W}^*_{\boldsymbol{MS2}}$ of the non-attenuation

sample as:

$$\boldsymbol{W^*}_{\boldsymbol{MS2}} = \begin{bmatrix} 0.3707 & -0.2048 & -0.1551 & 0.1500 \\ 0.3795 & 0.2299 & 0.2851 & 0.0750 \\ 0.3727 & 0.2398 & -0.2849 & -0.0800 \\ 0.3633 & -0.1998 & 0.1579 & -0.1400 \end{bmatrix}$$

The EWV of the $\boldsymbol{W^*}_{\boldsymbol{MS2}}$ is 17.5 (exceeding 15), which could lead to inaccurate measurement results. This discrepancy may be attributed to systematic errors within the measurement system.

**Polarization detection**

To verify that our metasurface can detect polarization, we randomly selected two unknown polarization states: one is linear polarization (unknown state 1), and the other is an arbitrary unknown polarization state (unknown state 2).

We first measure the polarization with MS1. The azimuth angle of linearly polarized light is 30°, so its Stokes parameter $\boldsymbol{S}$ is $[1 \quad 0.5000 \quad 0.8660 \quad 0]^T$. The optical setup of the experiment is shown in Figure 6.8. By rotating the metasurface, four measured intensities are obtained. According to Equation (6-7), the detected polarized light Stokes parameter $\boldsymbol{S} = [0.9204 \quad 0.5684 \quad 0.8679 \quad 0.0052]^{\mathrm{T}}$ can be calculated. The Stokes parameter calculated by measured matrix is $\boldsymbol{S}^* = [0.9698 \quad 0.5475 \quad 0.8530 \quad -0.0230]^{\mathrm{T}}$. The polarization detected by MS1 is plotted in Figure 6.9 left.

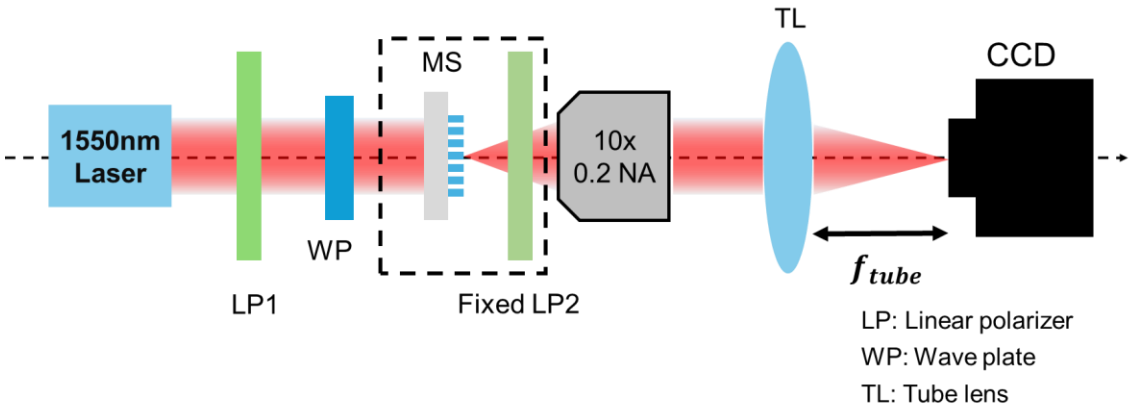


**Figure 6.8.: Diagram of the optical setup for polarization detection.**

For unknown state 2, the azimuth angle of the polarization is 19° and the ellipticity is 21.3°. Thus, the Stokes parameter of the incident light is $\boldsymbol{S} = [1 \quad 0.5799 \quad 0.4531 \quad 0.6770]^{\mathrm{T}}$. Using the same method, we calculate the detected polarization state based on the measured intensities $\boldsymbol{I}$ resulting in $\mathrm{S} = [0.9910 \quad 0.5888 \quad 0.4397 \quad 0.6211]^{\mathrm{T}}$. And the Stokes parameter calculated by the measured matrix is $\boldsymbol{S}^* = [1.0445 \quad 0.5702 \quad 0.4416 \quad 0.6595]^{\mathrm{T}}$. The polarization states are plotted in the right of Figure 6.9.

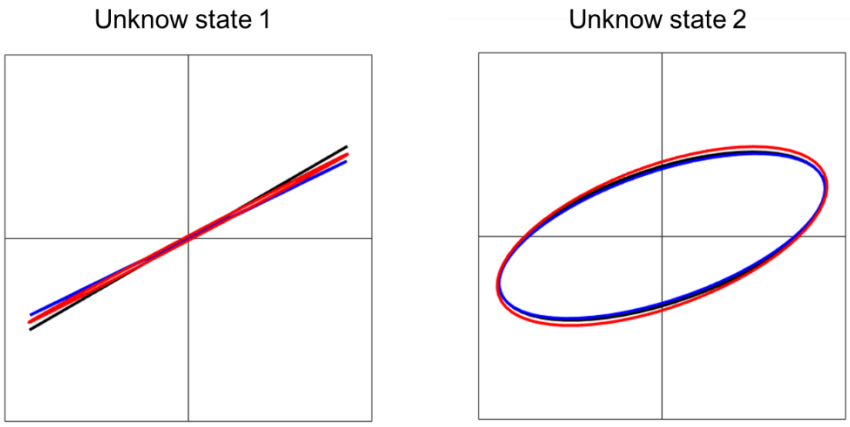


**Figure 6.9.: Polarization state detected by MS1.** Left: The polarization state measured by the attenuated sample. Right: The polarization state measured by the non-attenuated sample. (Black: theoretical polarization state. Blue: polarization state based on the calculated measurement matrix $\boldsymbol{W}$. Red: polarization state based on the calculated measurement matrix $\boldsymbol{W}^*$)

From Figure 6.9, we can see that for attenuated sample (MS1), both methods can accurately detect the polarization state of light.

Same measurements of two unknown polarization states were performed using the non-attenuating metasurface MS2. The polarization state of unknown state 1 is $S = [1.0133 \quad 0.5260 \quad 0.8636 \quad -0.0247]^T$ ($S = [1.0043 \quad 0.5275 \quad 0.8946 \quad -0.0221]^T$ the Stokes parameter calculated by the theoretical measurement matrix). The polarization state of unknown state 2 is $S = [0.9734 \quad 0.6182 \quad 0.4555 \quad 0.6450]^T$ ($S = [0.9708 \quad 0.6066 \quad 0.4753 \quad 0.3418]^T$ the Stokes parameter calculated by the theoretical measurement matrix). The detected polarization states are plotted in Figure 6.10

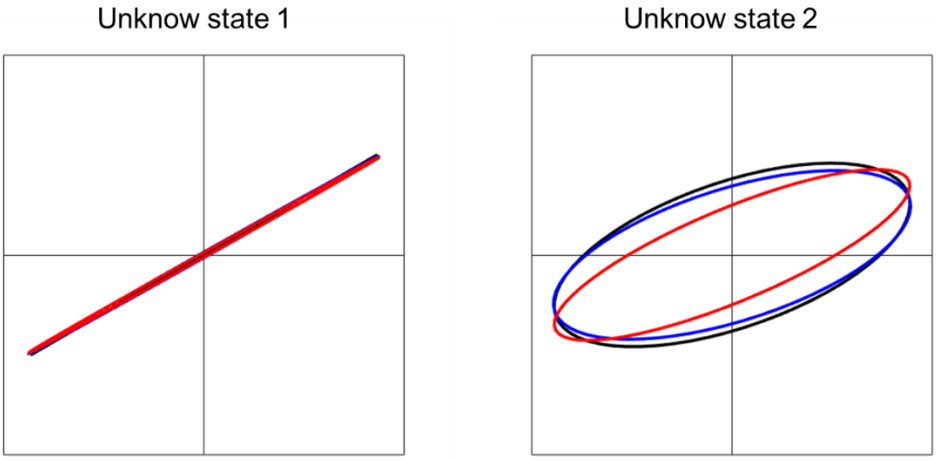


**Figure 6.10.: Polarization state detected by MS2.** Left: The polarization state measured by the attenuated sample. Right: The polarization state measured by the non-attenuated sample. (Black: theoretical polarization state. Blue: polarization state based on the calculated measurement matrix $\boldsymbol{W}$. Red: polarization state based on the calculated measurement matrix $\boldsymbol{W}^*$)

The results in Figure 6.10 show that when measuring the elliptical polarization state of the non-attenuating sample (MS2), the results based on the measurement method are accurate, while the polarization state detected by the delay calculation method is less accurate. This result is mainly caused by the system's inaccuracy when measuring ellipsometry, which may be due to intrinsic and measurement errors in the optical components of the measurement system.

In order to observe the performance of the polarimeter more intuitively, we plot the polarization states of the incident light and detection light on the Poincaré sphere (Figure 6.11) In this figure, the black circle represents the theoretical polarization state to be measured, the red box indicates the polarization state measured using the delay calculation method (matrix $\boldsymbol{W}$), and the blue star denotes the polarization state detected using the measurement method $\boldsymbol{W}^*$.

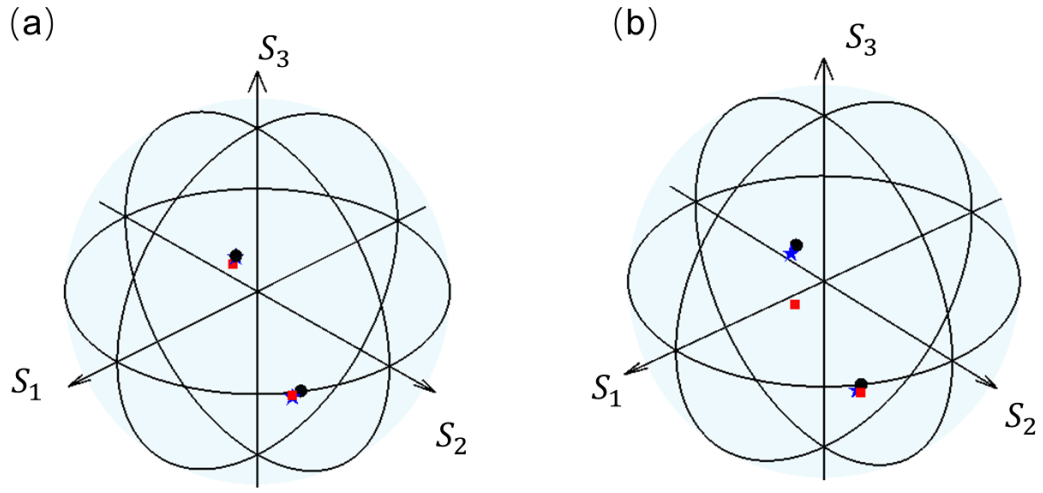


**Figure 6.11.: Poincaré sphere describing polarization detection.** (a) The polarization state measured by the attenuated sample (b) The polarization state measured by the non-attenuated sample. (The black circle in the figure represents the theoretical polarization state of the polarization to be measured, the red box represents the polarization state detected by $\boldsymbol{W}$ based on delay calculation, and the blue star represents the polarization state detected by $\boldsymbol{W}^*$ based on the measurement method)

## 6.5 Conclusion

In this chapter, we propose a polarization detection method based on nanoprinted metasurfaces. The detection system includes a metasurface with wave plate functionality and a fixed polarizer. By rotating the wave plate to different angles, we can determine the polarization state of light in a single measurement. It should be noted that in this chapter, we focus on experimentally verifying the working principle of the polarization detection system. Therefore, in our experiment, we chose to rotate the metasurface rather than directly printing wave plates with different rotation angles. Further in-depth research is required to refine this approach. Our experimental results accurately detected two unknown polarized lights (linear and elliptical polarization), demonstrating the superior capabilities of our polarization detection system. We believe that, given the excellent substrate compatibility of laser direct writing technology,

nanoprinted polarizers can be directly printed on cameras, offering a novel solution for the miniaturization of polarization detectors.

# 7. Conclusions and outlook

This dissertation primarily explores the theory and principles of 3D nanoprinted metasurfaces based on laser direct writing technology, focusing on their light control capabilities and potential applications. The introduction of the height degree of freedom endows 3D nanoprinted metasurfaces with superior optical properties. Furthermore, these metasurfaces can be seamlessly integrated with optical fibers to create a super optical fiber platform capable of arbitrarily controlling light output, offering broad application prospects in endoscopic imaging, optical fiber communications, and photonic chips.

This dissertation covers the principles of dispersion engineering, phase, and polarization control of 3D metasurfaces and demonstrates three experimental projects:

**Dispersion control of 3D metasurfaces**: We demonstrate an achromatic metafiber that can be used for focusing and imaging across the entire telecommunications range. This super optical fiber exhibits superior dispersion control capabilities and achieves efficient focusing and imaging at the diffraction limit across the entire communication band. Additionally, by fixing the in-plane rotation angles of nanopillar atoms at 0 and 90 degrees, our 3D achromatic metalens demonstrates insensitivity to the polarization of incident light.

**Dispersion and polarization control of 3D metasurfaces**: We introduce a metafiber platform capable of generating arbitrary structured light. The additional height degree of freedom in the 3D nanopillar meta-atoms significantly expands the 3D meta-atom library, enabling independent, complete, and precise control of polarization and phase at the single meta-atom level. Several structured light-generating metafibers were designed, 3D laser nanoprinted, and characterized, facilitating the on-fiber realization of five representative structured light fields on higher-order Poincaré spheres.

**Polarization detection based on 3D metasurface**: We designed a polarization detection system based on metasurfaces and experimentally achieved accurate polarization measurement. By simply rotating the wave plate to different angles, the polarization state of light can be determined in a single measurement, greatly simplifying the process of polarization measurement.

The experimental results demonstrate that laser direct writing technology has significant potential in the fabrication of advanced optical devices. In particular, the integration with fiber optics creates a novel super-fiber platform capable of directly controlling the light emitted from the fiber, providing strong support and innovative ideas for the miniaturization and integration of optical devices. Additionally, 3D metasurfaces, with their additional height degree of freedom compared to 2D metasurfaces, greatly enhance the performance of metasurfaces.

# Publication list

[1] Metafiber transforming arbitrarily structured light. **Chenhao Li**, Torsten Wieduwilt, Fedja J Wendisch, Andrés Márquez, Leonardo de S Menezes, Stefan A Maier, Markus A Schmidt, Haoran Ren. *Nature Communications* 14, 7222 (2023).

[2] An achromatic metafiber for focusing and imaging across the entire telecommunication range. Haoran Ren, Jaehyuck Jang, **Chenhao Li** (contribution equally), Andreas Aigner, Malte Plidschun, Jisoo Kim, Junsuk Rho, Markus A. Schmidt and Stefan A. Maier. *Nature Communications* 13, 4183 (2022). (Highly Cited Paper)

[3] Optical vortices in nanophotonics. **Chenhao Li**, Maier Stefan A., Haoran Ren.. *Chinese Optics*, 2021, 14(4): 792-811.

[4] Orbital-Angular-Momentum-Controlled Hybrid Nanowire Circuit. Haoran Ren, Xiaoxia Wang, **Chenhao Li**, Chenglin He, Yixiong Wang, Anlian Pan, and Stefan A. Maier. *Nano Letters* 2021 21 (14), 6220-6227.

[5] A metasurface measuring twisted light in turbulence. Dinter Thomas; **Li, Chenhao**; Kühner Lucca; Weber Thomas; Tittl Andreas; Maier Stefan; Dawes Judith; Ren Haoran. *ACS Photonics*. 2022, 9, 9, 3043–305

[6] Dispersion engineering of metalenses. Haoyi Yu, Zhaoyang Xie, **Chenhao Li**, Chi Li, Leonardo de S. Menezes, Stefan A. Maier, Haoran Ren; *Appl. Phys. Lett*. 11 December 2023; 123 (24): 240503.

# Publisher Permissions

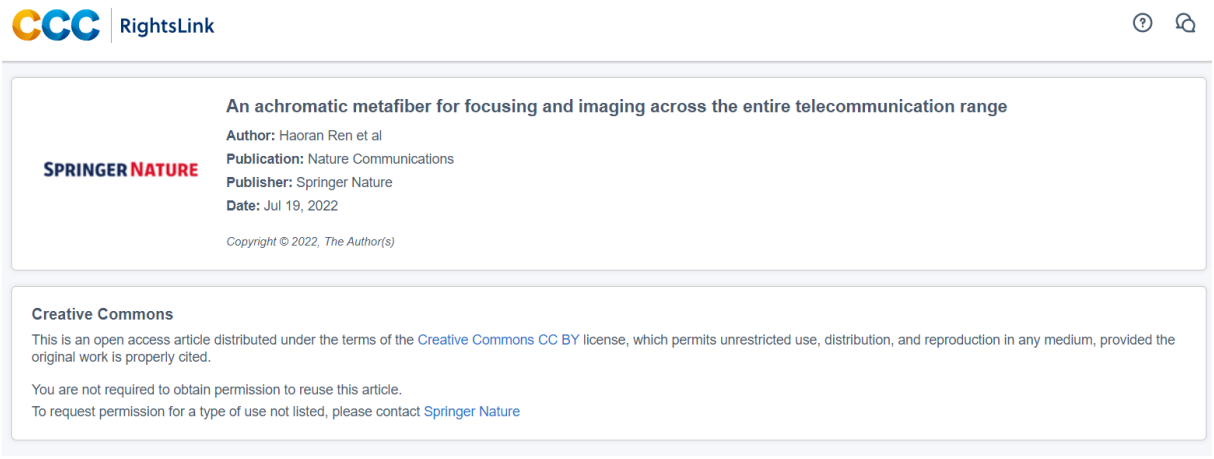

CCC RightsLink

SPRINGER NATURE

An achromatic metafiber for focusing and imaging across the entire telecommunication range

**Author:** Haoran Ren et al
**Publication:** Nature Communications
**Publisher:** Springer Nature
**Date:** Jul 19, 2022

*Copyright © 2022, The Author(s)*

**Creative Commons**

This is an open access article distributed under the terms of the Creative Commons CC BY license, which permits unrestricted use, distribution, and reproduction in any medium, provided the original work is properly cited.

You are not required to obtain permission to reuse this article.
To request permission for a type of use not listed, please contact Springer Nature

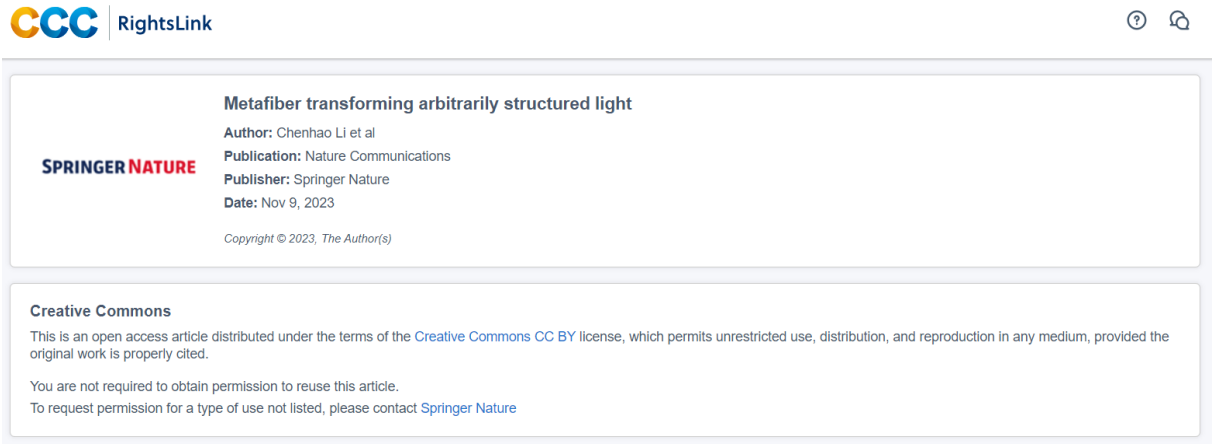

RightsLink

SPRINGER NATURE

**Metafiber transforming arbitrarily structured light**

**Author:** Chenhao Li et al
**Publication:** Nature Communications
**Publisher:** Springer Nature
**Date:** Nov 9, 2023

# Bibliography


1. V. G. Veselago, The Electrodynamics of Substances with Simultaneously Negative Values of ε and μ. *Soviet Physics Uspekhi* **10**, 509-514 (1968).
2. J. Lu *et al.*, Cerenkov radiation in materials with negative permittivity and permeability. *Opt Express* **11**, 723-734 (2003).
3. R. A. Shelby, D. R. Smith, S. Schultz, Experimental verification of a negative index of refraction. *Science* **292**, 77-79 (2001).
4. J. Chen *et al.*, Observation of the inverse Doppler effect in negative-index materials at optical frequencies. *Nature Photonics* **5**, 239-242 (2011).
5. C. M. Park, J. J. Park, S. H. Lee, Y. M. Seo, C. K. Kim, S. H. Lee, Amplification of acoustic evanescent waves using metamaterial slabs. *Phys Rev Lett* **107**, 194301 (2011).
6. J. B. Pendry, Negative refraction makes a perfect lens. *Phys Rev Lett* **85**, 3966-3969 (2000).
7. J. B. Pendry, A. J. Holden, W. J. Stewart, I. I. Youngs, Extremely low frequency plasmons in metallic mesostructures. *Phys Rev Lett* **76**, 4773-4776 (1996).
8. J. B. Pendry, A. J. Holden, D. J. Robbins, W. J. Stewart, Low frequency plasmons in thin-wire structures. *Journal of Physics: Condensed Matter* **10**, 4785-4809 (1998).
9. R. M. Walser, A. Lakhtakia, W. S. Weiglhofer, I. J. Hodgkinson, paper presented at the Complex Mediums II: Beyond Linear Isotropic Dielectrics, 2001.
10. D. Schurig *et al.*, Metamaterial electromagnetic cloak at microwave frequencies. *Science* **314**, 977-980 (2006).
11. J. B. Pendry, D. Schurig, D. R. Smith, Controlling electromagnetic fields. *Science* **312**, 1780-1782 (2006).
12. N. Fang, H. Lee, C. Sun, X. Zhang, Sub-diffraction-limited optical imaging with a silver superlens. *Science* **308**, 534-537 (2005).
13. Q. Cheng, T. J. Cui, W. X. Jiang, B. G. Cai, An omnidirectional electromagnetic absorber made of metamaterials. *New Journal of Physics* **12**, (2010).
14. R. Liu, C. Ji, J. J. Mock, J. Y. Chin, T. J. Cui, D. R. Smith, Broadband ground-plane cloak. *Science* **323**, 366-369 (2009).
15. N. Yu *et al.*, Light propagation with phase discontinuities: generalized laws of reflection and refraction. *Science* **334**, 333-337 (2011).
16. X. Ni, S. Ishii, A. V. Kildishev, V. M. Shalaev, Ultra-thin, planar, Babinet-inverted plasmonic metalenses. *Light: Science & Applications* **2**, e72-e72 (2013).
17. A. Pors, S. I. Bozhevolnyi, Plasmonic metasurfaces for efficient phase control in reflection. *Opt Express* **21**, 27438-27451 (2013).
18. C. Zhang *et al.*, Low-loss metasurface optics down to the deep ultraviolet region. *Light Sci Appl* **9**, 55 (2020).
19. H. Liang *et al.*, Ultrahigh Numerical Aperture Metalens at Visible Wavelengths. *Nano Lett* **18**, 4460-4466 (2018).
20. A. Arbabi, Y. Horie, A. J. Ball, M. Bagheri, A. Faraon, Subwavelength-thick lenses with high numerical apertures and large efficiency based on high-contrast transmitarrays. *Nat*

*Commun* **6**, 7069 (2015).
21. H. Zuo *et al.*, High-Efficiency All-Dielectric Metalenses for Mid-Infrared Imaging. *Advanced Optical Materials* **5**, (2017).
22. R. C. Devlin, M. Khorasaninejad, W. T. Chen, J. Oh, F. Capasso, Broadband high-efficiency dielectric metasurfaces for the visible spectrum. *Proc Natl Acad Sci U S A* **113**, 10473-10478 (2016).
23. M. V. Berry, Quantal Phase Factors Accompanying Adiabatic Changes. *Proceedings of the Royal Society of London. Series A, Mathematical and Physical Sciences* **392**, 45–57 (1984).
24. S. Pancharatnam, Generalized theory of interference, and its applications. *Proceedings of the Indian Academy of Sciences - Section A* **44**, 247-262 (1956).
25. S. Colburn, A. Zhan, A. Majumdar, Metasurface optics for full-color computational imaging. *Sci Adv* **4**, eaar2114 (2018).
26. P. R. West *et al.*, All-dielectric subwavelength metasurface focusing lens. *Opt Express* **22**, 26212-26221 (2014).
27. D. Fattal, J. Li, Z. Peng, M. Fiorentino, R. G. Beausoleil, Flat dielectric grating reflectors with focusing abilities. *Nature Photonics* **4**, 466-470 (2010).
28. X. Ni, A. V. Kildishev, V. M. Shalaev, Metasurface holograms for visible light. *Nature Communications* **4**, (2013).
29. G. Zheng, H. Muhlenbernd, M. Kenney, G. Li, T. Zentgraf, S. Zhang, Metasurface holograms reaching 80% efficiency. *Nat Nanotechnol* **10**, 308-312 (2015).
30. A. C. Overvig *et al.*, Dielectric metasurfaces for complete and independent control of the optical amplitude and phase. *Light Sci Appl* **8**, 92 (2019).
31. Y. Yang *et al.*, Full-Polarization 3D Metasurface Cloak with Preserved Amplitude and Phase. *Adv Mater* **28**, 6866-6871 (2016).
32. H. X. Xu *et al.*, Polarization-insensitive 3D conformal-skin metasurface cloak. *Light Sci Appl* **10**, 75 (2021).
33. D. L. Sounas, R. Fleury, A. Alù, Unidirectional Cloaking Based on Metasurfaces with Balanced Loss and Gain. *Physical Review Applied* **4**, (2015).
34. S. Chen, W. Liu, Z. Li, H. Cheng, J. Tian, Metasurface-Empowered Optical Multiplexing and Multifunction. *Adv Mater* **32**, e1805912 (2020).
35. T. J. Cui, M. Q. Qi, X. Wan, J. Zhao, Q. Cheng, Coding metamaterials, digital metamaterials and programmable metamaterials. *Light: Science & Applications* **3**, e218-e218 (2014).
36. T. J. Cui, S. Liu, L. L. Li, Information entropy of coding metasurface. *Light Sci Appl* **5**, e16172 (2016).
37. H. Wu *et al.*, Controlling Energy Radiations of Electromagnetic Waves via Frequency Coding Metamaterials. *Adv Sci (Weinh)* **4**, 1700098 (2017).
38. S. Wang *et al.*, Arbitrary polarization conversion dichroism metasurfaces for all-in-one full Poincare sphere polarizers. *Light Sci Appl* **10**, 24 (2021).
39. M. Liu *et al.*, Broadband generation of perfect Poincare beams via dielectric spin-multiplexed metasurface. *Nat Commun* **12**, 2230 (2021).
40. C. W. Qiu, T. Zhang, G. Hu, Y. Kivshar, Quo Vadis, Metasurfaces? *Nano Lett* **21**, 5461-5474 (2021).

41. A. S. Solntsev, G. S. Agarwal, Y. S. Kivshar, Metasurfaces for quantum photonics. *Nature Photonics* **15**, 327-336 (2021).
42. P. K. Jha, N. Shitrit, J. Kim, X. Ren, Y. Wang, X. Zhang, Metasurface-Mediated Quantum Entanglement. *ACS Photonics* **5**, 971-976 (2017).
43. X. Chen *et al.*, Dual-polarity plasmonic metalens for visible light. *Nat Commun* **3**, 1198 (2012).
44. W. Wang *et al.*, Ultra-thin, planar, broadband, dual-polarity plasmonic metalens. *Photonics Research* **3**, (2015).
45. D. Lin, P. Fan, E. Hasman, M. L. Brongersma, Dielectric gradient metasurface optical elements. *Science* **345**, 298-302 (2014).
46. M. Khorasaninejad, W. T. Chen, R. C. Devlin, J. Oh, A. Y. Zhu, F. Capasso, Metalenses at visible wavelengths: Diffraction-limited focusing and subwavelength resolution imaging. *Science* **352**, 1190-1194 (2016).
47. S. Wang *et al.*, Broadband achromatic optical metasurface devices. *Nat Commun* **8**, 187 (2017).
48. S. Wang *et al.*, A broadband achromatic metalens in the visible. *Nat Nanotechnol* **13**, 227-232 (2018).
49. W. T. Chen *et al.*, A broadband achromatic metalens for focusing and imaging in the visible. *Nat Nanotechnol* **13**, 220-226 (2018).
50. J. Chen *et al.*, Planar wide-angle-imaging camera enabled by metalens array. *Optica* **9**, (2022).
51. J. S. Park *et al.*, All-Glass 100 mm Diameter Visible Metalens for Imaging the Cosmos. *ACS Nano* **18**, 3187-3198 (2024).
52. Z. Li *et al.*, Meta-optics achieves RGB-achromatic focusing for virtual reality. *Sci Adv* **7**, (2021).
53. L. Allen, M. W. Beijersbergen, R. J. Spreeuw, J. P. Woerdman, Orbital angular momentum of light and the transformation of Laguerre-Gaussian laser modes. *Phys Rev A* **45**, 8185-8189 (1992).
54. A. Sit *et al.*, High-dimensional intracity quantum cryptography with structured photons. *Optica* **4**, (2017).
55. E. Nagali *et al.*, Optimal quantum cloning of orbital angular momentum photon qubits through Hong–Ou–Mandel coalescence. *Nature Photonics* **3**, 720-723 (2009).
56. G. Gibson *et al.*, Free-space information transfer using light beams carrying orbital angular momentum. *Opt Express* **12**, 5448-5456 (2004).
57. N. R. Heckenberg, R. McDuff, C. P. Smith, A. G. White, Generation of optical phase singularities by computer-generated holograms. *Opt Lett* **17**, 221 (1992).
58. M. W. Beijersbergen, R. P. C. Coerwinkel, M. Kristensen, J. P. Woerdman, Helical-wavefront laser beams produced with a spiral phaseplate. *Optics Communications* **112**, 321-327 (1994).
59. E. Karimi, S. A. Schulz, I. De Leon, H. Qassim, J. Upham, R. W. Boyd, Generating optical orbital angular momentum at visible wavelengths using a plasmonic metasurface. *Light: Science & Applications* **3**, e167-e167 (2014).
60. R. C. Devlin, A. Ambrosio, N. A. Rubin, J. P. B. Mueller, F. Capasso, Arbitrary spin-to-orbital angular momentum conversion of light. *Science* **358**, 896-901 (2017).

61. S. Wei, Z. Yang, M. Zhao, Design of ultracompact polarimeters based on dielectric metasurfaces. *Opt Lett* **42**, 1580-1583 (2017).
62. Z. Yang *et al.*, Generalized Hartmann-Shack array of dielectric metalens sub-arrays for polarimetric beam profiling. *Nat Commun* **9**, 4607 (2018).
63. N. A. Rubin, G. D'Aversa, P. Chevalier, Z. Shi, W. T. Chen, F. Capasso, Matrix Fourier optics enables a compact full-Stokes polarization camera. *Science* **365**, (2019).
64. S. Maruo, O. Nakamura, S. Kawata, Three-dimensional microfabrication with two-photon-absorbed photopolymerization. *Opt Lett* **22**, 132-134 (1997).
65. S. Kawata, H. B. Sun, T. Tanaka, K. Takada, Finer features for functional microdevices. *Nature* **412**, 697-698 (2001).
66. J. R. Tumbleston *et al.*, Additive manufacturing. Continuous liquid interface production of 3D objects. *Science* **347**, 1349-1352 (2015).
67. S. W. Hell, J. Wichmann, Breaking the diffraction resolution limit by stimulated emission: stimulated-emission-depletion fluorescence microscopy. *Opt Lett* **19**, 780-782 (1994).
68. Z. Gan, Y. Cao, R. A. Evans, M. Gu, Three-dimensional deep sub-diffraction optical beam lithography with 9 nm feature size. *Nat Commun* **4**, 2061 (2013).
69. I. Sakellari *et al.*, Diffusion-assisted high-resolution direct femtosecond laser writing. *ACS Nano* **6**, 2302-2311 (2012).
70. Q. Geng, D. Wang, P. Chen, S. C. Chen, Ultrafast multi-focus 3-D nano-fabrication based on two-photon polymerization. *Nat Commun* **10**, 2179 (2019).
71. P. Somers, Z. Liang, J. E. Johnson, B. W. Boudouris, L. Pan, X. Xu, Rapid, continuous projection multi-photon 3D printing enabled by spatiotemporal focusing of femtosecond pulses. *Light Sci Appl* **10**, 199 (2021).
72. M. Regehly *et al.*, Xolography for linear volumetric 3D printing. *Nature* **588**, 620-624 (2020).
73. M. S. Rill *et al.*, Photonic metamaterials by direct laser writing and silver chemical vapour deposition. *Nat Mater* **7**, 543-546 (2008).
74. T. Buckmann *et al.*, Tailored 3D mechanical metamaterials made by dip-in direct-laser-writing optical lithography. *Adv Mater* **24**, 2710-2714 (2012).
75. U. Klotzbach *et al.*, paper presented at the Laser-based Micro- and Nanoprocessing X, 2016.
76. S. Galanopoulos *et al.*, Design, Fabrication and Computational Characterization of a 3D Micro-Valve Built by Multi-Photon Polymerization. *Micromachines* **5**, 505-514 (2014).
77. D. J. Odde, M. J. Renn, Laser-guided direct writing of living cells. *Biotechnology and Bioengineering* **67**, 312-318 (2000).
78. N. R. Schiele, D. T. Corr, Y. Huang, N. A. Raof, Y. Xie, D. B. Chrisey, Laser-based direct-write techniques for cell printing. *Biofabrication* **2**, 032001 (2010).
79. Y. Nahmias, R. E. Schwartz, C. M. Verfaillie, D. J. Odde, Laser-guided direct writing for three-dimensional tissue engineering. *Biotechnol Bioeng* **92**, 129-136 (2005).
80. J. K. Gansel *et al.*, Gold helix photonic metamaterial as broadband circular polarizer. *Science* **325**, 1513-1515 (2009).
81. H. Ren, X. Fang, J. Jang, J. Burger, J. Rho, S. A. Maier, Complex-amplitude metasurface-based orbital angular momentum holography in momentum space. *Nat*

*Nanotechnol* **15**, 948-955 (2020).
82. C. F. Pan *et al.*, 3D-printed multilayer structures for high-numerical aperture achromatic metalenses. *Sci Adv* **9**, eadj9262 (2023).
83. T. Gissibl, S. Thiele, A. Herkommer, H. Giessen, Two-photon direct laser writing of ultracompact multi-lens objectives. *Nature Photonics* **10**, 554-560 (2016).
84. M. Plidschun, H. Ren, J. Kim, R. Forster, S. A. Maier, M. A. Schmidt, Ultrahigh numerical aperture meta-fibre for flexible optical trapping. *Light Sci Appl* **10**, 57 (2021).
85. C. F. Bohren, D. R. Huffman, *Absorption and Scattering of Light by Small Particles*. (1998).
86. J. B. Schneider, *Understanding the finite-difference time-domain method*. (chool of electrical engineering and computer science Washington State University, 2010).
87. M. G. Moharam, T. K. Gaylord, Rigorous coupled-wave analysis of planar-grating diffraction. *Journal of the Optical Society of America* **71**, (1981).
88. M. G. Moharam, T. K. Gaylord, E. B. Grann, D. A. Pommet, Formulation for stable and efficient implementation of the rigorous coupled-wave analysis of binary gratings. *Journal of the Optical Society of America A* **12**, (1995).
89. E. A. J. Marcatili, Dielectric Rectangular Waveguide and Directional Coupler for Integrated Optics. *Bell System Technical Journal* **48**, 2071-2102 (1969).
90. Y. Kane, Numerical solution of initial boundary value problems involving maxwell's equations in isotropic media. *IEEE Transactions on Antennas and Propagation* **14**, 302-307 (1966).
91. M. G. Moharam, T. K. Gaylord, Diffraction analysis of dielectric surface-relief gratings. *Journal of the Optical Society of America* **72**, (1982).
92. T. K. Gaylord, M. G. Moharam, Analysis and applications of optical diffraction by gratings. *Proceedings of the IEEE* **73**, 894-937 (1985).
93. H. Ren *et al.*, An achromatic metafiber for focusing and imaging across the entire telecommunication range. *Nat Commun* **13**, 4183 (2022).
94. A. M. Hanninen, E. O. Potma, Nonlinear optical microscopy with achromatic lenses extending from the visible to the mid-infrared. *APL Photonics* **4**, (2019).
95. X. Li, Y. Cao, N. Tian, L. Fu, M. Gu, Multifocal optical nanoscopy for big data recording at 30 TB capacity and gigabits/second data rate. *Optica* **2**, (2015).
96. S. J. M., *Optical Fiber Communications: Principles and Practice*. (Pearson Education, 2009).
97. J. Roh *et al.*, Full-color holographic projection display system featuring an achromatic Fourier filter. *Opt Express* **25**, 14774-14782 (2017).
98. T. Brabec, F. Krausz, Intense few-cycle laser fields: Frontiers of nonlinear optics. *Reviews of Modern Physics* **72**, 545-591 (2000).
99. X. Fang, H. Ren, M. Gu, Orbital angular momentum holography for high-security encryption. *Nature Photonics* **14**, 102-108 (2019).
100. B. Wang *et al.*, Visible-Frequency Dielectric Metasurfaces for Multiwavelength Achromatic and Highly Dispersive Holograms. *Nano Lett* **16**, 5235-5240 (2016).
101. P.-Y. Chen, A. Alù, Mantle cloaking using thin patterned metasurfaces. *Physical Review B* **84**, (2011).
102. X. Ma *et al.*, A planar chiral meta-surface for optical vortex generation and focusing.

*Sci Rep* **5**, 10365 (2015).

103. S. A. Kuznetsov, A. G. Paulish, M. Navarro-Cia, A. V. Arzhannikov, Selective Pyroelectric Detection of Millimetre Waves Using Ultra-Thin Metasurface Absorbers. *Sci Rep* **6**, 21079 (2016).
104. P. Georgi *et al.*, Metasurface interferometry toward quantum sensors. *Light Sci Appl* **8**, 70 (2019).
105. A. A. Fathnan, D. A. Powell, Bandwidth and size limits of achromatic printed-circuit metasurfaces. *Opt Express* **26**, 29440-29450 (2018).
106. C. Li *et al.*, Metafiber transforming arbitrarily structured light. *Nat Commun* **14**, 7222 (2023).
107. C. He, Y. Shen, A. Forbes, Towards higher-dimensional structured light. *Light Sci Appl* **11**, 205 (2022).
108. T. Young, The Bakerian Lecture. Experiments and calculations relative to physical optics. *Philosophical Transactions of the Royal Society of London* **94**, 1-16 (1804).
109. L. Li *et al.*, High-Capacity Free-Space Optical Communications Between a Ground Transmitter and a Ground Receiver via a UAV Using Multiplexing of Multiple Orbital-Angular-Momentum Beams. *Sci Rep* **7**, 17427 (2017).
110. J. Wang, J. Liu, S. Li, Y. Zhao, J. Du, L. Zhu, Orbital angular momentum and beyond in free-space optical communications. *Nanophotonics* **11**, 645-680 (2022).
111. H. Ren, X. Li, Q. Zhang, M. Gu, On-chip noninterference angular momentum multiplexing of broadband light. *Science* **352**, 805-809 (2016).
112. Z. Yue, H. Ren, S. Wei, J. Lin, M. Gu, Angular-momentum nanometrology in an ultrathin plasmonic topological insulator film. *Nat Commun* **9**, 4413 (2018).
113. P. Genevet, J. Lin, M. A. Kats, F. Capasso, Holographic detection of the orbital angular momentum of light with plasmonic photodiodes. *Nat Commun* **3**, 1278 (2012).
114. Z. Ji *et al.*, Photocurrent detection of the orbital angular momentum of light. *Science* **368**, 763-767 (2020).
115. A. T. O'Neil, I. MacVicar, L. Allen, M. J. Padgett, Intrinsic and extrinsic nature of the orbital angular momentum of a light beam. *Phys Rev Lett* **88**, 053601 (2002).
116. H. He, N. R. Heckenberg, H. Rubinsztein-Dunlop, Optical Particle Trapping with Higher-order Doughnut Beams Produced Using High Efficiency Computer Generated Holograms. *Journal of Modern Optics* **42**, 217-223 (1995).
117. A. Ashkin, J. M. Dziedzic, J. E. Bjorkholm, S. Chu, Observation of a single-beam gradient force optical trap for dielectric particles. *Opt Lett* **11**, 288 (1986).
118. M. E. J. Friese, T. A. Nieminen, N. R. Heckenberg, H. Rubinsztein-Dunlop, Optical alignment and spinning of laser-trapped microscopic particles. *Nature* **394**, 348-350 (1998).
119. D. G. Grier, A revolution in optical manipulation. *Nature* **424**, 810-816 (2003).
120. T. F. Scott, B. A. Kowalski, A. C. Sullivan, C. N. Bowman, R. R. McLeod, Two-color single-photon photoinitiation and photoinhibition for subdiffraction photolithography. *Science* **324**, 913-917 (2009).
121. L. Li, R. R. Gattass, E. Gershgoren, H. Hwang, J. T. Fourkas, Achieving lambda/20 resolution by one-color initiation and deactivation of polymerization. *Science* **324**, 910-913 (2009).

122. J. Fischer, M. Wegener, Three-dimensional optical laser lithography beyond the diffraction limit. *Laser & Photonics Reviews* **7**, 22-44 (2012).
123. S. Furhapter, A. Jesacher, S. Bernet, M. Ritsch-Marte, Spiral phase contrast imaging in microscopy. *Opt Express* **13**, 689-694 (2005).
124. A. Jesacher, S. Furhapter, S. Bernet, M. Ritsch-Marte, Shadow effects in spiral phase contrast microscopy. *Phys Rev Lett* **94**, 233902 (2005).
125. G. Situ, G. Pedrini, W. Osten, Spiral phase filtering and orientation-selective edge detection/enhancement. *J Opt Soc Am A Opt Image Sci Vis* **26**, 1788-1797 (2009).
126. Y. Zhang, J. Wang, W. Zhang, S. Chen, L. Chen, LED-based visible light communication for color image and audio transmission utilizing orbital angular momentum superposition modes. *Opt Express* **26**, 17300-17311 (2018).
127. I. V. A. K. Reddy, A. Bertoncini, C. Liberale, 3D-printed fiber-based zeroth- and high-order Bessel beam generator. *Optica* **9**, (2022).
128. C. Zhou *et al.*, All-Dielectric Fiber Meta-Tip Enabling Vortex Generation and Beam Collimation for Optical Interconnect. *Laser & Photonics Reviews* **15**, (2021).
129. H. Zhang, B. Mao, Y. Han, Z. Wang, Y. Yue, Y. Liu, Generation of Orbital Angular Momentum Modes Using Fiber Systems. *Applied Sciences* **9**, (2019).
130. N. Wang, M. Zeisberger, U. Hübner, M. A. Schmidt, Nanotrimer enhanced optical fiber tips implemented by electron beam lithography. *Optical Materials Express* **8**, (2018).
131. M. Zeisberger, H. Schneidewind, U. Hübner, T. Wieduwilt, M. Plidschun, M. A. Schmidt, Plasmonic Metalens-Enhanced Single-Mode Fibers: A Pathway Toward Remote Light Focusing. *Advanced Photonics Research* **2**, (2021).
132. N. Wang, M. Zeisberger, U. Hübner, M. A. Schmidt, Boosting Light Collection Efficiency of Optical Fibers Using Metallic Nanostructures. *ACS Photonics* **6**, 691-698 (2019).
133. J. Yang *et al.*, Photonic crystal fiber metalens. *Nanophotonics* **8**, 443-449 (2019).
134. G. H. Yuan, E. T. Rogers, N. I. Zheludev, Achromatic super-oscillatory lenses with sub-wavelength focusing. *Light Sci Appl* **6**, e17036 (2017).
135. G. Kostovski, U. Chinnasamy, S. Jayawardhana, P. R. Stoddart, A. Mitchell, Sub-15nm optical fiber nanoimprint lithography: A parallel, self-aligned and portable approach. *Adv Mater* **23**, 531-535 (2011).
136. A. Kuchmizhak, S. Gurbatov, A. Nepomniaschii, O. Vitrik, Y. Kulchin, High-quality fiber microaxicons fabricated by a modified chemical etching method for laser focusing and generation of Bessel-like beams. *Appl Opt* **53**, 937-943 (2014).
137. D. A. Talmage, P. J. Curran, Remote sensing using partially polarized light. *International Journal of Remote Sensing* **7**, 47-64 (2007).
138. W.-G. Kim, N.-W. Moon, H.-K. Kim, Y.-H. Kim, Linear Polarization Sum Imaging in Passive Millimeter-Wave Imaging System for Target Recognition. *Progress In Electromagnetics Research* **136**, 175-193 (2013).
139. S. Brasselet, Polarization-resolved nonlinear microscopy: application to structural molecular and biological imaging. *Advances in Optics and Photonics* **3**, (2011).
140. R. C. Jones, A New Calculus for the Treatment of Optical SystemsI Description and Discussion of the Calculus. *Journal of the Optical Society of America* **31**, (1941).
141. F. Perrin, Polarization of Light Scattered by Isotropic Opalescent Media. *The Journal*

*of Chemical Physics* **10**, 415-427 (1942).
142. E. Collett, *Field Guide to Polarization*. (2005).

# Acknowledgement

First and foremost, I would like to express my heartfelt gratitude to my advisor, Prof. Dr. Leo Menezes. His immense support and assistance in both my research and personal life have been invaluable. Not only did Professor Leo provide crucial academic guidance, but he also offered selfless help and encouragement during challenging times. His expertise and patient teaching have allowed me to make continuous progress throughout my research.

Secondly, I am deeply thankful to Prof. Dr. Stefan Maier for accepting me into the Chair in Hybrid Nanosystems. This opportunity has allowed me to engage in a high-level research environment and projects. Professor Maier's trust and support enabled me to make significant advancements in this field, and his research team provided me with invaluable resources and collaboration opportunities.

Special thanks to Dr. Yi Li, who offered tremendous help when I first arrived in Germany. Dr. Li not only assisted me in quickly adapting to my new living environment but also provided invaluable advice and guidance in my scientific research. His support made my life abroad much smoother and more enjoyable.

I am grateful to Dr. Haoran Ren for his hands-on guidance with my research projects, which have led to my current achievements. Dr. Ren provided detailed instruction on experimental procedures and data analysis, as well as significant assistance with writing papers and presenting reports. His patience and meticulousness have greatly benefited me.

Next, I would like to extend my gratitude to my Ph.D. committee, particularly Prof. Dr. Ralf Jungmann, Prof. Dr. Tim Liedl, Prof. Dr. Armin Scrinzi, and Dr. Theobald Lohmuller. Their invaluable opinions and support during my doctoral research have greatly enhanced and refined my work. Their expertise and constructive feedback have been crucial to the improvement and completion of my research.

Reflecting on my five-year Ph.D. journey abroad, especially during the period when the COVID-19 pandemic prevented me from returning home, I am immensely grateful for my parents' selfless support and assistance. They have always been my strongest pillars of support. No matter the difficulties I encountered, their love and encouragement have always helped me to persevere and stay resilient.

Lastly, I would like to thank my friends: Xiankai Pang, Nan Qiu, and Hong Luo. The time spent with you has been the most beautiful memory of my Ph.D. journey. Together, we explored many countries and created many precious memories. Your friendship and support have enriched my life abroad and made it more fulfilling.